FIU Electronic Theses and Dissertations   University Graduate School

2-25-2015

Multimode Analysis of Nanoscale Biomolecular Interactions

Purushottam Babu Tiwari
Florida International University, tiwaree79@gmail.com

FLORIDA INTERNATIONAL UNIVERSITY

Miami, Florida

MULTIMODE ANALYSIS OF NANOSCALE BIOMOLECULAR INTERACTIONS

A dissertation submitted in partial fulfillment of the

requirements for the degree of

DOCTOR OF PHILOSOPHY

in

PHYSICS

by

Purushottam Babu Tiwari

2015

To: Dean Michael R. Heithaus
     College of Arts and Sciences

This dissertation, written by Purushottam Babu Tiwari, and entitled Multimode Analysis of Nanoscale Biomolecular Interactions, having been approved in respect to style and intellectual content, is referred to you for judgment.

We have read this dissertation and recommend that it be approved.

_____
Jaroslava Miksovska

_____
Yuk-Ching Tse-Dinh

_____
Xuewen Wang

_____
Jin He

_____
Yesim Darici, Major Professor

Date of Defense: February 25, 2015

The dissertation of Purushottam Babu Tiwari is approved.

_____
Dean Michael R. Heithaus
College of Arts and Sciences

_____
Dean Lakshmi N. Reddi
University Graduate School

Florida International University, 2015

DEDICATION

I dedicate this dissertation to my parents, wife Ambika, and kids Prakriti and Anup.

ACKNOWLEDGMENTS

ABSTRACT OF THE DISSERTATION

MULTIMODE ANALYSIS OF NANOSCALE BIOMOLECULAR

INTERACTIONS

by

Purushottam Babu Tiwari

Florida International University, 2015

Miami, Florida

Professor Yesim Darici, Major Professor

Biomolecular interactions, including protein-protein, protein-DNA, and protein-ligand interactions, are of special importance in all biological systems. These interactions may occer during the loading of biomolecules to interfaces, the translocation of biomolecules through transmembrane protein pores, and the movement of biomolecules in a crowded intracellular environment. The molecular interaction of a protein with its binding partners is crucial in fundamental biological processes such as electron transfer, intracellular signal transmission and regulation, neuroprotective mechanisms, and regulation of DNA topology. In this dissertation, a customized surface plasmon resonance (SPR) has been optimized and new theoretical and label free experimental methods with related analytical calculations have been developed for the analysis of biomolecular interactions.

Human neuroglobin (hNgb) and cytochrome c from equine heart (Cyt c) proteins have been used to optimize the customized SPR instrument. The obtained K_d value (~13 µM), from SPR results, for Cyt c-hNgb molecular interactions is in general agreement with a previously published result. The SPR results also confirmed no significant impact

of the internal disulfide bridge between Cys 46 and Cys 55 on hNgb binding to Cyt c. Using SPR, *E. coli* topoisomerase I enzyme turnover during plasmid DNA relaxation was found to be enhanced in the presence of Mg^{2+}. In addition, a new theoretical approach of analyzing biphasic SPR data has been introduced based on analytical solutions of the biphasic rate equations.

In order to develop a new label free method to quantitatively study protein-protein interactions, quartz nanopipettes were chemically modified. The derived K_d (~20 µM) value for the Cyt c-hNgb complex formations matched very well with SPR measurements (K_d ~16 µM). The finite element numerical simulation results were similar to the nanopipette experimental results. These results demonstrate that nanopipettes can potentially be used as a new class of a label-free analytical method to quantitatively characterize protein-protein interactions in attoliter sensing volumes, based on a charge sensing mechanism.

Moreover, the molecule-based selective nature of hydrophobic and nanometer sized carbon nanotube (CNT) pores was observed. This result might be helpful to understand the selective nature of cellular transport through transmembrane protein pores.

TABLE OF CONTENTS

LIST OF TABLES

LIST OF FIGURES

CHAPTER 1: INTRODUCTION

Biomolecular interactions including, protein-protein, protein-DNA, and protein-ligand interactions, are of special importance in all biological systems and processes. These interactions occur during the loading of biomolecules to interfaces [1], the translocation of biomolecules through transmembrane protein pores [2,3], and the movement of biomolecules in a crowded intracellular environment [4,5]. The molecular interaction of a protein with its binding partners has great significance in fundamental biological processes such as electron transfer [6], intracellular signal transmission and regulation [7], neuroprotective mechanisms [8], and regulation of DNA topology [9,10]. A detailed analysis of these interactions allows us to understand the role of protein molecules in fundamental intracellular processes, translocation and complex formation, and to determine the affinity of proteins to their binding partners.

One of the major goals of this dissertation is to optimize a customized surface plasmon resonance (SPR) instrument for the quantitative analysis of the fundamental biomolecular interactions. For this purpose, human neuroglobin (hNgb) and cytochrome c from equine heart (Cyt c) proteins have been used as model systems. Following the successful detection of Cyt c-hNgb interactions, the optimized SPR instrument was used to quantitatively study protein-DNA interactions. Molecular interaction between *Escherichia coli* topoisomerase I (EctopoI) and pBAD/Thio supercoiled plasmid DNA has been successfully investigated. DNA topoisomerases change the topology of DNA, which is crucial in transcription, translation and recombination [11].

Another major purpose of this dissertation was to introduce a new label free method for the analysis of biomolecular interaction. In order to achieve this goal, quartz

nanopipettes were chemically modified to quantitatively study Cyt c-hNgb protein-protein interaction in an attoliter sensing volumes, based on a charge sensing mechanism.

Besides experimental methods of studying biomolecular interactions, this dissertation also aims at presenting new theoretical approaches and related analytical calculations for the analysis and understanding of experimental results. To this end, a theoretical approach for the analysis of the biphasic SPR data has been introduced based on analytical solutions. Moreover, finite element based numerical simulations have also been performed to understand the nanopipette experimental results.

In addition to above method biomolecular interactions, another aspect of this dissertation was to investigate the molecular translocation through nanopores that mimic the protein pores inside the body. Carbon nanotube (CNT) based nanoporous membrane device was used to study the translocation of small charged molecules.

The following sections in this chapter present an overview of the fundamental biomolecular interactions and a brief explanation of research projects and results.

1.1: Interaction mechanisms of proteins with their binding partners

Despite complexity in structure, a protein molecule recognizes its binding partner as a result of the specific interaction [12]. As explained below, several intermolecular interaction mechanisms, specific or non-specific, play crucial roles in the complex formation between a protein molecule and its binding partner.

1.1.1: Electrostatic interaction

Electrostatic interaction takes place between two oppositely charged molecules and it is long range in nature [13], which typically depends upon the net charge of protein molecules [14]. The electrostatic interaction is ubiquitous in many biomolecular

interactions [15]. The electrostatic free energy ($\Delta\Delta G_{elec}^{all}$) for the interaction of charged

biological macromolecules, A and B, is given by Equation 1.1 [16]:

$$\Delta\Delta G_{elec}^{all} = \frac{1}{2}\sum_{i(A:B)} q_i \Phi^{A:B}(r_i) - \frac{1}{2}\sum_{i(A)} q_i \Phi^A(r_i) - \frac{1}{2}\sum_{i(B)} q_i \Phi^B(r_i) \qquad (1.1)$$

where, A:B represents the complex formation between A and B, q_i the electric charge,

and $\Phi(r_i)$ is the electric potential.

1.1.2: Dipole-dipole interaction

Two opposite charges with equal magnitude separated at a distance constitute an

electric dipole. The alignment of molecular dipoles is one of the several possibilities

responsible for the complex formation between a protein and its binding partner [17]. The

interaction energy, with the second order correction, for two freely rotating dipoles is

given by Equation 1.2 [18]:

$$U = -\frac{2\mu_1^2\mu_2^2}{3(4\pi\varepsilon_o)^2 kTr^6} \qquad (1.2)$$

where, μ_1 and μ_2 are the dipole moments of two molecules, ε_o is the permittivity of the

vacuum, k is the Boltzmann constant, T is absolute temperature, and r is the distance

between the molecules. The dipole moment of proteins have been measured previously

by Takashima et al. and Antosiewicz et al. [19,20].

1.1.3: Van der Waals interaction

Van der Waals interactions are a consequence of a random fluctuation of the

electronic distribution in an atom that leads to transient electric dipoles [21]. These

interactions are short-range in nature when compared to the molecular dimensions of

proteins. These interactions are attractive and the strength of interactions increases as the

distance between molecules or distance from interacting surface in solution decreases [22]. The Van der Waals interaction is the sum of the interaction between two permanent dipoles (Keesom contribution), between a permanent dipole and a corresponding induced dipole (Debye contribution), and between two induced dipoles (London dispersion contribution) [22,23].

1.1.4: Hydrogen Bonding

Hydrogen bonding occurs because of the weak electrostatic interaction between hydrogen and electronegative atom like oxygen. Several terminal groups such as –NH2, -C=O, and –OH in proteins are capable of establishing a hydrogen bond [21]. The binding interface of proteins is comparatively more hydrophilic than the interior [24]. There are about 1.42 charged groups per 100Å^2 of protein binding surface [25]. Therefore, the binding interface generally forms hydrogen bonds. On average, there are 10.4 hydrogen bonds in one binding interface. The hydrogen bonding, therefore, plays a dominant role in specific interaction of protein molecules with their binding partners [24].

1.1.5: Hydrophobic interaction

Hydrophobic interaction is the aggregation of non-polar molecules in an aqueous medium [26] because of the disruption of hydrogen bonds between water molecules. The release of water molecules from the protein-ligand binding site, because of hydrophobic interaction, plays an important role in the complex formation between the binding partners, changing the total entropy and total free energy [27]. Hydrophobicity is the key factor for the inter-protein complex stabilization [28].

1.1.6: Transient covalent bonding

In addition to above-mentioned non-covalent interactions, a protein molecule may

exhibit a transient covalent interaction with its binding partner. More specifically, DNA topoisomerases form a transient covalent bond while making a complex with DNA [29]. The cleavable covalent complex between topoisomerase and DNA is formed via transesterification of active site tyrosyl and a phosphate group of DNA. The breakage of the covalent complex follows with another transesterification [10]. The cutting and rejoining of the DNA strands via the formation of cleavable covalent complex is shown in Figure 1.1. The DNA topoisomerases change the topological stage of DNA [9,10], which is very important in DNA replication, transcription, and recombination [11].
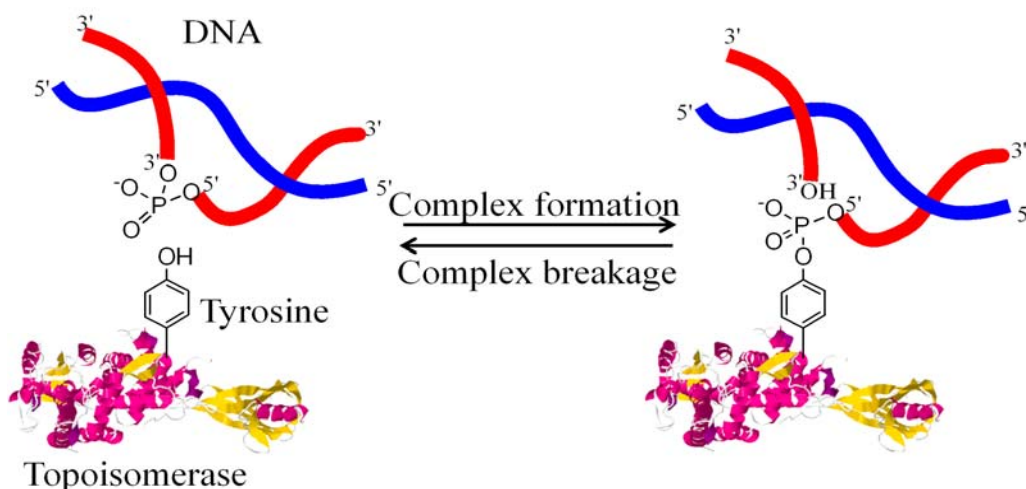
Figure 1.1: Formation and breakage of transient covalent bond between DNA topoisomerase and DNA. The cartoon scheme for the DNA topoisomerase is adapted from protein data bank (PDB) entry 1ECL.

1.2: Binding models for biomolecular interactions

1.2.1: Monophasic (1:1 Langmuir) binding model of biomolecular interaction

The monophasic binding model is considered when analyte-ligand complex is formed via single site binding. A simple biomolecular reaction corresponding to the monophasic binding model is given by [30,31]:

$$[A] + [B] \underset{k_d}{\overset{k_a}{\rightleftharpoons}} [AB]$$
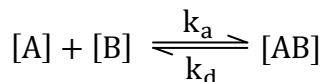
and the corresponding association and dissociation rate equations are given by:

$$\frac{d[AB]}{dt} = k_a[A][B] - k_d[AB]$$

$$\frac{d[AB]}{dt} = -k_d[AB]$$

(1.3)

where, [A] corresponds to the analyte concentration (C) and assumed to be constant, [B] corresponds to the ligand concentrations, available surface binding sites, k_a is the association rate constant, and k_d is the dissociation rate constant. With $[B] = [B_o] -$ [AB], where $[B_o]$ corresponds to the initial available surface binding sites, Equation 1.3 can be rewritten as:

$$\frac{d[AB]}{dt} = Ck_a[B_0] - (k_aC + k_d)[AB]$$

$$\frac{d[AB]}{dt} = -k_d[AB]$$

(1.4)

1.2.2: Biphasic binding model
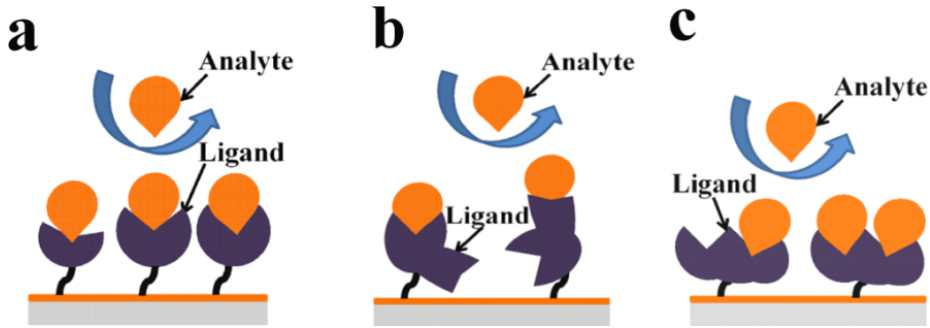
Figure 1.2: Cartoon schemes: (a) the two-step conformational change model (Model 1), (b) the heterogeneous ligand model (Model 2), and (c) the bivalent ligand model (Model 3). The ribbon-shaped arrow indicates the analyte flow over ligand immobilized sensor surface.

There are several possibilities with the biphasic interactions with complicated data analysis as compared to the monophasic model. Figure 1.2 shows the schematic representation of the three biphasic models governed by the coupled linear differential rate equations presented in this dissertation.

1.2.2.1: Two-step conformational change model

The two-step conformational change model is applicable when the analyte-ligand complex undergoes a conformational change to stabilize the complex [32,33]. The biphasic reaction for the two-step conformational change model can be written as:

$$[A] + [B] \; \underset{k_{d1}}{\overset{k_{a1}}{\rightleftharpoons}} [AB^*] \underset{k_{-2}}{\overset{k_2}{\rightleftharpoons}} [AB]$$
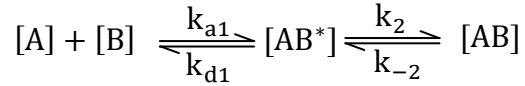
and the corresponding rate equations are given by:

$$\frac{d[AB^*]}{dt} = k_{a1}[A][B] - k_{d1}[AB^*] - k_2[AB^*] + k_{-2}[AB]$$

$$\frac{d[AB]}{dt} = k_2[AB^*] - k_{-2}[AB]$$

(1.5)

where, $[AB^*]$ and $[AB]$ represent the intermediate stage and the final docked stage of the complex, respectively. In this case, the second association rate constant (k_2) is different from the normal association rate constant, and its unit is s^{-1}, not $M^{-1}s^{-1}$ [34]. Using $[B] = [B_0] - [AB^*] - [AB]$, Equation 1.5 can be expressed as given below:

$$\frac{d[AB^*]}{dt} = k_{a1}C[B_0] - (k_{a1}C + k_{d1} + k_2)[AB^*] - (k_{a1}C - k_{-2})[AB]$$

$$\frac{d[AB]}{dt} = k_2[AB^*] - k_{-2}[AB]$$

(1.6)

1.2.2.2: Heterogeneous ligand model

The heterogeneous ligand model explains two independent bindings of analytes to immobilized ligands [35,36] as represented by the following biphasic reactions:
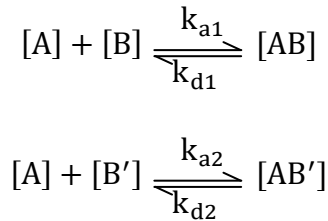
$$[A] + [B] \; \underset{k_{d1}}{\overset{k_{a1}}{\rightleftharpoons}} [AB]$$

$$[A] + [B'] \; \underset{k_{d2}}{\overset{k_{a2}}{\rightleftharpoons}} [AB']$$

and the corresponding rate equations are given by:

$$\frac{d[AB]}{dt} = k_{a1}[A][B] - k_{d1}[AB]$$

$$\frac{d[AB']}{dt} = k_{a2}[A][B'] - k_{d2}[AB']$$

(1.7)

Using $[B] = [B_0] - [AB]$, and $[B'] = [B'_0] - [AB']$, Equation 1.7 can be rewritten as seen below in Equation 1.8:

$$\frac{d[AB]}{dt} = k_{a1}C[B_0] - (k_{a1}C + k_{d1})[AB]$$

$$\frac{d[AB']}{dt} = k_{a2}C[B'_0] - (k_{a2}C + k_{d2})[AB']$$

(1.8)

1.2.2.3: Bivalent ligand model

The bivalent ligand model accounts for the two sequential analyte-ligand bindings with different affinity [37-39]. The biphasic reaction for the bivalent model can be described by the following reactions:

$$[A] + [B] \underset{k_{d1}}{\overset{k_{a1}}{\rightleftharpoons}} [A_1B]$$
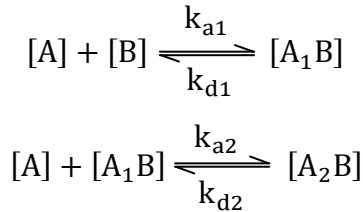
$$[A] + [A_1B] \underset{k_{d2}}{\overset{k_{a2}}{\rightleftharpoons}} [A_2B]$$

and the corresponding rate equations are given by:

$$\frac{d[A_1B]}{dt} = k_{a1}[A][B] - k_{d1}[A_1B] - k_{a2}[A][A_1B] + k_{d2}[A_2B]$$

$$\frac{d[A_2B]}{dt} = k_{a2}[A][A_1B] - k_{d2}[A_2B]$$

(1.9)

Using $[B] = 2[B_o] - [A_1B] - 2[A_2B]$, above equation can be expressed as given in Equation 1.10.

$$\frac{d[A_1B]}{dt} = 2k_{a1}C[B_o] - (k_{a1}C + k_{a2}C + k_{d1})[A_1B] - (2k_{a1}C - k_{d2})[A_2B]$$

$$\frac{d[A_2B]}{dt} = k_{a2}C[A_1B] - k_{d2}[A_2B]$$

(1.10)

Here, $[B_o]$ corresponds to the concentration of the ligands, with each ligand having two binding sites.

1.3: Translocation through transmembrane protein pores

There are transporter proteins on the biological membrane, either categorized as channels (pores) or carriers [40,41]. Stimulated chemically or electro-physiologically, the channel proteins allow the solute to pass through selective pores whereas the carrier proteins allow substrate translocation under concentration gradient across the membrane [42]. Membrane proteins typically have hydrophobic and polar surfaces in aqueous environment [43]. Translocation of polymers through protein pores has been previously studied both theoretically [44,45] and experimentally [46,47]. The protein pores have variable diameter up to several nanometers [44,46,48-51]. Translocation of charged or neutral molecules, polymers, and polypeptides through these nanometer sized protein pores (channels) is of special importance in fundamental life processes [44,52] including, regulation of nutrients and waste products [53].

1.4: Research projects and results

A surface plasmon resonance (SPR) instrument was optimized and used to investigate protein-protein and protein-DNA interactions. Various chemical surface modifications and characterization strategies were followed in order to prepare sensor chips for their use in SPR. Human neuroglobin (hNgb) and cytochrome c from equine heart (Cyt c) has been used as a model system to optimize the SPR instrument for its use to investigate protein-protein molecular interaction. A K_d value of ~13 µM was obtained for Cyt c-hNgb interactions using phosphate buffer at pH 7.0. A similar K_d value of (~45 µM) for Cyt c binding to dithiothreitol (DTT) reduced hNgb in Tris buffer has been

reported previously [17]. On the basis of the SPR results, it has been observed that the CD-loop flexibility, in hNgb, does not significantly affect its affinity to Cyt c.

The use of the optimized custom-built SPR system was extended to investigate the molecular interaction between *E.coli* topoisomerase I (EctopoI) and pBAD/Thio supercoiled plasmid DNA (pBAD/Thio). The study is the first biophysical investigation between these molecules in terms of quantitative determination of the interaction. EctopoI removes excess negative supercoils to regulate DNA supercoiling [54]. The regulation of DNA topology has significance in biological processes such as transcription, translation, and recombination [11]. The catalytic activity of topoisomerase I (topoI) requires Mg^{2+} [55]. The equilibrium dissociation constant (K_d) values of ~8 nM and ~15 nM in the presence and absence of Mg^{2+} for EctopoI-pBAD/Thio interactions were determined, respectively. Moreover, a larger dissociation rate constant (k_d) was obtained for interaction between Mg^{2+} bound EctopoI and pBAD/Thio supercoiled plasmid DNA. These SPR results revealed that the enzyme turnover would be enhanced in the presence of Mg^{2+}.

The determination of rate constants, the association rate constant (k_a) and the dissociation rate constant (k_d), requires the fitting of SPR sensorgrams (profiles) mainly with single or double exponential functions. The SPR data analysis by fitting with single exponential function is simple and straightforward. However, there is no simple procedure to analyze the biphasic SPR sensorgrams. The dissertation, therefore, presents a new analysis procedure for the biphasic SPR sensorgrams, using a theoretical approach. The new method is more straightforward than currently existing SPR data fitting

procedures to choose the underlying biphasic interaction and to perform further analysis, including the determination of the rate constants.

To develop a new method to quantitatively investigate protein-protein interaction, quartz nanopipettes with pore diameters of ~37 nm were chemically modified to immobilize protein molecules. Using these modified nanopipettes, Cyt c-hNgb molecular interactions was investigated in attoliter sensing volumes, based on a charge sensing mechanism. The K_d value of Cyt c-hNgb complex formation (K_d ~20 µM) was found to be very similar to the K_d value obtained from SPR measurements. Finite element based numerical simulations were also performed in order to understand the fundamental charge sensing mechanism. Using the experimental conditions, the simulation results were similar to the experimental nanopipette. Altogether, these results suggest that quartz nanopipettes are a new analytical tool to quantitatively study protein-protein interactions.

Moreover, this dissertation presents the investigation of the translocation of small charged molecules through CNT based nanopores. Carbon nanotube can be regarded as a model system to help understand the transporter proteins on the cell membrane that work in aqueous environments with hydrophobic inner walls and nanometer channel sizes [56]. Under the effect of an applied electric field, an obvious translocation of ferricyanide ($Fe(CN)_6^{3-}$) molecules was observed whereas the translocation of ruthenium bipyridine ($Ru(bpy)_3^{2+}$) was not as prominent as that of ferricyanide. Depending on the molecular structure, the pi-pi interaction between the rings of ruthenium bipyridine molecules and CNT surface was found to be the factor that hindered translocation of ruthenium bipyridine molecules, compared to ferricyanide. These results might be helpful to understand the selective nature of the intracellular transport processes [57].

11

In summary, this dissertation presents optimization of a customized SPR instrument for the quantitative study of protein-protein and protein-DNA molecular interactions. Based on analytical solutions, a new theoretical approach of analyzing biphasic SPR data has also been presented. With experimental and simulation results, this dissertation introduces a new label free analytical method to quantitatively study protein-protein interaction in attoliter sensing volumes based on a charge sensing mechanism. This dissertation also presents the results for the translocation of small charged molecules through CNT nanopores. These nanopores are very analogous to transmembrane protein pores in terms of hydrophobicity and nanometer sized pore diameter. Altogether, this dissertation will, therefore, be a valuable contribution to the research on the multimode analysis of nanoscale biomolecular interactions.

1.5: References

1. D.G. Castner, B.D. Ratner, Surf. Sci. 2002, 500, 28.

2. P. Rehling, K. Model, K. Brandner, P. Kovermann, A. Sickmann, H.E. Meyer, W. Kühlbrandt, R. Wagner, K.N. Truscott, N. Pfanner, Science 2003, 299, 1747.

3. S.C. Hinnah, R. Wagner, N. Sveshnikova, R. Harrer, J. Soll, Biophys. J. 2002, 83, 899.

4. Q. Wang, A. Zhuravleva, L.M. Gierasch, Biochemistry 2011, 50, 9225.

5. G. Rivas, F. Ferrone, J. Herzfeld, EMBO reports 2004, 5, 23.

6. D.G.G. McMillan, S.J. Marritt, M.A. Firer-Sherwood, L. Shi, D.J. Richardson, S.D. Evans, S.J. Elliott, J.N. Butt, L.J.C. Jeuken, J. Am. Chem. Soc. 2013, 135, 10550.

7. T. Pawson, P. Nash, Genes Dev. 2000, 14, 1027.

8. T.J. Craig, L.F. Ciufo, A. Morgan, J. Biochem. . Biophys. Methods 2004, 60, 49.

9. J.C. Wang, Nat. Rev. Mol. Cell Biol. 2002, 3 430.

10. K.D. Corbett, J.M. Berger, Annu. Rev. Biophys. Biomol. Struct. 2004, 33, 95.

11. J.J. Champoux, Annu. Rev. Biochem. 2001, 70, 369.

12. P. Carbonell, R. Nussinov, A. del Sol, Proteomics 2009, 9, 1744.

13. K. Brock, K. Talley, K. Coley, P. Kundrotas, E. Alexov, Biophys. J. 2007, 93, 3340.

14. Z. Zhe, W. Shawn, A. Emil, Physi. Biol. 2011, 8, 035001.

15. B. Honig, A. Nicholls, Science 1995, 268, 1144.

16. F.B. Sheinerman, B. Honig, J. Mol. Biol. 2002, 318, 161.

17. S.H. Bønding, K. Henty, A.J. Dingley, T. Brittain, Int. J. Biol. Macromol. 2008, 43, 295.

18. P. Atkins, The Elements of Physical Chemistry (3rd ed.), W. H. Freeman and Company, New York, USA, 1993.

19. S. Takashima, Biophys. Chem. 1996, 58, 13.

20. J. Antosiewicz, D. Porschke, Biochemistry 1989, 28, 10072.

21. P.N. Prasad, In: Introduction to Biophotonics, John Wiley & Sons, Inc., 2004, 50.

22. C.M. Roth, B.L. Neal, A.M. Lenhoff, Biophys. J. 1996, 70, 977.

23. J.M. Prausnitz, R.N. Lichtenthaler, E.G. Azevedo, Molecular Thermodynamics of Fluid-Phase Equilibria (2nd ed.), Prentice-Hall, Englewood Cliffs, New Jersey, 1986.

24. D. Xu, C.J. Tsai, R. Nussinov, Protein Eng. 1997, 10, 999.

25. D.J. Barlow, J.M. Thornton, Biopolymers 1986, 25, 1717.

26. T.M. Raschke, J. Tsai, M. Levitt, Proc. Nat. Acad.f Sci. 2001, 98, 5965.

27. P. Cozzini, M. Fornabaio, A. Marabotti, D.J. Abraham, G.E. Kellogg, A. Mozzarelli, Curr. Med. Chem. 2004, 11, 1345.

28. C. Chothia, J. Janin, Nature 1975, 256, 705.

29. T. Viard, C.B. de la Tour, Biochimie 2007, 89, 456.

30. M. Ritzefeld, N. Sewald, J. Amino Acids 2012, 2012, 19.

31. W. Huber, J. Hurst, D. Schlatter, R. Barner, J. Hübscher, W.C. Kouns, B. Steiner, Eur. J. Biochem. 1995, 227, 647.

32. N.J. de Mol, M.I. Catalina, M.J.E. Fischer, I. Broutin, C.S. Maier, A.J.R. Heck, BBA - Protein Proteom. 2004, 1700, 53.

33. M. Futamura, P. Dhanasekaran, T. Handa, M.C. Phillips, S. Lund-Katz, H. Saito, J. Biol. Chem. 2005, 280, 5414.

34. M.L. Azoitei, Y.-E.A. Ban, J.-P. Julien, S. Bryson, A. Schroeter, O. Kalyuzhniy, J.R. Porter, Y. Adachi, D. Baker, E.F. Pai, W.R. Schief, J. Mol. Biol. 2012, 415, 175.

35. S.M. Alam, G.M. Davies, C.M. Lin, T. Zal, W. Nasholds, S.C. Jameson, K.A. Hogquist, N.R.J. Gascoigne, P.J. Travers, Immunity 1999, 10, 227.

36. D.J. O'Shannessy, D.J. Winzor, Anal. Biochem. 1996, 236, 275.

37. E.R. Sprague, W.L. Martin, P.J. Bjorkman, J. Biol. Chem. 2004, 279, 14184.

38. A.M. Giannetti, P.M. Snow, O. Zak, P.J. Björkman, PLoS Biol. 2003, 1, e51.

39. Y.-S. Lo, W.-H. Tseng, C.-Y. Chuang, M.-H. Hou, Nucleic Acids Res. 2013, 41, 4284.

40. M.H. Saier, Microbiol. Mol. Biol. Rev. 2000, 64, 354.

41. W. Busch, M.H. Saier, Crit. Rev. Biochem. Mol. Biol. 2002, 37, 287.

42. S.G. Dahl, I. Sylte, A.W. Ravna, J Pharm. Exp. Ther. 2004, 309, 853.

43. C. Ostermeier, H. Michel, Curr. Opin. Struct. Biol. 1997, 7, 697.

44. M. Muthukumar, C.Y. Kong, Proc.e Nat. Acad.f Sci. 2006, 103, 5273.

45. D.P. Tieleman, Clin. Exp. Pharm. Physiol. 2006, 33, 893.

46. J.J. Kasianowicz, E. Brandin, D. Branton, D.W. Deamer, Proc. Nat. Acad. Sci. 1996, 93, 13770.

47. L.-Q. Gu, M. Dalla Serra, J.B. Vincent, G. Vigh, S. Cheley, O. Braha, H. Bayley, Proc. Nat. Acad. Sci. 2000, 97, 3959.

48. M. Chen, S. Khalid, M.S.P. Sansom, H. Bayley, Proc. Nat. Acad. Sci. 2008, 105, 6272.

49. M.P. Schwartz, A. Matouschek, Proc. Nati. Acad. Sci. 1999, 96, 13086.

50. I. Bárcena-Uribarri, M. Thein, M. Barbot, E. Sans-Serramitjana, M. Bonde, R. Mentele, F. Lottspeich, S. Bergström, R. Benz, J. Biol. Chem. 2014, 289, 18614.

51. A. Mangel, J.M. LeitÃO, R. Batel, H. Zimmermann, W.E.G. MÜLler, H.C. SchrÖDer, Eur. J. Biochem. 1992, 210, 499.

52. L. Movileanu, J.P. Schmittschmitt, J. Martin Scholtz, H. Bayley, Biophys. J. 2005, 89, 1030.

53. B. Hille, Ionic Channels of Excitable Membranes, Sinauder Associates, Inc., Sunderland, MA, 2001.

54. K. Drlica, Trends Gen. 1990, 6, 433.

55. C. Sissi, M. Palumbo, Nucleic Acids Res. 2009, 37, 702.

56. P. Krishnakumar, P.B. Tiwari, S. Staples, T. Luo, Y. Darici, J. He, S.M. Lindsay, Nanotechnology 2012, 23, 455101.

57. B. Alberts, A. Johnson, J. Lewis, M. Raff, K. Roberts, P. Walter, Molecular biology of the cell (4th ed.), Garland Science, New York, 2002.

CHAPTER 2: METHODS

This dissertation presents label free experimental techniques, surface plasmon resonance (SPR) and nanopore techniques, and theoretical simulations along with related analytical calculations for the analysis of the fundamental biomolecular interactions. The nanopore technique includes the use of quartz nanopipettes and carbon nanotube (CNT) pores. This chapter presents all the methods, experimental and theoretical, which have been used to successfully accomplish this dissertation.

2.1: Surface plasmon resonance (SPR)

A customize SPR system was optimized in this dissertation in order to investigate the label-free detection of the biomolecular interactions, including cytochrome c-human neuroglobin and E.coli topoisomerase I-supercoiled DNA interactions. The following subsections in this chapter explain the instrumentation, data collection, and sensor surface modification and characterization.

2.1.1: Instrumentation and data collection

The SPR system is comprised of a diode laser (Thor Labs, 4.5 mW and λ=635nm), as a light source, and a single array photodetector (TSL3301EVM, TAOS). Polycrystalline gold chips (50 nm gold layer deposited over a 2.5 nm titanium adhesion layer coated on 18mm x 18mm cover slip glass slides) were purchased from Platypus Technologies, LLC. The gold coated chip was used to prepare the SPR sensor. Each chip was cut into two pieces before processing or any measurements. The properly cleaned gold chip was chemically modified using various modification strategies (as explained below) for its use as SPR sensor. The modified sensor chip was placed over the BK7 semicircular cylindrical prism (Melles Griot) flat surface using a thin layer of refractive

index matching fluid (immersion oil n=1.515)[1] and a customized Teflon flow cell was mounted above the sensor chip. The Teflon flow cell has four sets of flow channels to carry out four independent SPR measurements under similar conditions. This allows to monitor the reproducibility of the SPR results.

The p-polarized light from the diode laser passes through the BK7 prism followed by the total internal reflection (TIR) from the metal (gold)-dielectric interface. The intensity of reflected light is detected by a photodetector and is collected using a program written in C++. At the condition of resonance, the intensity of reflected light reduces sharply. Any change in refractive index in the surrounding of the metal surface is reflected as the change in the SPR angle, the angle at minimum reflectance intensity [1-3]. The change in SPR angle for each refractive index variation leads to the change in pixel position on the detector. The centroid method was used to calculate the center-of-mass position of the certain portion of SPR dip below a certain threshold [4,5]. The dip position corresponding to each SPR angle was calculated by using Equation 2.1 [5]:

$$X = \frac{\int x(h-I(x))dx}{\int (h-I(x))dx}$$
(2.1)

where, X is an averaged pixel position, x is the pixel position of a diode, h is the threshold value, and I(x) is the light reflectance intensity as a function of x. The value of X in pixel units was then plotted as a function of time to generate SPR sensorgrams for further data analysis.

2.1.2: Sensor surface modification and characterization

The gold chip was always cleaned using oxygen plasma at 10.2 W RF power for 40 s followed by hydrogen flaming for 20 s, to reduce surface roughness [6], and then

incubated in thiol solutions, prepared in ethanol, for the chemical modifications. The different chemical modifications and characterization strategies of the gold surface are explained below.

2.1.2.1: Gold surface modification with 16-mercaptohexadecanoic acid (MHA) and 11-mercapto-1-undecanol (MUO)

The cleaned gold chip was incubated overnight in the 1:1 (v/v) mixture of 1 mM MHA and 1 mM MUO (both in 200 proof ethanol) to prepare a self-assembled monolayer (SAM) on the cleaned gold surface. The chip was then rinsed with ethanol, followed by Deionized (DI) water, and dried with argon. The SAM has the reactive carboxyl terminal groups, which can be activated by treating the mixed solution, in deionized (DI) water, of N-hydroxysuccinimide (NHS) and N-(3-dimethylaminopropyl)-N'-ethylcarbodiimide hydrochloride (EDC). The treatment forms reactive NHS esters on the gold surface that form covalent amid linkage with protein primary amine groups.

2.1.2.2: Gold surface modification with anti-His antibody

The gold chip was modified with mouse anti-His antibody (Invitrogen) in order to immobilize histidine tagged proteins. After cleaning, the gold chip was immersed in 5 mM 2-Aminoethanethiol hydrochloride (Acros Organics) in ethanol overnight at 4°C to form a SAM of cysteamine (CA) on the gold surface. The CA modified surface was rinsed with ethanol followed by DI water, treated with 2-5% glutaraldehyde (GA) solution (in DI water) followed by 2 µg/ml anti-His antibody solution in phosphate buffer saline (PBS) at pH 7.4. The functionalized chip surface was then treated with 1 M ethanolamine (pH 8.0) to quench excess aldehyde groups. GA molecules crosslink the

amines of CA SAM with the primary amine groups of anti-His antibody molecules used to capture His-tagged proteins.

2.1.2.3: Gold surface modification with Tri (ethylene glycol) mono-11-mercaptoundecyl ether (PEG-thiol) and 2-{2-[2-(1-mercaptoundec-11-yloxy)-ethoxy]-ethoxy}-ethoxy nitrilotriacetic acid TFA salt (NTA-thiol)

The hydrogen flamed chip was immediately immersed in mixed thiol solution (1:9 V/V mixture of 1 mM NTA-thiol and 1 mM PEG-thiol in ethanol, respectively) and incubated overnight. The chip was then copiously rinsed with ethanol and DI water to remove physically adsorbed thiol molecules and dried with argon. The sensor surface was activated using 40 mM aqueous solution of nickel (II) sulfate. The Ni^{2+}-NTA surface was used to capture histidine tagged proteins.

2.1.2.4: Characterization of gold surface modification

The successful chemical modification of the gold surface (formation of SAM) was confirmed using electrochemical impedance spectroscopy (EIS). A commercial electrochemical workstation (CHI760D, CH Instruments, Inc., USA) using a three-electrode system in a cuntomized Teflon electrochemical cell was used to measure EIS data. The volume of the Teflon electrochemical cell was 1.49 cm^3. The modified gold surface was used as a working electrode, Ag/AgCl electrode (prepared by immersion of Ag wire in bleach for 30 minutes) was used as a reference electrode, and Platinum/Iridium wire (0.25 mm in diameter coiled spirally) was used as a counter electrode. The counter electrode was cleaned by sonication in DI water and hydrogen flaming before its use. A DC potential EDC= + 219 mV (formal potential of the redox couple, Fe $(CN)_6^{-3/-4}$, in the solution) was applied to the working electrode. The redox

couple was prepared by mixing (1:1V/V) 10 mM potassium hexacyanoferrate (III) and 10 mM potassium ferrocyanide trihydrate in 100 mM KCl aqueous solution (pH 7.0). All measurements were carried out (at room temperature) at a frequency range from 10^{-1} Hz to 10^4 Hz with an application of sinusoidal voltage amplitude of 5 mV. The LEVMW software (Version 8.12) [7] or MATLAB (MathWorks, USA) [8] was used to perform a complex nonlinear least square (CNLS) analysis.

Contact angle measurements were also performed in order to assess chemical modifications of the gold surface. A Samsung Galaxy S4 cell phone or a Sony Cyber-shot DSC-W290 12.1 MP digital camera was used to capture an image of 5 μL water drop over the gold coated glass chip. A photo editing software was used to determine the ratio of diameter of the water drop to the chip length. This ratio was multiplied by 18 mm (the real chip length) to determine the diameter of the water drop. The diameter of the water drop was obtained using the expression, $\frac{(d_1+d_1)/2}{d'}$ (Figure 2.1).
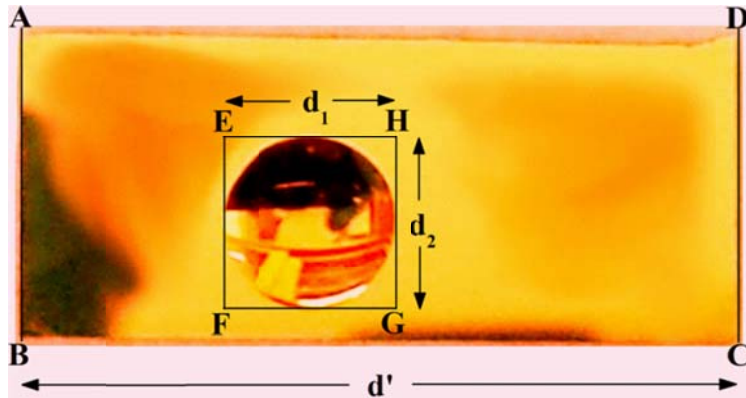
Figure 2.1: A picture of a 5 μL water drop on gold surface.

The radius of the drop was plugged in Equation 2.2 [9] and solved using Mathematica in order to determine the contact angle.

$$\frac{2-3\cos\theta+\cos^3\theta}{\sin^3\theta} = \frac{3V}{\pi r^3} \tag{2.2}$$

In Equation 2.2, V is the volume of the water drop, r is the radius of the drop, and θ is the contact angle.

2.2: Quartz nanopipettes for the quantitative study of protein-protein interactions

The fabrication, characterization and chemical surface modification of quartz nanopipettes are explained below.

2.2.1: Quartz nanopipette fabrication and characterization

The quartz capillary tubes with filament (QF100-50-7.5, Sutter Instrument) were first cleaned by piranha (caution: Piranha solutions are highly corrosive and must be handled with extreme caution) for 30 minutes, then rinsed with deionized water, and then dried in oven at $120^{o}C$ for 15 minutes. Quartz nanopipettes were fabricated from these cleaned capillary tubes by using a laser based pipette puller (P-2000, Sutter Instrument) with the following parameters: HEAT=750, FIL=4, VEL=60, DEL=170, PUL=180.

Scanning electron microscopy (SEM) and pore conductance measurement were carried out in order to characterize the nanopipette pore geometry.

2.2.1.1: SEM

Field emission scanning electron microscope (FE-SEM, JEOL JSM-6330F) was used to characterize the nanopipette geometry. Figure 2.2a and 2.2b represent SEM characterization for the geometry of the nanopipette tip. The accelerating voltage was varied from 3 kV to 20 kV, the working distance from 8 mm to 39 mm, and the emission current was always set as 12 μA. A thin layer of gold was deposited using auto sputter coater (PELCOSC-7) to make the surface conducting, to avoid the charging effect during SEM measurements. The half cone angle of fabricated nanopipettes was estimated using SEM, and the diameter was determined using this half cone angle.

2.2.1.2: Measurement of pore conductance

Ionic conductance of the nanopipette pore was also measured, from I-V curve, to estimate the pore diameter. The measurement setup is shown in Figure 2.2c. The Keithley 2636A sourcemeter (Keithley Instruments), with a scan rate of 50 mV/s, was used to record I-V curves. All measurements were performed at room temperature. The measurement setup was housed in a home-built Faraday cage to reduce external noise. Ag/AgCl electrodes (prepared by dipping clean 0.2 mm diameter Ag wires in bleach for 30 minutes) were used in all the ionic current measurements.

If the surface charge can be ignored, then the inner diameter (D) of the nanopipette can be derived using the half cone angle (θ) and the pore conductance (G_p), using Equation 2.3.

$$D = \frac{2G_p}{k}\left[\frac{1}{\pi\tan\theta}\right] \qquad (2.3)$$

where, k is the conductivity of electrolyte (25 mM KCl with 2.5 mM PB, pH 7.0).
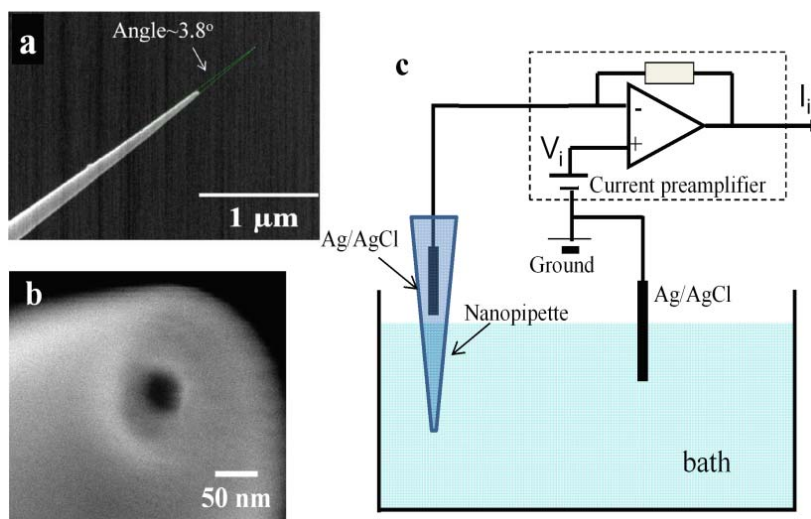
Figure 2.2: Nanopipette fabrication and ionic current measurement. (a-b) Low (a) and high resolution (b) SEM images of an as-fabricated nanopipette tip. To avoid charging, about 3-4 nm thick gold was coated on the pipette before imaging. (c) The scheme of the ionic current measurement setup.

A schematic of the chemical surface modification method is shown in Figure 2.3. The modification was finished in 5 steps: (1) 3-4 hours incubation of the nanopipette tip at room temperature in APTES (5% V/V in ethanol) inside a partially sealed beaker, which is placed in a desiccator connected to a lab vacuum line [11]; (2) 1-2 hours incubation in glutaraldehyde (0.5-2 V/V% in DI water) at room temperature; (3) Overnight incubation at 4°C in a standard phosphate buffered saline (PBS, pH 7.4) solution containing anti-His antibodies (2 µg/ml); (4) 30 minutes incubation in ethanolamine (1 M in DI water, pH 8.0) solution at room temperature to quench excess aldehyde terminal groups; and (5) Overnight incubation at 4°C in 20 µM N-terminus His-tagged hNgb in PB (10 mM, pH 7.0). The nanopipettes were rinsed repeatedly with DI water and followed by the appropriate buffer solutions between the modification steps.
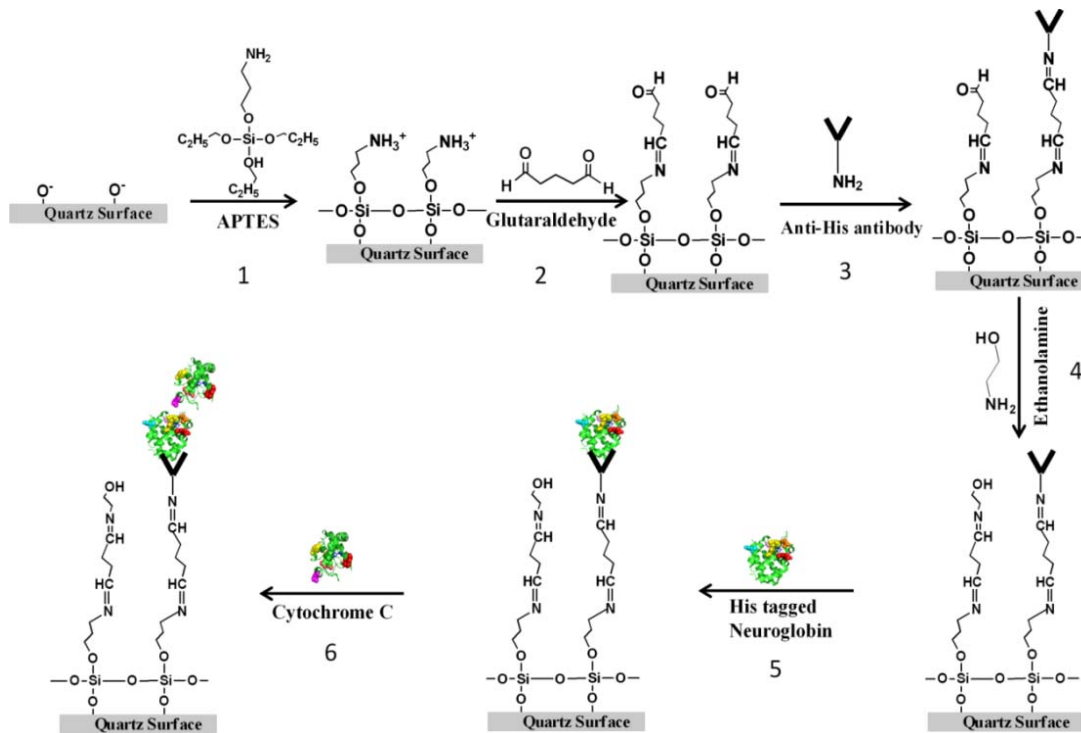
Figure 2.3: Schematic of the anti-His antibody surface modification method.

24

The following methods were used to characterize the chemical surface medication of the quartz nanopipette.

2.2.2.1: Ion current rectification (ICR)

Current-voltage data were used to determine ICR. As a consequence of its conical shape, the ionic current through the nanopipette is extremely sensitive to surface charge variation near the nanopipette tip [12]. Because of this fact, the I-V curves through these nanopipettes are not linear in bigger bias range bigger than 15 mV. The current at one bias polarity is larger than the current at the opposite bias polarity with the same magnitude. The phenomenon is regarded as ICR [13]. The chemical surface modification with (3-aminopropyl) triethoxysilane (APTES) and hNgb alters the nanopipette surface charge. To quantitatively compare the rectification, the definition of ICR (r) was used as $r = \log \left| \frac{I_+}{I_-} \right|$ [14].

2.2.2.2: Noise analysis

Noise analysis was also performed to characterize the nanopipette surface modification using current-time (I-t) traces. The I-t traces were measured by the Axon 200B instrument (Molecular Devices Inc.) operated in voltage clamp mode. An Axon Digidata 1440A was used to record ionic current time traces. All measurements were performed at room temperature.

The measurement setup, as shown in Figure 2.2c, was housed in a home-built Faraday cage, placed on an air floating mechanical table to reduce mechanical noise. The Ag/AgCl electrodes were used in all the ionic current measurements. The noise power spectrum density (PSD), S(f), was obtained by performing fast Fourier transformations

(FFT) of the current time trace (at V = -0.4V) for a nanopore, which were recorded at 250 kHz sampling rate with a bandwidth of 100 kHz. The noise spectrum was obtained by plotting PSDs ($S(f)/<I>^2$, where $<I>$ is the average current) for the same nanopore before and after modification. The noise at low frequency regime (f <100 Hz), which is called the 1/f noise or flicker noise, was only focused. The origin of this noise is still in debate but is assumed to be related to fluctuations in the charge carrier and surface charge [15-17]. The normalized S(f) in this frequency regime can be fitted by $S(f)/<I>^2 = A/f$, where A is the slope of the fitted curve.

2.2.2.3: SPR

In addition to ICR and noise analysis, SPR measurements (Section 2.1) were monitored for the confirmation of real time chemical surface modifications. As mentioned in Section 2.1.2.2, CA molecules were used to chemically modify the gold surface to form a SAM. The modification is analogous to chemical modification of quartz with APTES since both modifications result in an amine terminal group for the antibody immobilization.

2.3: Translocation through CNT nanopores

The following procedures were followed to investigate the translocation of small charged molecules through CNT nanopores.

2.3.1: Dry etching

A plasma RIE system (Harric Plasma, PDC-001) was used in dry etching. The etching time, gas selection and flow rate, and pressure were varied based on the etching results.

2.3.2: Wet chemical etching

All wet chemical etching processes followed during the fabrication of CNT based nanoporous membrane device are explained below.

2.3.2.1: Anisotropic KOH etching

Forty-five percentage (w/w) potassium hydroxide (KOH) solution in DI water was used for anisotropic etching of Si <100> wafers. Typically the etching process was completed in more than 6 hours. The KOH solution was continuously heated and stirred at 95°C and 240 rpm, respectively, throughout the etching process. A Teflon holder was used to hold the wafer in the KOH solution during the etching process. The beaker with KOH solution was covered with a glass dish containing cold water to prevent the rapid vaporization of the KOH solution. After 6 hours, the wafer was taken out, cleaned with DI water, dried with argon gas, and carefully checked under optical microscope to confirm the successful etching of Si. If the wafer was observed under-etched, the etching process was continued again untill free standing SiN membrane (300 nm or 325 nm thick) was left.

2.3.2.2: PAN etching

The PAN etching solution was made with the mixture of phosphoric acid, acetic acid, nitric acid, and water, respectively, in the ratio of 16:1:1:2. This solution was used to remove the metal catalysts deposited for CNT growth. The PAN etching was performed at 45°C for 5 minutes. The successful completion of the PAN etching was confirmed using optical microscope.

2.3.4: Fabrication of PDMS layer

A SYLGARD 184 silicone elastomer base and SYLGARD 184 silicone elastomer

curing agents, respectively, were mixed in the ratio of 10:1 (w/w). The mixture was kept in a desiccator connected to a continuous vacuum line untill the air bubbles were removed. The mixture was then poured on a petri dish and allowed to be cured at least overnight.

2.3.5: Fabrication and characterization of nanoporous membrane device

The following steps were followed in order to accomplish the fabrication of CNT based nanoporous membrane device to make it ready for the experiments. The Si/SiN substrate with vertically aligned CNTs grown (step 1), on free standing SiN membrane was used to fabricate the nanoporous membrane device. The CNTs were turned into a membrane via parylene coating after CNT growth (step 2). The parylene and free standing SiN membranes were etched, from the backside of CNT membrane using RIE (step 3) followed by PAN etching (step 4) in order to remove metal particles and used optical microscopy to confirm the successful etching. The substrate was then rinsed in DI water, dried with oxygen gas, and treated with the oxygen plasma (2–4 min, 7.2 W, 550–600 mTorr) to etch excess parylene (step 5) in order to open the CNT ends. The successful etching of parylene was confirmed via optical microscopy. The substrate was then sandwiched in between parafilm layers (step 6), followed by polydimethylsiloxane (PDMS) layers (step 7), and then plastic cuvettes (step 8). Each parafilm layer, PDMS layer, and plastic cuvette was drilled to make a hole for the fluidic pathway. Finally, the sandwiched assembly was tightened between two flat squared aluminum slabs (step 9). The fabrication steps (steps 1 to 3) were finished at Arizona State University (ASU).

Transmission electron microscopy (TEM) and SEM were used to characterize the CNTs. SEM was used to characterize the parylene coating (step 2) and etching (step 3).

These characterizations were accomplished at ASU in collaboration with Dr. Stuart Lindsay's research group. Gold nanoparticles (AuNPs) were used to test the leakage of the nanoporous membrane device. Porosity measurements using a KCl diffusion method [10] was also carried out for the characterization of the membrane device.

2.3.6: Data collection and analysis

The following data collection and analysis procedures were followed in order to investigate the translocation of small charged molecules.

2.3.6.1: Square wave voltammetry (SWV)

Square wave voltammetry was used in order to detect the small charged molecules translocated through CNT nanopores under the application of an electric field. In the current translocation study, two redox molecules, potassium hexacyanoferrate (III) and Tris (bipyridine) ruthenium (II) chloride were selected. The same electrochemical workstation and electrode assembly, as used in EIS measurements, was used in the SWV measurements with parameters: Initial potential = 0 V (for ferricyanide) and 0.6 V (for Ruthenium bipyridine), Final potential = 0.4 V to 0.6 V (for ferricyanide) and 1.4 V (for Ruthenium bipyridine), Increment = 0.004 V, Amplitude = 0.04 V, Frequency = 30 Hz, and Sensitivity = $1e^{-4}$ A/V. Typically, the redox molecules were dissolved in KCl solution. Therefore to detect the unknown concentration of the redox molecules in the solution, calibration curves were used, which were obtained by plotting peak current vs. the known concentration of the same redox molecule in the KCl solution (same KCl concentration as used in translocation experiments).

2.3.6.2: UV-vis spectroscopy

concentration of molecules in the solution, and to determine the concentration of translocated small ions as well as gold nanoparticles. For the determination of the concentration, Beer-Lambert law, was used which is given by Equation 2.4:

$$A = C \in L \tag{2.4}$$

where, A is the absorbance, $\in$ is the extinction coefficient of molecule of interest, and L is the path length, which is the length of quartz cuvette that I used during measurements. In my case, L = 1 cm.

2.3.6.3: Current-voltage (I-V) measurements

The Keithley 2636A sourcemeter (Keithley Instruments) was used to collect I-V data. All measurements were performed at room temperature. The measurement setup was housed in a home-built Faraday cage to reduce external noise. Ag/AgCl electrodes (prepared by dipping clean 0.2 mm diameter Ag wires in bleach for 30 minutes) were used in all the ionic current measurements. A constant bias was applied using a home-built LABVIEW software.

2.4: Theoretical simulations

In addition to label free experimental methods, the following theoretical simulations were also performed in this dissertation.

2.4.1: Simulation and analysis of biphasic SPR data

Mathematica software was used to simulate SPR sensorgrams, and Originpro 9.1 to fit the simulated SPR profiles and to perform error analysis. The SPR sensorgrams were generated by directly substituting the rate constants into the analytical solutions of the rate equations at a random noise with a standard deviation of 1 RU. Random noise

was added in order to simulate the experimental noises. Five SPR association profiles were generated for each analyte concentration. The analyte concentration was set to zero during the simulation of the dissociation profiles. The dissociation profiles were simulated five times in total.

2.4.2: Finite element based numerical simulations

Numerical simulations were carried out using Poisson-Nernst-Planck (PNP) equations ollowing the finite element method using the software package COMSOL Multiphysics 4.3b with chemical reaction engineering and AC/DC modules. The whole computation domain was discretized into free triangular elements and rigorous mesh refinements were adopted during simulations.

2.5: References

1. N.M. Mulchan, M. Rodriguez, K. O'Shea, Y. Darici, Sen. Actuators, B 2003, 88, 132.

2. W.D. Wilson, Science 2002, 295, 2103.

3. A.J. Tudos, R.B.M. Schasfoort, In: Handbook of Surface Plasmon Resonance, The Royal Society of Chemistry, 2008, 1.

4. K. Kukanskis, J. Elkind, J. Melendez, T. Murphy, G. Miller, H. Garner, Anal. Biochem. 1999, 274, 7.

5. M. Shi, "The construction and optization of a surface plasmon resonance sensor for the studies of bio-molecular interactions", PhD dissertation, Florida International University, 2011.

6. M.C. Leopold, E.F. Bowden, Langmuir 2002, 18, 2239.

7. Macdonald Website, http://jrossmacdonald.com/[February 2013], 2013.

8. Y.P. Shan, P.B. Tiwari, P. Krishnakumar, I. Vlassiouk, W.Z. Li, X.W. Wang, Y. Darici, S.M. Lindsay, H.D. Wang, S. Smirnov, J. He, Nanotechnology 2013, 24, 495102.

9. R. Tadmor, Langmuir 2004, 20, 7659.

10. M. Majumder, N. Chopra, B.J. Hinds, ACS Nano 2011, 5, 3867.

11. H. Wang, R. Bash, J.G. Yodh, G.L. Hager, D. Lohr, S.M. Lindsay, Biophys. J. 2002, 83, 3619.

12. P.B. Tiwari, L. Astudillo, J. Miksovska, X. Wang, W. Li, Y. Darici, J. He, Nanoscale 2014, 6, 10255.

13. H.S. White, A. Bund, Langmuir 2008, 24, 2212.

14. B. Vilozny, P. Actis, R.A. Seger, Q. Vallmajo-Martin, N. Pourmand, Anal. Chem. 2011, 83, 6121.

15. P. Chen, T. Mitsui, D.B. Farmer, J. Golovchenko, R.G. Gordon, D. Branton, Nano Lett. 2004, 4, 1333.

16. R.M.M. Smeets, U.F. Keyser, N.H. Dekker, C. Dekker, Proc. Nat. Acad. Sci. 2008, 105, 417.

17. D.P. Hoogerheide, S. Garaj, J.A. Golovchenko, Phys. Rev. Lett. 2009, 102, 256804.

CHAPTER 3: SURFACE PLASMON RESONANCE

Chapter 3 presents the optimization and use of a customized SPR instrument to determine the equilibrium dissociation constant (K_d) for protein-protein molecular interactions. Some of the contents of this chapter has been adapted from the manuscript, which is being prepared for publication [1].

3.1: Introduction

Several techniques such as SPR, fluorescence microscopy, and isothermal titration calorimetry (ITC) have been extensively used for the study of biomolecular interactions. Fluorescence microscopy requires the labeling of the molecule of interest. The chemically grafted foreign molecule may introduce artifacts in the experimental result. Isothermal titration calorimetry requires considerably higher sample concentration even to accomplish single experiment. On the contrary, SPR does not require labeling, and as compared to ITC it does not demand significantly higher sample concentration.

Surface plasmon resonance is a widely used label free biophysical technique to determine the equilibrium dissociation constant and the kinetics of bio-molecular interactions [2]. A SPR instrument has been optimized for the investigation of biomolecular interactions, including the determination of the K_d value. The immobilization of one of the interacting biomolecules onto the SPR sensor surface requires the successful chemical modification of the gold surface. Detail about the SPR instrument, including chemical modification and characterization strategies was presented in Section 2.1.

3.1.1: Principle of SPR

As a result of the Coulomb interaction between the valence electrons, collective plasma oscillation (surface plasma oscillations) occurs on the metal surface [3]. The quanta of surface plasma oscillations are called surface plasmons [4]. Most of the incident light gets total internally reflected when it passes from higher to lower transparent refractive index medium, at an incident angle above the critical angle. A part of the incident light leaks to the lower refractive index medium as an electric field. This electric filed wave is called evanescent field wave and the magnitude of this wave reduces exponentially as the distance from the interface increases [5]. The p-polarized component of the evanescent wave penetrates the interface when the interface is coated with a thin metal layer of suitable thickness. At a particular angle of incidence, the p-polarized light transfers its energy to surface plasmons increasing the intensity of electric field and causing drastic decrease in the intensity of the reflected light [5]. The phenomenon is known as the surface plasmon resonance and the corresponding angle of incidence is known as the SPR angle [6].

The propagation of constant (β) of the surface plasma wave along the metal surface is given by Equation 3.1[7,8]:

$$\beta_{sp} = k\sqrt{\frac{\varepsilon_m n_s^2}{\varepsilon_m + n_s^2}} \qquad (3.1)$$

where, k is the free space wave number, ε_m is the complex dielectric constant of the metal (gold), and n_s is the refractive index of dielectric medium. The parallel component of the wave vector $(\beta_{ev\,||})$ of the evanescent wave is given by Equation 3.2 [6]:

$$\beta_{ev\,||} = k\,n_g\,\sin\theta \qquad (3.2)$$

35

where, n_g is the refractive index of higher refractive index medium (glass prism) and θ is the incident angle. At the condition of SPR, β_{sp} equals to $\beta_{ev\,||}$. The SPR (θ_{SPR}) angle can now be calculated using Equation 3.3:

$$\theta_{SPR} = \sin^{-1}\left(\frac{1}{n_g}\sqrt{\frac{\varepsilon_m n_s^2}{\varepsilon_m + n_s^2}}\right) \qquad (3.3)$$

In my case, ε_m ($\varepsilon_m = n_m^2$, n_m is the refractive index of the metal) and n_g both are fixed. Therefore any change in the SPR angle is due to the change in n_s near the metal-dielectric interface [6].

3.1.2: Detection of biomolecular binding

The instrument (Section 2.1) that was used in this dissertation research follows Kretschmann's configuration [9] and the schematic of the configuration is shown in Figure 3.1a. Figure 3.1b shows a typical SPR curve. As explained in Section 2.1.1 and Equation 3.3, the SPR angle shifts (Figure 3.1b) are the result of the change in the refractive index near the sensor surface. Figure 3.1c represents the typical SPR sensorgram. The colored squares represent the corresponding position of SPR angles as shown in Figure 3.1b. The binding of biomolecules on the chemically modified sensor surface causes the change in the refractive index near the sensor surface thereby changing the SPR response (positions of brown and blue squares) relative to the SPR response for the buffer level (position of the red square). The initial stable buffer response as shown in Figure 3.1.c represents the SPR response prior to either ligand immobilization onto the sensor surface or to binding of analyte to the immobilized ligand. Based on the obtained sensorgrams (Figure 3.1c), further analysis can be performed.

The SPR instrument was optimized using various chemical surface modification techniques as explained in Section 2.1.2 in order to determine the affinity of the biomolecular interaction. The following sections in this chapter represent the determination of resolution of the SPR instrument, and the SPR results for the successful quantitative investigation of biomolecular interactions, taking human neuroglobin (hNgb) and cytochrome c from equine heart (Cyt c) and as a model proteins pair.
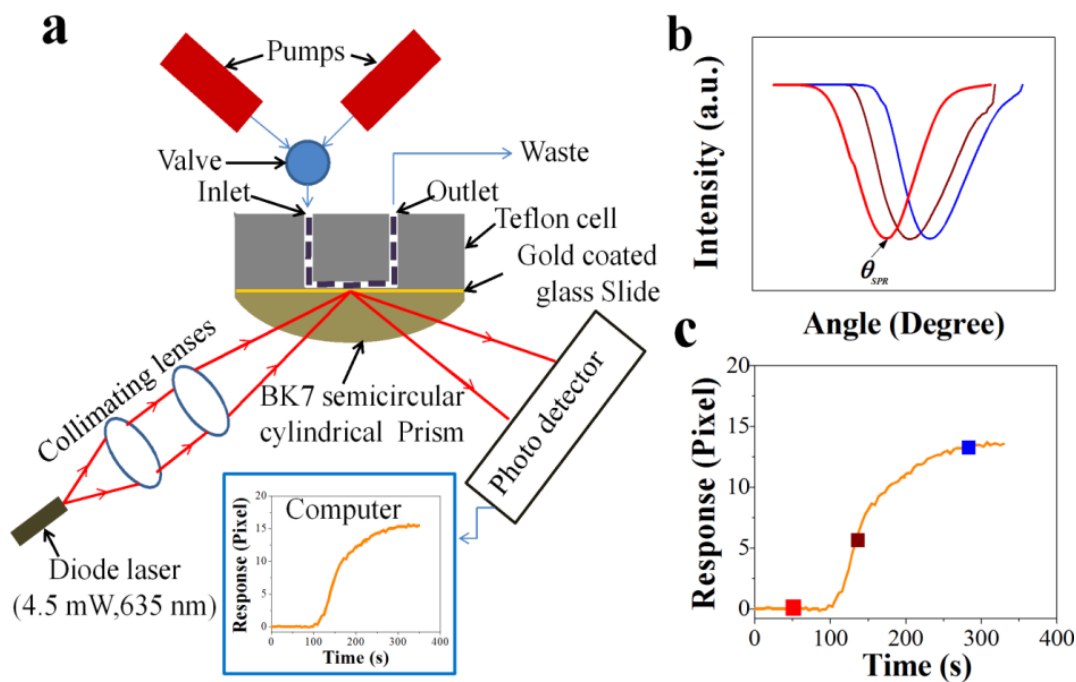
Figure 3.1: (a) Schematic of customized SPR setup. (b) Intensity of reflected light vs. incident angle plot (SPR curve). The SPR curves represent the SPR angle shift due to the change in refractive index on the sensor surface (Figures not to scale). (c) Typical SPR sensorgram. The colored squares represent the corresponding position of SPR dip as shown in Figure 3.1b.

3.2: Determination of resolution

Glycerol-water solutions at various glycerol percentages (v/v) mixed in DI water were prepared and degassed by sonication. The Lorenz-Lorenz relation (Equation 3.4) was used in order to determine the refractive index of glycerol-DI water mixtures [10]:

$$\frac{n_{12}^2-1}{n_{12}^2+2} = \varphi_1 \frac{n_1^2-1}{n_1^2+2} + \varphi_2 \frac{n_2^2-1}{n_2^2+2} \tag{3.4}$$

where, n_{12} is the refractive index of the mixture, n_1 is the refractive index of the glycerol, n_2 is the refractive index of the DI water, and φ_1 and φ_2 are the volume fractions. The volume fractions can be calculated using the relation: $\varphi_i = x_i \vartheta_i / \sum x_i \vartheta_i$, where, x_i is the mole fraction and ϑ_i is the molar volume of the ith component [10].
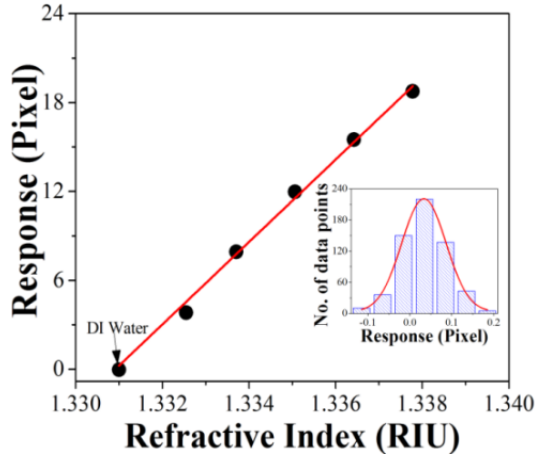
Figure 3.2: Response vs. refractive index plot. The black solid circles are the equilibrium SPR responses and the red continuous line is a linear fit. The inset is the histogram plot of SPR data points for 10 minutes. The red line is the Gaussian fit and the standard deviation of the Gaussian fit was treated as the baseline noise.

Using $n_1 = 1.473$ and $n_2 = 1.331$, the values for n_{12} were determined to be 1.33255, 1.33371, 1.33506, 1.33642, and 1.33778 for 1%, 2%, 3%, 4%, and 5% glycerol-DI water solutions, respectively. The SPR response (at equilibrium) for each solution was then plotted vs. the refractive index of the solution as shown in Figure 3.2. The slope from the linear fit (continuous line) of the data (black solid circles) was used to determine the bulk refractive index sensitivity, which was 2782 ± 101 Pixel/RIU. The baseline noise was calculated by fitting the histogram (continuous line, inset of Figure 3.2) of SPR data points measured for 10 minutes when only DI water was passed through the sensor

surface. The baseline noise was determined to be $(1.06 \pm 0.04) \times 10^{-1}$ pixel. Therefore, the minimum refractive index resolution equals $\frac{1}{2782 \pm 101}$ RIU/pixel $\times$ $(1.06 \pm 0.04) \times 10^{-1}$ pixel, which is $(3.81 \pm 0.20) \times 10^{-5}$ RIU. The resolution of SPR instrument is in used in the experiments is similar to the resolution of SPR instruments used by other research groups [11-13]. However, the resolution obtained for the SPR instrument used in the experiments is at least one order smaller compared to $\sim 10^{-6}$ RIU resolution of most of the commercial SPR instruments. The discrepancy in the resolution is mainly due to the result of relatively higher baseline noise. There are possibilities of optimizing the baseline noise by performing the experiments in a vibration-free laboratory setup, using a detector with larger number of linear array photodiodes, and by using noise reduction algorithms (using noise filters).

3.3: Cyt c-hNgb molecular interactions using customized SPR system

The Cyt c and hNgb pair was used as an interacting proteins pair to optimize the customized SPR instrument and to quantitatively investigate protein-protein interactions. The following subsections explain the SPR experimental details for the investigation of Cyt c-hNgb molecular interactions.

3.3.1: Overview

Neuroglobin (Ngb) is a hexa-coordinate heme protein that is predominantly expressed in the brain tissue [14]. In cultured neuronal cells, Ngb over-expression is up-regulated under conditions of neuronal hypoxia and ischemia [15]. In transgenic animals, Ngb over-expression reduces ischemic cerebral injury, and its knockdown increases infarct volume and worsens post-ischemic conditions [16]. Decreased Ngb expression

was associated with an increased risk of Alzheimer's dementia in humans [17]. The overall protein structure closely resembles to that of myoglobin (Mgb) with a characteristic three over three fold of α-helices [18]. As in other globins, Ngb reversibly binds small diatomic molecules, including O_2. In spite of the high affinity for oxygen, the low micromolar intracellular Ngb concentration in the neuronal tissue does not support a role as oxygen storage and/or transport protein [19]. On the basis of a rapid reaction of oxygen bound Ngb with nitric oxide forming ferric Ngb and nitrate anion, it was suggested that Ngb functions as an NO scavenger [20].

The unknown molecular mechanism of Ngb protective role stimulated a search for its interacting partners. Although in vivo and in vitro studies have identified several intracellular proteins as Ngb interacting partners, only few protein-protein complexes were characterized in terms of affinity constant and binding site identification. To better understand the molecular basis of interactions between Cyt c (an Ngb binding partner) and hNgb), the equilibrium dissociation constants (K_d) for the formation of Cyt c-Ngb complexes were determined using the customized SPR instrument.

Human Ngb (hNgb) and rat Ngb (rNgb) exhibit a high sequence homology (94%), though the rNgb structure lacks the disulfide bridge connecting Cys46 to Cys55 [21] due to the presence of a glycine (Gly) residue at position 46. Therefore, rNgb was selected in order to understand the impact of the internal disulfide bond between Cys46 and Cys55 and CD loop flexibility on the affinity between Cyt c and hNgb.

3.3.2: Materials and reagents

Ferric Cyt c, ferric hNgb and ferric rNgb were received from Dr. Miksovska's lab (Chemistry and Biochemistry, FIU), 16-mercaptohexadecanoic acid (MHA), 11-

mercapto-1-undecanol (MUO), Triethylene glycol mono-11-mercaptoundecyl ether (PEG-thiol), and nickel (II) sulfate hexahydrate, were purchased from Sigma-Aldrich; and ethanol (200 proof) from Decon Laboratories. N-hydroxysuccinimide (NHS), N-(3-dimethylaminopropyl)-N′-ethylcarbodiimide hydrochloride (EDC) were received from Thermo-Scientific and 2-{2-[2-(1-mercaptoundec-11-yloxy)-ethoxy]-ethoxy)-ethoxy nitrilotriacetic acid (NTA-thiol) from Prochimia Surfaces, Poland. All other reagents were purchased from Fisher Scientific and used as received. Solutions were prepared using deionized (DI) water (~18 MΩ, Ultra Purelab system, ELGA/Siemens). The polycrystalline gold chips (Section 2.1.1) were purchased from Platypus Technologies LLC.

3.3.3: Sensor preparation
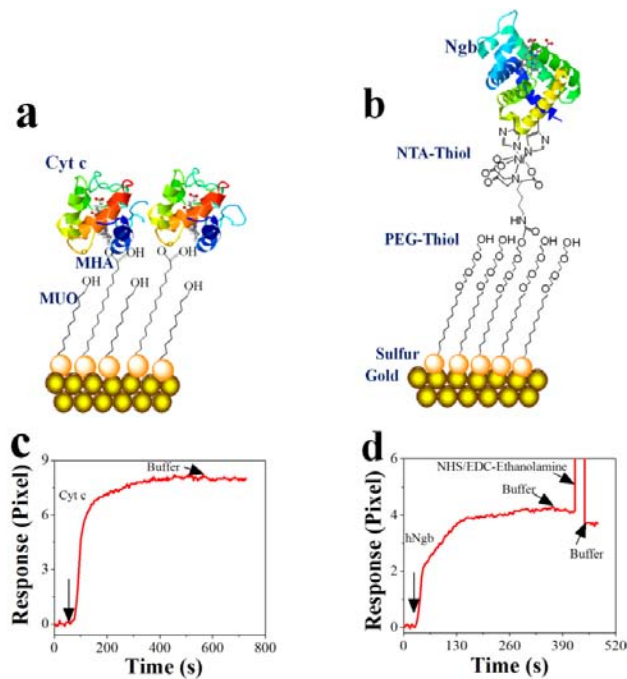
Figure 3.3: Cartoon scheme of gold surface modification: (a) mixed alkanethiols (MHA and MUO) followed by Cyt c immobilization (Cyt c PDB entry 1AKK), and (b) mixed NTA- and PEG-thiols followed by His-tagged Ngb immobilization (hNgb PDB entry 1OJ6). Representative SPR sensorgram showing: (c) covalent immobilization of Cyt c to MHA-MUO surface via NHS-EDC coupling chemistry, and (d) immobilization of His-tagged Ngb to Ni^{2+} chelated NTA surface.

The SPR sensor was prepared using the gold chip. The gold surface modification and characterization using MHA-/MUN-thiol and NTA-/PEG-thiol are explained in Section 2.1.2. The schemes for the surface modifications are shown in Figure 3.3. The modified sensor chip was then mounted in the SPR system (Section 2.1).

3.3.4: Protein Immobilization and Cyt c-Ngb binding

The immobilization of Cyt c to the MHA-MUO modified surface was achieved following NHS-EDC coupling chemistry via covalent linkage of Cyt c primary amines to the NHS-EDC activated -COOH surface (Figures 3.3a and 3.3c). The N-terminal His-tagged hNgb was immobilized onto the Ni^{2+} chelated NTA surface (Figures 3.3b and 3.3d). The immobilization of His-tagged proteins will be further explained in detail in Chapter 4. In order to detect the Cyt c-hNgb complex formation, buffered solutions of hNgb and Cyt c (different concentrations) were passed through the 20 μM Cyt c and 20 μM hNgb immobilized sensor surfaces, respectively, at a flow rate of 50 μL/min. Phosphate buffer (PB, 10 mM, pH 7.0) was used in all the binding experiments.

3.3.5: Data analysis

The observed SPR response (quasi-equilibrium) for each Cyt c-hNgb complex formation was plotted as a function of Ngb or Cyt c concentration. K_d values were determined by fitting the response vs. concentration plot to Equation 3.5 [22,23]:

$$R_{eq} = \frac{R_{max}[hNgb\ or\ Cyt\ c]}{K_d + [hNgb\ or\ Cyt\ c]} \tag{3.5}$$

where, R_{eq} is the equilibrium response, [hNgb or Cyt c] is the Ngb or Cyt c concentration, and R_{max} is the fitting parameter corresponding to SPR response at maximum analyte (Cyt c or hNgb) concentration.

3.3.6: Results and discussion

In this part of my dissertation research, a customized SPR instrument was optimized via the characterization of the molecular mechanism of Cyt c-Ngb complex formation. The K_d values for Cyt c association to hNgb and rNgb were derived. The results from two different surface modification strategies were also investigated.

Firstly, I examined bindings of hNgb and rNgb to covalently immobilized Cyt c onto an activated self-assembled monolayer (SAM) surface, via standard NHS-EDC coupling chemistry. Figure 3.4a represents the typical SPR sensorgrams for Cyt c-Ngb complex formation. A control experiment (Figure 3.4b, upper panel) was performed by flowing 30 μM buffered solution of Mgb over Au/SAM/Cyt c surface, under the similar condition as the results in Figure 3.4a. Mgb is a globular protein of a similar tertiary structure as Ngb but does not interact with Cyt c. Only a negligible increase in the SPR signal was detected for the Mgb association to Cyt c, more likely due to non-specific binding and/or bulk refractive index change. This result of not forming inter-protein complex between Cyt c and Mgb is consistent with the previous report suggesting no evidence of complex formation between these two proteins [24]. Since Cyt c has large number of amino acid residues with primary amines, the activated SAM surface more likely was fully covered with Cyt c. On the other hand hNgb has very small number of amino acid residues with primary amines. Therefore, an extra step of quenching NHS esters (after NHS/EDC activation of SAM) was not performed in the experiments as shown in Figure 3.4a. An experiment (Figure 3.4b, lower panel) with ethanolamine (0.2 M, pH 8.0) treatment (for 5 minutes) of the Cyt c immobilized surface also gave no indication of different result. Cyt c-Ngb binding experiments did not reach perfect

equilibrium state (Figure 3.4a), which is in consistent with previously observed results [25]. Therefore, for simplicity, I used quasi-equilibrium SPR response (gray shaded area, Figure 3.4a) to determine the K_d value.
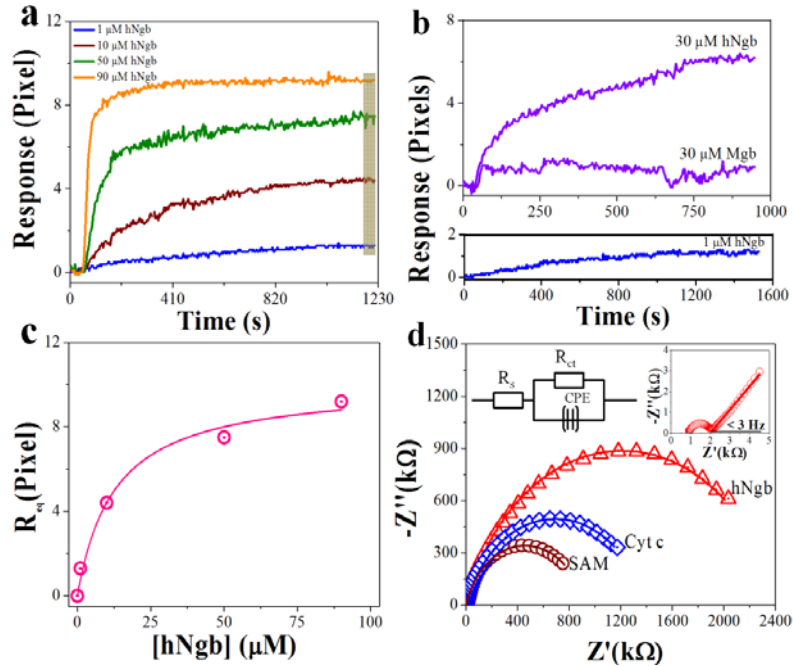
Figure 3.4: (a) Representative SPR sensorgrams for hNgb binding to immobilized Cyt c. The grey shaded area represents the quasi-equilibrium SPR response. (b) Upper panel- control experiment showing 30 mM myoglobin (Mgb) does not bind to immobilized Cyt c but binding of 30 mM hNgb to the immobilized Cyt c as shown in Figure 3.3a. Lower panel- Cyt c-hNgb complex formation after Cyt c immobilized surface (Figure 3.3c) was treated with NHS/EDC followed by ethanolamine. (c) Plot of quasi-equilibrium response (R_{eq}) vs. hNgb (circles) concentration. The continuous lines are the fit to Equation 3.5. (d) EIS results: Nyquist plots for successive gold surface modification. Symbols correspond to experimental data and the continuous lines show CNLS fit using the equivalent circuit model Equivalent circuit (left inset). The right inset represents the Nyquist plot for bare gold demonstrating a linear dependence at frequencies below 3 Hz. Symbols correspond to experimental data and the continuous line shows linear fit above 3 Hz.

The K_d value determined from this procedure should be approximately similar to the true K_d value since the progression of SPR sensorgrams is negligible after 800 s. The quasi-equilibrium SPR response values (symbols, Figure 3.4c) were plotted as a function of hNgb concentration and fitted (continuous line, Figure 3.4c) to Equation 3.5, which

resulted in a K_d value of ~13 μM. A K_d value of ~ 45 μM was reported previously for DTT reduced ferric Ngb binding to ferric Cyt c using SPR in Tris buffer [26].
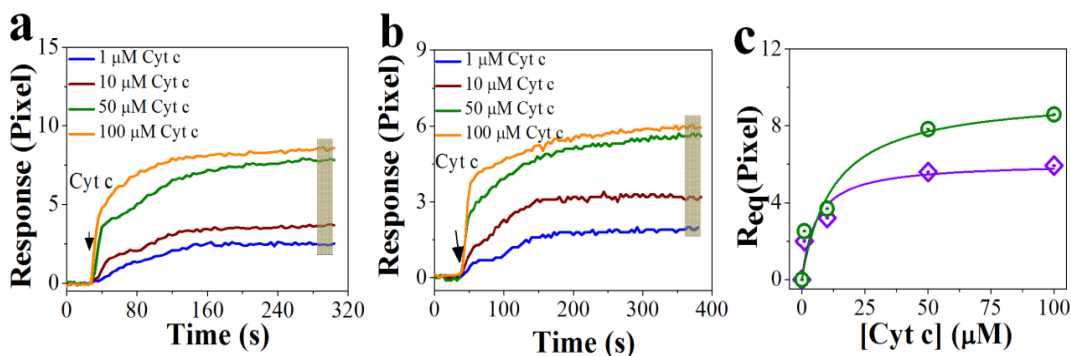
Figure 3.5: Representative SPR sensorgrams for Cyt c binding to the immobilized His-tagged Ngbs: (a) hNgb and (b) rNgb. The grey shaded area represents the quasi-equilibrium SPR response. (c) Plot of quasi-equilibrium response (R_{eq}) vs. analyte (hNgb-green circles and rNgb-violet diamonds) concentration. The continuous lines are the fit to Equation 3.5.

The formation of SAM, Cyt c immobilization to SAM, and Cyt c-hNgb complex formation surface were also verified by EIS measurements. A detailed explanation of EIS is given in Section 2.1.2.4, including data fitting and analysis. Results from EIS experiments are shown in Figure 3.4d. The semicircular diameter in the Nyquist plot (Figure 3.4 d) crudely determines the charge transfer resistance (R_{ct}) [27]. The R_{ct} value for bare gold (Semicircular part only, right inset of Figure 3.4d) is therefore ~2 kΩ. Except bare gold, other parameters were determined from fitting (Section 2.1.2.4) to equivalent circuit (left inset, Figure 3.4d). After SAM modification, the charge transfer resistance increased from 2 kΩ to 920 kΩ and from 920 kΩ to 1390 kΩ when Cyt c was immobilized onto an activated SAM. This confirms the successful SAM formation and Cyt c immobilization. Moreover, the charge transfer resistance increases from 1390 kΩ to 2420 kΩ when 30 μM hNgb was allowed to bind with Cyt c, confirming the Cyt c-hNgb complex formation.

Secondly, I followed the experiments with His-tag immobilization of Ngbs. This ensures homogeneous and predictable ligand orientation for His-tag immobilization [28]. Figure 3.3b represents the scheme for capturing of His-tagged Ngb onto Ni^{2+} chelated NTA surface. A detailed explanation of His-tagged protein immobilization will be given in Chapter 4. Figure 3.5a represents SPR sensorgrams for Cyt c binding to hNgb and Figure 3.5b for Cyt c binding to rNgb, at different Cyt c concentrations.

The analysis of SPR data (fitting to Equation 3.5, Figure 3.5c) resulted in comparable equilibrium dissociation constants for hNgb association to Cyt c ($K_d \sim 12$ μM) and rNgb ($K_d \sim 6$ μM). The K_d value (~12 μM) for Cyt c-hNgb molecular interactions obtained from experimental results with His-tag immobilization is very close to the K_d value (~13 μM) from random covalent immobilization. This shows that either of the two methods can comparably determine the affinity of the Cyt c-Ngb complex formation. Similar K_d values for hNgb and rNgb association with Cyt c indicated that the formation of the Cyt c-Ngb complex is not significantly perturbed by the conformational flexibility of the CD loop, which is restricted in hNgb [29].

3.4: Conclusions

The SPR instrument was optimized and used for its use to investigate protein-protein interactions (Cyt c-Ngb). The derived K_d value (~13 μM) was found in a general agreement with the previously published result. Based on the derived equilibrium dissociation constant (K_d), no significant impact of the internal disulfide bridge between Cys 46 and Cys 55 was found in the affinity of hNgb binding to Cyt c.

3.5: References

1. P.B. Tiwari, L. Astudillo, K. Pham, X. Wang, J. He, S. Bernad, V. Derrien, P. Sebban, J. Miksovska, Y. Darici, a) Evaluation of protein immobilization approached for SPR measurements, and b) Heme iron coordination regulated neuroglobin-cytochrome c complex formation.

2. W.D. Wilson, Science 2002, 295, 2103.

3. D. Pines, Rev. Mod. Phys. 1956, 28, 184.

4. E.A. Stern, R.A. Ferrell, Phys. Rev. 1960, 120, 130..

5. I.N. Serdyuk, N.R. Zaccai, J. Zaccai, Methods in Molecular Biophysics: Structure, Dynamics, and Function, Cambridge University Press, New York, 2007.

6. Y. Tang, X. Zeng, J. Liang, J. Chem. Educ. 2010, 87, 742.

7. J. Homola, S.S. Yee, G. Gauglitz, Sens. Actuators, B 1999, 54, 3.

8. H. Raether, Surface plasmons on smooth and rough surfaces and on gratings, Springer-Verlag, Berlin, 1988.

9. E. Kretschmann, Optics Commun. 1972, 6, 185.

10. R. Mehra, Proc. Indian Acad. Sci. (Chem. Sci.) 2003, 115, 147.

11. J.S. Shumaker-Parry, C.T. Campbell, Anal. Chem. 2004, 76, 907.

12. J. Homola, Chem. Rev. 2008, 108, 462.

13. K.M. Hansson, K. Johansen, J. Wetterö, G. Klenkar, J. Benesch, I. Lundström, T.L. Lindahl, P. Tengvall, Biosens. Bioelectron. 2007, 23, 261..

14. T. Burmester, B. Weich, S. Reinhardt, T. Hankeln, Nature 2000, 407, 520.

15. Y. Sun, K. Jin, X.O. Mao, Y. Zhu, D.A. Greenberg, Proc. Natl. Acad. Sci. U.S.A. 2001, 98, 15306.

16. Y. Sun, K. Jin, A. Peel, X.O. Mao, L. Xie, D.A. Greenberg, Proc. Natl. Acad. Sci. U.S.A. 2003, 100, 3497.

17. M. Szymanski, R. Wang, M.D. Fallin, S.S. Bassett, D. Avramopoulos, Neurobiol. aging 2010, 31, 1835.

18. B. Vallone, K. Nienhaus, A. Matthes, M. Brunori, G.U. Nienhaus, Proc. Natl. Acad. Sci. U.S.A. 2004, 101, 17351.

19. A. Fago, C. Hundahl, H. Malte, R.E. Weber, IUBMB Life 2004, 56, 689.

20. M. Brunori, A. Giuffrè, K. Nienhaus, G.U. Nienhaus, F.M. Scandurra, B. Vallone, Proc. Natl. Acad. Sci. U.S.A. 2005, 102, 8483.

21. D. Hamdane, L. Kiger, S. Dewilde, B.N. Green, A. Pesce, J. Uzan, T. Burmester, T. Hankeln, M. Bolognesi, L. Moens, M.C. Marden, J. Biol. Chem. 2003, 278, 51713.

22. S. Lin, A. Shih-Yuan Lee, C.-C. Lin, C.-K. Lee, Curr. Proteomics 2006, 3, 271.

23. P.B. Tiwari, T. Annamalai, B. Cheng, G. Narula, X. Wang, Y.-C. Tse-Dinh, J. He, Y. Darici, Biochem. Biophys. Res. Commun. 2014, 445, 445.

24. C.-S.C. Wu, P. Duffy, W.D. Brown, J. Biol. Chem. 1972, 247, 1899.

25. K.M. Henty, "A Role for Neuroglobin in the Inhibition of Cytochrome c-Mediated Apoptosome Formation", Dissertation, University of Auckland, 2011.

26. S.H. Bønding, K. Henty, A.J. Dingley, T. Brittain, Int. J. Biol. Macromol. 2008, 43, 295.

27. Y.P. Shan, P.B. Tiwari, P. Krishnakumar, I. Vlassiouk, W.Z. Li, X.W. Wang, Y. Darici, S.M. Lindsay, H.D. Wang, S. Smirnov, J. He, Nanotechnology 2013, 24, 495102.

28. L. Nieba, S.E. Nieba-Axmann, A. Persson, M. Hämäläinen, F. Edebratt, A. Hansson, J. Lidholm, K. Magnusson, Å.F. Karlsson, A. Plückthun, Anal. Biochem. 1997, 252, 217.

29. A.D. Nadra, M.A. Martí, A. Pesce, M. Bolognesi, D.A. Estrin, Proteins: Struct., Funct., and Bioinf. 2008, 71, 695.

CHAPTER 4: A SURFACE PLASMON RESONANCE STUDY OF THE INTER-MOLECULAR INTERACTION BETWEEN *Escherichia coli* TOPOISOMERASE AND pBAD/Thio SUPERCOILED PLASMID DNA

In Chapter 3, I discussed the optimization of customized SPR instrument for the analysis of biomolecular (protein-protein) interaction, including determination of the equilibrium dissociation constant (K_d). This chapter presents the ability of the optimized customized SPR instrument for label-free characterization of the molecular interaction between *Escherichia coli* topoisomerase I (EctopoI) and pBAD/Thio supercoiled plasmid DNA. The majority of the content of this chapter has been adapted from my research work published in a peer reviewed paper [1].

4.1: Introduction

The drug resistance of bacterial pathogens to available antibacterial drugs is a serious public health issue and needs to be addressed. The bacterial topoisomerase I, a DNA topoisomerase I (topoI), is a novel target biomolecule for the discovery of new antibacterial drugs [2,3]. DNA topoisomerases play important roles on both the supercoiling control of DNA and the resolution of topological barriers during replication, transcription, and recombination [4-6]. The supercoiling tension caused by translocation of RNA polymerase must be relieved by topoisomerase [7,8]. Topoisomerase I cleaves and rejoins a single DNA strand during topoI-DNA reactions [9], which establishes a transient covalent linkage between these two macromolecules. These complexes can be trapped using topoisomerase inhibitors [4,9].

Topoisomerase I can catalyze interconversion of various topological isomers [10] and type IA topoisomerase catalytic activity requires Mg^{2+}[11]. In *Escherichia coli*,

EctopoI removes excess negative supercoils in order to regulate DNA supercoiling [12]. EctopoI is a single polypeptide of 865 amino acids and tyrosine 319 is the active site tyrosine in EctopoI that forms a transient covalent linkage to DNA 5' phosphoryl group during EctopoI-DNA reaction [13]. I quantitatively studied the interactions for EctopoI-pBAD/Thio supercoiled plasmid DNA (hereafter termed as pBAD/Thio) and Mg^{2+} bound EctopoI (Mg^{2+}EctopoI)-pBAD/Thio using the surface plasmon resonance (SPR) technique.

SPR is a widely used label free technique to determine equilibrium dissociation constants and the kinetics of bio-molecular interactions [14]. The sensor surface modification for the SPR assay was confirmed by using electrochemical impedance spectroscopy (EIS). The equilibrium dissociation constant (K_d) for EctopoI binding to pBAD/Thio was determined to be about 8 nM. A slightly higher K_d (~15 nM) value was obtained for Mg^{2+}EctopoI-pBAD/Thio interactions. In addition, the dissociation rate constants (k_d) for the interactions between the enzymes (EctopoI or Mg^{2+}EctopI) and pBAD/Thio were also derived and a larger k_d was obtained for Mg^{2+}EctopoI-pBAD/Thio interactions. These results can help us further understand the important role of Mg^{2+} in the interactions between EctopoI and DNA substrate during catalysis [15].

Mycobacterial tuberculosis topoisomerase I (MttopoI), has a different C-terminal DNA binding domain (CTD) that lacks the three Zn^{2+} binding motifs in the CTD of EctopoI [16]. Binding of the two enzymes, EctopoI and MttopoI, to pBAD/Thio plasmid DNA were compared. Under my experimental conditions, weak SPR signals were observed for interactions between MttopoI and pBAD/Thio. Therefore, the K_d value could not be recovered for MttopoI-pBAD/Thio interactions.

4.2: **Materials and methods**

4.2.1: Materials

Triethylene glycol mono-11-mercaptoundecyl ether (PEG-thiol), nickel (II) sulfate hexahydrate, sodium, chloride, potassium hexacyanoferrate (III) and ethanolamine HCL were purchased from Sigma-Aldrich, ethanol (200 proof) from Decon Laboratories LLC, 2-{2-[2-(1-mercaptoundec-11-yloxy)-ethoxy]-ethoxy)-ethoxy nitrilotriacetic acid (NTA-thiol) from Prochimia Surfaces, Poland and potassium ferrocyanide trihydrate from Acros Organics. N-hydroxysuccinimide (NHS), N-(3-dimethylaminopropyl)-N′-ethylcarbodiimide hydrochloride (EDC) and GeneJET Plasmid Maxiprep Kit were received from Thermo-Scientific. N-terminal recombinant EctopoI and MttopoI, and pBAD/Thio were received from Dr. Yuk-Ching Tse-Dinh's lab at FIU. All other reagents were purchased from VWR international, USA. Solutions were prepared using deionized (DI) water (~18 MΩ, Ultra Purelab system, ELGA/Siemens or Milli-Q Direct 8 water system). The polycrystalline gold chips (Section 2.1.1) were purchased from Platypus Technologies, LLC and each chip was cut into two halves before further processing.

4.2.2: Methods

4.2.2.1: Sensor preparation and characterization

The cleaning of gold chip and formation of SAM with NTA- and PEG-thiols are explained in Section 2.1.2.3. The formation of SAM on the cleaned gold surface was confirmed by electrochemical impedance spectroscopy (EIS). A frequency range from 10^{-1} Hz to 10^4 Hz was used during EIS measurements. A detailed explanation of EIS experiments can be found in Section 2.1.2.4. The surface modification was also

confirmed by contact angle measurements. The procedure for the contact angle measurements is explained in the Section 2.1.2.4. Figure 4.1a shows the scheme of SAM formation and His-tagged EctopoI or MttopoI immobilization.

4.2.2.2: Enzyme immobilization and DNA binding

The prepared sensor chip (Section 2.1.2.3) was mounted inside the SPR flow cell (Section 2.1.1). The sensor surface was activated using a 40 mM nickel (II) sulfate solution prepared in DI water for 2 minutes at a flow rate of 50 µL/min followed by DI water flushing for two minutes. The surface was then equilibrated with the HEPES buffer for 5-10 minutes. His-tagged EctopoI (2 µM) or MttopoI (2.5 µM) was immobilized on the activated SAM surface at a flow rate of 50 µL/min. Sequential treatment of the EctopoI or MttopoI immobilized surface was accomplished with a pulsed injection of NHS-EDC solution (25 mM NHS and 100 mM EDC) in DI water followed by 1 M ethanolamine (pH 8.2) in DI water. This treatment allowed me to achieve the baseline stability. The experiments with various pBAD/Thio concentrations were accomplished by regeneration of the sensor surface using 1M NaCl. For the experiments involving Mg^{2+}, 0.5 mM $MgCl_2$ (in Tris buffer, pH 8.0) was passed over EctopoI immobilized surface for 5 minutes. All the experiments were carried out at $22^{o}C$.

4.2.2.3: Data analysis

Complex non-linear least square (CNLS) fitting algorithm was used for EIS data using an equivalent circuit model (Figure 3.4d). Equilibrium data analysis methods were used to analyze the SPR data [17]. The equilibrium SPR response was plotted as the function of pBAD/Thio concentrations. In order to determine K_d, the plotted data was fitted to a simple nonlinear hyperbolic (SNLH) equation (Equation 4.1):

$$R = \frac{R_{max}[DNA]}{K_d + [DNA]} \qquad (4.1)$$

where, R is the equilibrium response, [DNA] is the analyte (pBAD/Thio) concentration, K_d is the equilibrium dissociation constant, and R_{max} is the fitting parameter representing the response at very high pBAD/Thio concentration.

The dissociation rate constants are obtained by fitting the SPR dissociation profiles using the exponential dissociation rate equation given below [18],

$$R_t = R_o e^{-k_d (t - t_o)} \qquad (4.2)$$

where, R_t is response at any time t, R_o is the response at $t = t_o$ (start of dissociation) and k_d is dissociation rate constant. R_o and t_o were fixed during the fitting. To avoid the artifact due to refractive index changes during the start of the dissociation process, entire SPR dissociation profiles were not fitted to Equation 4.2. Assuming $t_o = 0$ s, at the start of dissociation, Equation 4.2 can be modified by taking the logarithm on both sides as,

$$\ln\left(\frac{R_o}{R_t}\right) = k_d t \qquad (4.3)$$

and therefore the plot of $\ln\left(\frac{R_o}{R_t}\right)$ vs. t should produce a straight line.

4.3: Results

4.3.1: Sensor surface characterization

As shown in Figures 4.1b and 4.1c, the EIS experimental data (symbols) are fitted (continuous lines) using the equivalent circuit (inset, Figure 4.1c). The parameters obtained from fitting are listed in Table 4.1. The charge transfer resistance (R_{ct}) for SAM modified gold is significantly higher (~1060 kΩ) compared to cleaned unmodified (bare) gold (~0.5 kΩ). This significant difference in R_{ct} value clearly confirms the successful modification of the gold surface.
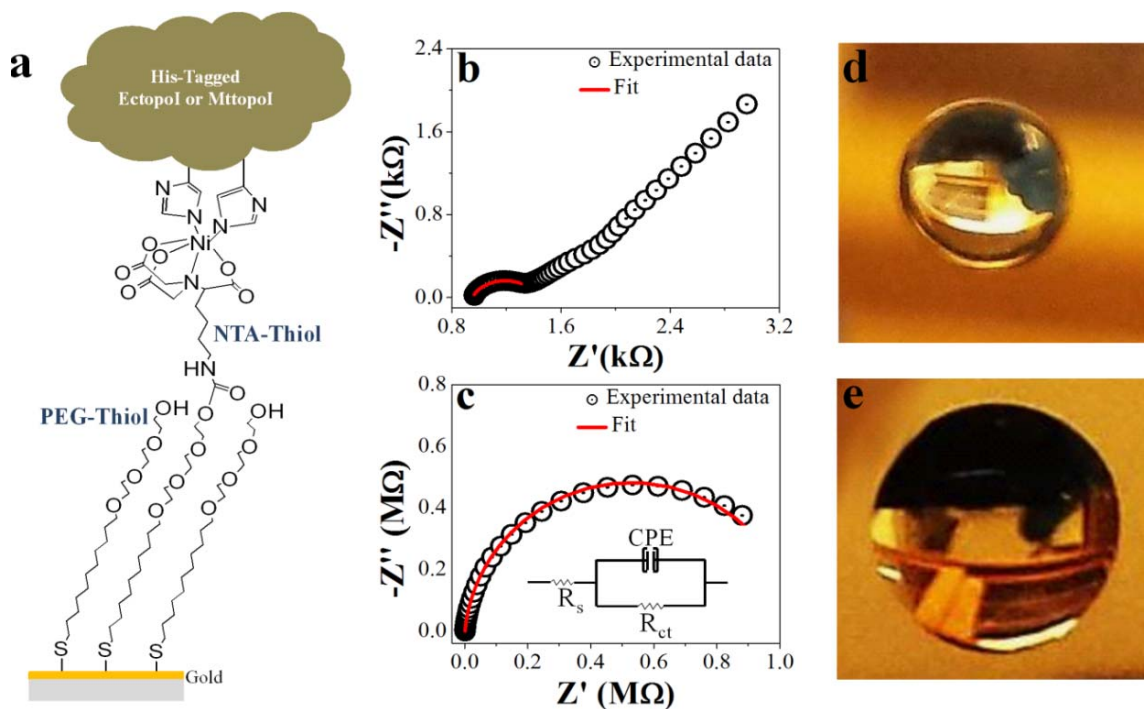
Figure 4.1: (a) Scheme showing the sensor surface modification with mixed thiols followed by the His-tagged EctopoI or MttopoI immobilization. (b) Electrochemical Impedance Spectroscopy (EIS) for the cleaned bare gold. (c) EIS for SAM modified gold surface, inset: equivalent circuit for EIS data fitting and analysis. In both Figures b and c, the symbols are experimental data and continuous lines are the CNLS fit. Cell phone images of 5 µL water drop on (d) cleaned gold and (e) SAM modified gold.

Moreover, due to the presence of SAM on the gold surface, the interfacial capacitance (C) for modified surface is obviously reduced (313nF) compared to clean gold (1227 nF). The contact angle for the water drop on clean bare gold (Figure 4.1d) is $82^o \pm 6^o$ and the contact angle for the water drop on SAM modified gold is $29^o \pm 2^o$. The significant reduction in the contact angle also confirms the formation of SAM on gold surface.

Surface	C (nF)	R_{ct} (kΩ)	R_s (kΩ)	α
Au	1227±122	0.48±0.08	0.95±0.04	0.75±0.01
Au/SAM	313±3	1060±10	0.93±0.08	0.94

Table 4.1: The parameters obtained by CNLS fitting of EIS experimental data to an equivalent circuit (Inset, Figure 4.1c). The errors are the standard errors of the fitting.

4.3.2: Enzyme immobilization and pBAD/Thio binding
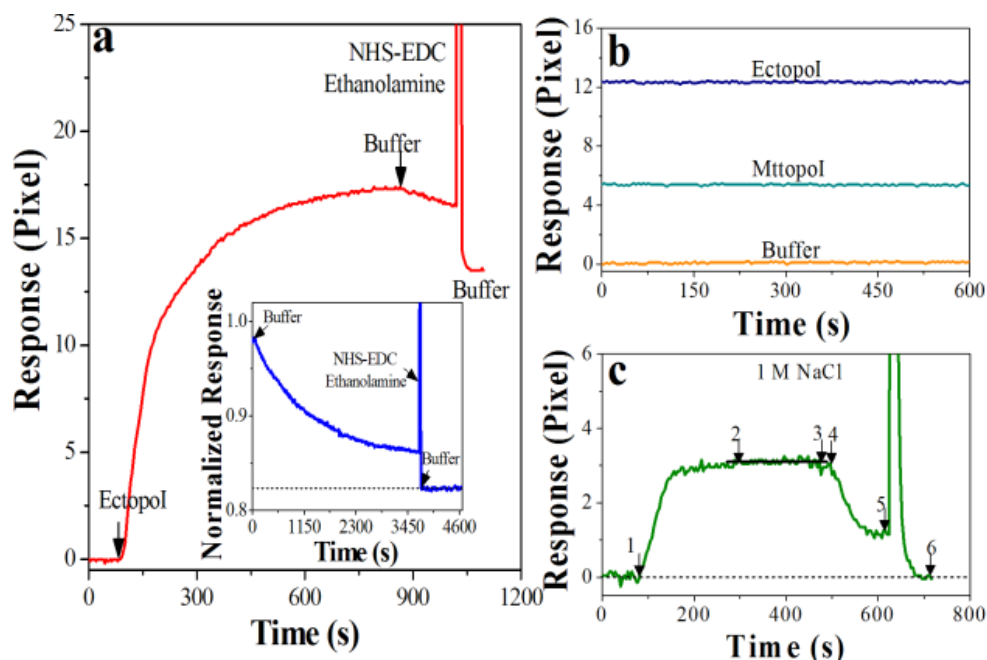
Figure 4.2: (a) SPR sensorgram for the immobilization of EctopoI. The arrows show the start of immobilization and buffer wash. Inset: Normalized response vs. time for a separate experiment showing the SPR response before and after NHS-EDC followed by ethanolamine treatment. (b) Representative SPR signals showing stability of sensor surface before and after immobilization of the enzymes. (c) Representative SPR profile for EctopoI-pBAD/Thio interaction: 1 to 2 association, 2 to 3 saturation, 3 to 4 minor signal shift due to manual changing of valve, 4 to 5 dissociation, and 5 to 6 regeneration.

As explained in the Methods section, both EctopoI (Figure 4.2a) and MttopoI (data not shown) were immobilized onto the Ni^{2+} chelated NTA surface. The inset in the Figure 4.2a represents the SPR signal for a separate experiment showing the SPR signal drift before NHS-EDC followed by ethanolamine treatment. Following EctopoI (or MttopoI) immobilization, before the treatment the baseline signal strength decreases continuously. However, after the treatment, the baseline stability was achieved. Figure 4.2b depicts the sensor surface stability after chemical treatment of the enzyme immobilized surfaces with NHS-EDC followed by ethanolamine treatment. Figure 4.2c is the representation of pBAD/Thio binding to the EctopoI enzyme immobilized sensor

surfaces, including association, saturation and dissociation of SPR signal. The sensor surface was regenerated using 1 M NaCl solution.

4.3.3: pBAD/Thio molecular interaction with EctopoI, Mg^{2+}EctopoI and MttopoI
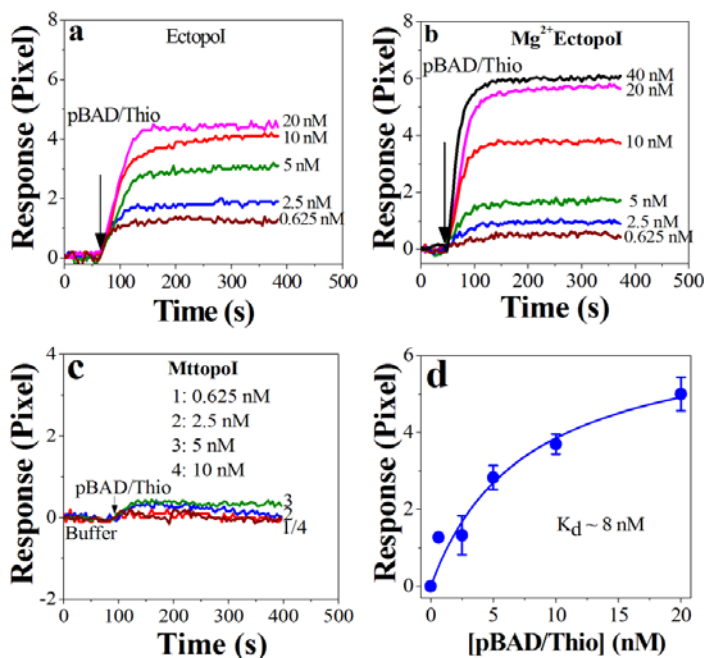
Figure 4.3: SPR sensorgrams for (a) pBAD/Thio binding to EctopoI, (b) for pBAD/Thio binding to Mg^{2+} bound EctopoI and (c) for pBAD/Thio binding to MttopoI. (d) Plot of equilibrium SPR response vs. pBAD/Thio concentration. The symbols are average experimental data of three different measurements with error bars as standard deviation and the continuous lines are the simple hyperbolic fit (Equation 4.1).

The concentration-dependent pBAD/Thio binding to EctopoI and Mg^{2+}EctopoI are shown in Figure 4.3a and 4.3b, respectively. Under my experimental conditions, the pBAD/Thio did not show a considerable response change upon its binding to MttopoI (Figure 4.3c). The SNLH fitting, using Equation 4.1, to the plot of equilibrium response vs. concentration of pBAD/Thio (Figure 4.3d) provides quantitative information of the interaction; more precisely, the K_d can be derived. The K_d value obtained from the fit was about 8 nM for EctopoI-pBAD/Thio interactions and a slightly higher K_d value (~15 nM)

for Mg^{2+}EctopoI-pBAD/Thio interactions was obtained. I could not obtain quantitative information for MttopoI-pBAD/Thio interactions.

4.3.4: Effect of Mg^{2+} on EctopoI-pBAD/Thio molecular interaction

To study the effect of Mg^{2+}, the SPR dissociation signals were fitted using the exponential dissociation rate constant equation as explained in the Methods section. For the SPR traces shown in Figures 4.3a and 4.3b, the dissociation SPR signals were recorded for data fitting and analysis.
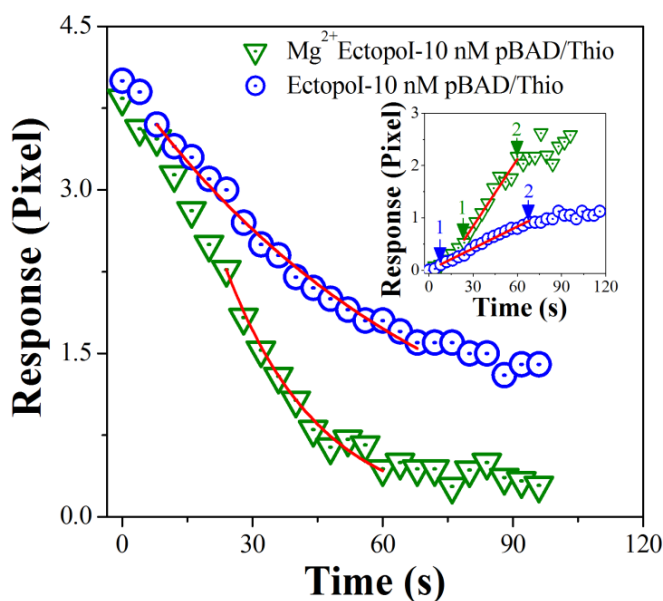
Figure 4.4: Representative SPR dissociation profiles fitted to exponential dissociation rate equation (Equation 4.2). The symbols are experimental data and the continuous lines are the best fit to Equation 4.2. Inset: Plot of $\ln\left(\frac{R_o}{R_t}\right)$ vs. t in order to find the most linear data rage. The data in the range between 1 and 2 were identified as the best data fitting range (most linear part). The symbols are experimental SPR responses converted to logarithmic data (Equation 4.3) and the continuous lines are the linear fit to Equation 4.3.

The most linear data range, excluding the starting data, from this plot of $\ln\left(\frac{R_o}{R_t}\right)$

vs. t (Figure 4.4, inset) was identified as the data range to fit to the unmodified (original) SPR dissociation signals using Equation 4.2. The k_d values were derived by fitting the

data to Equation 4.2. Due to the very weak dissociation signal, 0.625 nM and 2.5 nM DNA data were not used for this fitting. Since EctopoI-pBAD/Thio binding experiments were finished at 20 nM DNA concentrations, k_d values were derived by fitting 5 nM, 10 nM and 20 nM data. As shown in Figure 4.4, stronger dissociation signals were observed for Mg^{2+}EctopoI-pBAD/Thio interactions compared to EctopoI-pBAD/Thio-EctopoI interactions. The derived dissociation rate constant (k_d) value for EctopoI-pBAD/Thio interactions was ~0.017 s^{-1} and for Mg^{2+}EctopoI-pBAD/Thio interactions was ~0.043 s^{-1}. Compared to EctopoI-pBAD/Thio interactions, a larger k_d value for Mg^{2+}EctopoI-pBAD/Thio interactions suggests that the rate of enzyme turnover following DNA religation during catalysis of EctopoI- pBAD/Thio relaxation reaction is enhanced in the presence of Mg^{2+}.

4.4: Discussion

Recognizing EctopoI as an important target biomolecule for the discovery of new antibacterial drugs [2], EctopoI-plasmid DNA interactions were quantitatively studied for the first time (to the best of my knowledge) using SPR, a surface based affinity technique. In the SPR technique, the sensor surface modification plays a crucial role for the minimization of non-specific binding and reproducibility of SPR signals. I carried out EIS and contact angle measurements to confirm the gold surface modification via the mixed thiols. The efficient charge (electron) transfer between the redox couple and the working electrode in solution is basically evaluated by charge transfer resistance (R_{ct}) determination. The R_{ct} value obtained either from fitting or crudely from the semicircular diameter (Figures 4.1b and 4.1c) [19], for Au surface is much smaller compared to Au/SAM surface (Table 4.1). This clearly confirms the successful sensor surface

modification. My data also shows that the interfacial capacitance (C) decreases as the surface thickness increases because of the surface modification (Table 4.1). Moreover, the reduction of contact angle for 5 µL water drop from clean bare gold (Figure 4.1d) to SAM modified gold (Figure 4.1e) can also confirm the formation of SAM on the gold surface. The successful immobilization of EctopoI or MttopoI on the modified sensor surface was achieved via histidine tag (His-tag) capture method. Previously reported result shows that the single His-tag has a weak affinity (~1 µM) to the Ni^{2+}-NTA surface [20]. Even immobilized hexahistidine tagged proteins would dissociate upon continuous buffer flushing (Figure 4.2a, inset), and this phenomenon is not suitable for protein-small molecule interaction studies [21]. The immobilized enzyme surface must therefore be stable. This could be achieved by chemical treatment of the enzyme immobilized surface with sequential flow of NHS-EDC and ethanolamine solutions (explained in Methods). According an application note [22], even though, the primary amines (side chain terminal groups) in the immobilized proteins are modified due to a treatment for similar purpose (baseline stability), but, the resulting binding sites after stabilization should be sufficient for kinetic characterization. 30 µL of each (NHS-EDC and ethanolamine) solution was injected as a pulse for 20 seconds. Figure 4.2a shows the EctopoI (and MttopoI, data not shown) immobilization onto the sensor surface. In my case I did not have –COOH groups together with –NTA groups on the sensor surface, however, the treatment with NHS-EDC followed by ethanolamine allowed me to achieve the baseline stability as what was achieved in the previous report [21]. I, therefore, named this immobilization of His-tagged EctopoI (or MttopoI), explained here, as capture covalent immobilization. The mechanism that maintained the baseline stability was not very clear to me. However, this

59

might be due to the activation of primary –COOH groups of amino acid residues forming NHS ester that covalently linked with primary amines of nearby immobilized enzymes, thus forming the stable layer. Alternatively, the pulsed injection (NHS-EDC and more precisely, the concentrated, 1 M, ethanolamine solution) quickly removed the loosely and non-specifically bound enzymes thereby maintaining baseline stability. The first speculation is less likely because the ratio of NTA-SAM and PEG-SAM was 1:9, which ensures that the immobilized protein molecules are not very near to couple to each other. As shown in Figure 4.2b, the SPR response was found to be stable for 10 minutes before and after the treatment of EctopoI and MttopoI immobilized surfaces and thus guarantees the sensor surface stability and the successful capture covalent immobilization of the enzymes.

Figures 4.3a shows the interaction of EctopoI-pBAD/Thio in a concentration dependent manner. The EctopoI-pBAD/Thio binding responses saturated quickly; therefore an equilibrium analysis method could easily produce the K_d value via SNLH fitting (Figure 4.3d). The K_d value for EctopoI-pBAD/Thio interactions was found to be about 8 nM. A slightly higher K_d value (~15 nM) was obtained for Mg^{2+}EctopoI-pBAD/Thio interactions. For the experiments shown in Figures 4.3a and 4.3b, except for 40 nM data, each SPR trace was repeated three times. Due to sample limitation, the 40 nM data was not repeated. After saturated SPR responses were achieved, dissociation SPR profiles were recorded for some experiments. Buffer flushing could dissociate the EctopoI-pBAD/Thio complex considerably. The covalent topoisomerase-DNA complex is transient and reversible in nature [5]. Treatment of the topoisomerase-DNA complex with high salt would promote dissociation of the DNA from enzyme following relegation

[23]. After desired SPR signals were recorded, the surface was treated using 1M NaCl (in DI water) via pulsed injection for 2-3 minutes. This could successfully regenerate the surface to the initial (buffer) level and the surface was ready for next pBAD/Thio concentration. Figure 4.2c shows a typical SPR sensorgram showing association, saturation and dissociation of enzyme-pBAD/Thio interaction followed by regeneration. It should be noted that 10 mM Tris (pH 8.0) buffer was used as running buffer for enzymes-pBAD/Thio interaction experiments. The immobilized enzyme surfaces were equilibrated with the Tris buffer, for approximately 5 minutes, before pBAD/Thio injection. The experiments for each enzyme were performed either on the same chip or on different sensor chips. The variation of chip surfaces resulted in a variation of equilibrium response (lowest to highest) of ~0.6 pixels, on an average, in these experiments.

In order to understand the influence of the topoI C-terminal domain (CTD) sequence on the interactions between topoI and supercoiled plasmid DNA, we also studied the interaction between MttopoI and pBAD/Thio using SPR. There are tetracysteine Zn^{2+} binding motifs [24] that follow the N-terminal 67 kDa transesterification domain in EctopoI [25]. The three tetracysteine motifs are part of a DNA-binding domain at the C-terminus of EctopoI [26]. Unlike EctopoI [27], MttopoI lacks Zn^{2+} coordination and has evolved to have a different CTD sequence [16]. Under my experimental conditions, I could not see the concentration dependent interaction for MttopoI-pBAD/Thio interactions. As shown in Figure 4.3c, weak SPR signals were observed instead. This result suggests that the tetracysteine Zn^{2+} binding motifs are required for observing the interaction with plasmid DNA with the SPR protocol described

here. *Mycobacterium smegmatis* topoisomerase I (MstopoI) has a CTD similar to MttopoI that also does not coordinate Zn^{2+} [16]. Previous reports indicate that MstopoI CTD interacts with DNA during catalysis [28] and is responsible for sequence specific recognition of duplex DNA by MstopoI [29]. Because of its specific interaction with duplex DNA sequence, the *Mycobacterium topoisomerase* CTD may not be as efficient in promoting high affinity binding to the single-stranded DNA region in supercoiled plasmid DNA as the CTD in EctopoI. Alternatively, the result observed here might be due to the loss of MttopoI activity during protein immobilization. The dialyzed MttopoI sample used for protein immobilization was assayed for relaxation activity and found to be active (data not shown, this experiment was performed in Dr. Tse-Din's lab at FIU).

It has been revealed from the crystal structure of the 67 kDa N-terminal fragment of EctopoI that there is presence of acidic and basic amino acid residues nearby the active site region [30]. It has also been proposed that Lys-13 and Arg-321 (both basic residues) participate in DNA cleavage [31,32] and three acidic residues Asp-111, ASP-113, and Glu-115 coordinate with Mg^{2+} [33]. I could not detect the concentration dependent Mg^{2+} binding to EctopoI, which might be the limiting case of our SPR systems to resolve the detection of very small molecular weight ions/molecules-protein interactions. I also did not analyze our SPR sensorgrams for association rate constant measurements due to rapid association and fast saturation of the SPR signals. Therefore, to better understand the effect of Mg^{2+} coordination, the SPR dissociation profiles were recorded for the SPR sensorgrams shown in Figures 4.3a and 4.3b. These SPR profiles were fitted to the exponential dissociation rate constant equation. The fitting procedure is explained in detail in Methods. A larger dissociation rate constant (k_d) (~0.043 s^{-1}) was obtained for

Mg^{2+}EctopoI-pBAD/Thio compared to EctopoI-pBAD/Thio interactions (~0.017 s^{-1}). This increase in k_d value confirms that EctopoI catalytic activity is enhanced with Mg^{2+}. This is consistent with the role of Mg^{2+} to increase the dissociation rate constants for type IB topoisomerase I-DNA interactions, as reported previously [15]. Such analysis for type IA topoisomerase-DNA interactions has not been previously reported.

4.5: Conclusions

The quantitative study of EctopoI-pBAD/Thio interaction has been accomplished for the first time (to the best of my knowledge), using a customized SPR. A slightly higher equilibrium dissociation constant (K_d) a larger dissociation rate constant (k_d) for Mg^{2+}EctopoI-pBAD/Thio interactions, compared to EctopoI-pBAD/Thio interactions suggest that enzyme turnover during plasmid DNA relaxation is enhanced due to the presence of Mg^{2+}.

4.6: References

1. P.B. Tiwari, T. Annamalai, B. Cheng, G. Narula, X. Wang, Y.-C. Tse-Dinh, J. He, Y. Darici, Biochem. Biophys. Res. Commun. 2014, 445, 445.

2. Y.-C. Tse-Dinh, Nucleic Acids Res. 2009, 37, 731.

3. B. Cheng, S. Shukla, S. Vasunilashorn, S. Mukhopadhyay, Y.-C. Tse-Dinh, J. Biol. Chem. 2005, 280, 38489.

4. J.J. Champoux, Annu. Rev. Biochem. 2001, 70, 369.

5. J.C. Wang, Nat. Rev. Mol. Cell Biol. 2002, 3, 430.

6. K.D. Corbett, J.M. Berger, Annu. Rev. of Biophys. Biomol. Struct. 2004, 33, 95.

7. L.F. Liu, J.C. Wang, Proc. Nat. Acad. Sci. 1987, 84, 7024.

8. H.-Y. Wu, S. Shyy, J.C. Wang, L.F. Liu, Cell 1988, 53, 433.

9. H.-P. Tsai, L.-W. Lin, Z.-Y. Lai, J.-Y. Wu, C.-E. Chen, J. Hwang, C.-S. Chen, C.-M. Lin, J. Biomed. Sci. 2010, 17, 49.

10. J.C. Wang, Annu. Rev. Biochem. 1985, 54, 665.

11. C. Sissi, M. Palumbo, Nucleic Acids Res. 2009, 37, 702.

12. K. Drlica, Trends Genet. 1990, 6, 433.

13. R.M. Lynn, J.C. Wang, Proteins: Struct., Funct., Genet. 1989, 6, 231.

14. W.D. Wilson, Science 2002, 295, 2103.

15. C.D. Pond, J.A. Holden, P.C. Schnabel, L.R. Barrows, Anti-Cancer Drugs 1997, 8, 336.

16. T. Bhaduri, T.K. Bagui, D. Sikder, V. Nagaraja, J. Biol. Chem. 1998, 273, 13925.

17. A.E.M. Wammes, M.J.E. Fischer, N.J. de Mol, M.B. van Eldijk, F.P.J.T. Rutjes, J.C.M. van Hest, F.L. van Delft, Lab Chip 2013, 13, 1863.

18. C.J. Thomas, V. Anbazhagan, M. Ramakrishnan, N. Sultan, I. Surolia, M.J. Swamy, Biophys. J. 2003, 84, 3037.

19. Y.P. Shan, P.B. Tiwari, P. Krishnakumar, I. Vlassiouk, W.Z. Li, X.W. Wang, Y. Darici, S.M. Lindsay, H.D. Wang, S. Smirnov, J. He, Nanotechnology 2013, 24, 495102.

20. L. Nieba, S.E. Nieba-Axmann, A. Persson, M. Hämäläinen, F. Edebratt, A. Hansson, J. Lidholm, K. Magnusson, Å.F. Karlsson, A. Plückthun, Anal. Biochem. 1997, 252, 217.

21. M.A. Wear, A. Patterson, K. Malone, C. Dunsmore, N.J. Turner, M.D. Walkinshaw, Anal. Biochem. 2005, 345, 214.

22. Silicon Kinetics Website, Application note: 13, http://www.siliconkinetics.com/pdf/SKi_Assay_Designs_for_Immobilization_AN13 .pdf [November 2014], 2014.

23. S.-J. Chen, J.C. Wang, J. Biol. Chem. 1998, 273, 6050.

24. Y.-C. Tse-Dinh, R.K. Beran-Steed, J. Biol. Chem. 1998, 263, 15857.

25. A. Ahumada, Y.-C. Tse-Dinh, BMC Biochem. 2002, 3, 13.

26. A. Ahumada, Y.-C. Tse-Dinh, Biochem. Biophys. Res. Commun. 1998, 251, 509.

27. L. Yu, C.-X. Zhu, Y.-C. Tse-Dinh, S.W. Fesik, Biochemistry 1995, 34, 7622.

28. W. Ahmed, A.G. Bhat, M.N. Leelaram, S. Menon, V. Nagaraja, Nucleic Acids Res. 2013, 41, 7462.

29. T. Bhaduri, D. Sikder, V. Nagaraja, Nucleic Acids Res. 1998, 26, 1668.

30. C.D. Lima, J.C. Wang, A. Mondragon, Nature 1994, 367, 138.

31. D. Strahs, C.-X. Zhu, B. Cheng, J. Chen, Y.-C. Tse-Dinh, Nucleic Acids Res. 2006, 34, 1785.

32. H. Feinberg, C.D. Lima, A. Mondragón, Nat. Struct. Biol. 1999, 6, 918.

33. C.-X. Zhu, Y.-C. Tse-Dinh, J. Biol. Chem. 2000, 275, 5318.

CHAPTER 5: ANALYZING SURFACE PLASMON RESONANCE DATA: CHOOSING A CORRECT BIPHASIC MODEL FOR INTERPRETATION

In Chapters 3 and 4, I explained SPR as a label free experimental tool for the analysis of biomolecular interactions. This chapter presents my theoretical research results for the analysis of the biphasic SPR data. The determination of the association rate constant (k_a) and dissociation rate constant (k_d) requires the fitting of SPR sensorgrams. For the SPR data fitting using a single exponential function, the procedure to extract the rate constants is straightforward. However, there is no simple procedure for SPR data fitting with double exponential functions. The commonly existing procedure requires some prior knowledge of the underlying interaction mechanism and the extracted rate constants often have large uncertainties. In this chapter, a new method of analyzing the biphasic SPR data is presented using the three commonly employed biphasic models. This method is based on a general analytical solution of the biphasic rate equations, which is much more transparent and straightforward than the highly non-linear numerical integration approach. The procedures have been illustrated with examples of the data analysis on simulated SPR profiles, and the results are discussed. The contents of this chapter has been adapted from my research results published in a peer reviewed paper [1].

5.1: Introduction

Surface plasmon resonance (SPR) is an affinity based label-free biophysical technique for the analysis of biomolecular interactions, including the determination of the kinetic parameters [2-9]. SPR has been successfully used to study protein-protein and protein-DNA interactions [10-14], peptide inhibitor studies [15], adsorption rate of

chemical molecules [16], and to investigate the binding of proteins to lipid membranes [17]. SPR has also been used as a fundamental tool to validate the quantitative data from other method [18]. The equilibrium SPR data analysis method has been used successfully to determine the equilibrium dissociation constant (K_d) [11]. However, this simple method has some limitations [19]. Therefore, the kinetic analysis should be performed in order to obtain the association rate constant (k_a) and dissociation rate constant (k_d) [20].

Several attempts have been reported in order to enhance the resolution of SPR systems [21-23]. However, there is no clear and straightforward procedure to choose and analyze the appropriate biphasic SPR data. A commonly used approach is to fit the SPR data directly with the numerical solutions of the rate equations, corresponding to a chosen biphasic model [24-29], and the procedure relies on the quality of fitting (R^2 value) to numerical solutions of the rate equations as well as on some prior knowledge of the system under study to determine the underlying biphasic binding mechanisms. In addition, this highly non-linear fitting procedure assumes that the two components (phases) of the biphasic reaction contribute equally to the SPR signal, which may not be true for real systems. The three commonly used biphasic binding models: two-step conformational change model (Model 1) [24,25], heterogeneous ligand model (Model 2) [26,27,30], and bivalent ligand model (Model 3) [28,29], have been explained in this Chapter.

This chapter attempts to address these issues based on analytical solutions of linear rate equations, which include the three widely used biphasic models, mentioned above. Systems with non-linear rate equations and systems beyond biphasic reactions are not considered here. This approach avoids the ambiguity of the relative SPR signal

weight for each phase of the biphasic reactions, and gives a well-defined procedure to identify the specific biphasic models. Moreover, this approach leads to a straightforward procedure to extract the rate constants from the fitting of the SPR profiles. These procedures of SPR data fitting, model identification and extraction of the rate constants are illustrated by the analysis of simulated SPR profiles.

5.2: Theoretical methods

5.2.1: Data analysis for the biphasic binding model

The three different biphasic models, as explained in detail in Section 1.3, can be expressed in matrix form as:

$$X' = A_0 + A_{12}X \tag{5.1}$$

where, $X' = \begin{pmatrix} X_1' \\ X_2' \end{pmatrix}, A_0 = \begin{pmatrix} a_0 \\ b_0 \end{pmatrix}, A_{12} = \begin{pmatrix} a_1 & a_2 \\ b_1 & b_2 \end{pmatrix},$ and $X = \begin{pmatrix} X_1 \\ X_2 \end{pmatrix}$. X_1 and X_2

represent the two phases of the biphaisc reaction. The matrix elements, listed in Table 5.1, are obtained by comparing Equations 1.6, 1.8 and 1.10 with Equation 5.2 as given below:

$$\frac{dX_1}{dt} = X_1' = a_0 + a_1X_1 + a_2X_2$$

$$\frac{dX_2}{dt} = X_2' = b_0 + b_1X_1 + b_2X_2 \tag{5.2}$$

where, a_0, a_1, a_2, b_0, b_1, and b_2 all are constants.

Model	a_0	a_1	a_2	b_0	b_1	b_2
1	$k_{a1}C[B_0]$	$-(k_{a1}C + k_{d1} + k_2)$	$-(k_{a1}C - k_{-2})$	0	k_2	$-k_{-2}$
2	$k_{a1}C[B_0]$	$-(k_{a1}C + k_{d1})$	0	$k_{a2}C[B_0']$	0	$-(k_{a2}C + k_{d2})$
3	$2k_{a1}C[B_0]$	$-(k_{a1}C + k_{a2}C + k_{d1})$	$-(2k_{a1}C - k_{d2})$	0	$k_{a2}C$	$-k_{d2}$

Table 5.1: The matrix elements of matrices A_0 and A_{12}.

As long as A_0 and A_{12} are independent of time, Equation 5.1 can be solved analytically, in the following form:

$$X_1 = P_o + P_1 e^{-\sigma_1 t} + P_2 e^{-\sigma_2 t}$$

$$X_2 = Q_o + Q_1 e^{-\sigma_1 t} + Q_2 e^{-\sigma_2 t}$$

(5.3)

where, P's and Q's depend on A_0 and A_{12}. With initial conditions of $X_1 = X_2 = 0$ at $t = 0$, P_o equals $-(P_1 + P_2)$ and Q_o equals $-(Q_1 + Q_2)$. It is well known that for linear differential equations, the exponents (σ_1 and σ_2) only depend on the elements of the matrix A_{12} and in fact are the eigenvalues of matrix A_{12}:

$$\sigma_1 = -\frac{1}{2}(a_1 + b_2) + \frac{1}{2}\sqrt{(a_1 - b_2)^2 + 4a_2 b_1}$$

$$\sigma_2 = -\frac{1}{2}(a_1 + b_2) - \frac{1}{2}\sqrt{(a_1 - b_2)^2 + 4a_2 b_1}$$

(5.4)

The eigenvalues (σ_1 and σ_2), separately, have complicated dependency on the elements of A_{12}, but as roots of quadratic equations they satisfy simple relationships:

$$\sigma_1 + \sigma_2 = -(a_1 + b_2)$$

$$\sigma_1 \sigma_2 = a_1 b_2 - a_2 b_1$$

(5.5)

Similarly, the exponents γ_1 and γ_2 can be obtained from the SPR dissociation profiles. In fact, the γ's are the σ's at analyte concentration $C = 0$. The sums and products of the matrix eigenvalues derived from these matrix elements are listed in Table 5.2.

Model	$\sigma_1 + \sigma_2$	$\sigma_1 \sigma_2$	$\gamma_1 + \gamma_2$	$\gamma_1 \gamma_2$
1	$k_{a1}C + k_{d1} + k_2 + k_{-2}$	$k_{a1}(k_2 + k_{-2})C + k_{d1}k_{-2}$	$k_{d1} + k_2 + k_{-2}$	$k_{d1}k_{-2}$
2	$(k_{a1} + k_{a2})C + k_{d1} + k_{d2}$	$k_{a1}k_{a2}C^2 + (k_{a1}k_{d2} + k_{d1}k_{a2})C + k_{d1}k_{d2}$	$k_{d1} + k_{d2}$	$k_{d1}k_{d2}$
3	$(k_{a1} + k_{a2})C + k_{d1} + k_{d2}$	$2k_{a1}k_{a2}C^2 + k_{a1}k_{d2}C + k_{d1}k_{d2}$	$k_{d1} + k_{d2}$	$k_{d1}k_{d2}$

Table 5.2: The products and sums of the eigenvalues of matrix A_{12} (Equation 5.5). The γ's are the σ's at analyte concentration $C = 0$.

5.2.2: SPR data fitting using double exponential functions

In the biphasic reaction, each phase of the reaction contributes to the SPR response. Therefore, the SPR response (R) is, in general, a linear combination of the two variables:

$$R = \alpha X_1 + \beta X_2 \tag{5.6}$$

where, X_1 is $[AB^*], [AB], [A_1B]$, and X_2 is $[AB], [AB'], [A_2B]$ for Model 1, Model 2, Model 3, respectively. As shown in Equation 5.3, X_1 and X_2 have the same exponents, σ_1 and σ_2 (or γ_1 and γ_2 for dissociation). Hence, the SPR response R, regardless of the values of α and β, must still be a linear combination of two exponential functions. Partly due to complexity of Equation 5.4, the prevalent practice is to fit the SPR data directly to the numerical solutions of the rate equations. For this approach to work, it is necessary to assume $\frac{\alpha}{\beta} = 1$. Notably, the ratio $\frac{\alpha}{\beta}$ only affects the coefficients of the exponential functions, but does not affect the exponents. Therefore, a more sensible way, that we proposed here, is to fit the SPR profiles to double exponential functions.

The association profiles were fitted using the following Equation:

$$R = D + Ee^{-\sigma_1 t} + Fe^{-\sigma_2 t} \tag{5.7}$$

where, D, E, and F are all constants. With $D = -(E + F)$, there are four fitting parameters. The SPR dissociation profiles are fitted using the following Equation with two additional parameters, γ_1 and γ_2:

$$R = Ee^{-\gamma_1(t-t_o)} + Fe^{-\gamma_2(t-t_o)} \tag{5.8}$$

where t_o is the time at the start of the dissociation profiles, which was fixed during the fitting. From Equations 5.3, 5.6, and 5.7, one can easily see that if α to β ratio is known,

the ratio of $\frac{E}{F} = \frac{\frac{\alpha}{\beta}P_1 + Q_1}{\frac{\alpha}{\beta}P_2 + Q_2}$, which is determined by analytical solutions. However, since in

general α to β ratio is unknown, we let both E and F to be free fitting parameters.

5.2.3: Identification of the underlying biphasic mechanism

Based on Table 5.2, the dependencies of σ_1 and σ_2 as well as their sums and their

products on the analyte concentration C are summarized in Table 5.3, which is essential

for the identification of the correct biphasic model. Table 5.3 clearly shows that in order

to identify the underlying models, SPR experiments need to be carried out, at the

minimum, for three different analyte concentrations. In reality, experiments for more

values of analyte concentration may have to be carried out to truly reveal the quadratic or

other non-linear behaviors of the exponents. In the example shown in Section 5.3.1

below, five analyte concentration values were used in order to have a confident

identification of the underlying model.

Model	$\sigma_1 + \sigma_2$ vs. C	$\sigma_1\sigma_2$ vs. C	σ_1 and σ_2 vs. C
1	Linear	Linear	Non-linear
2	Linear	Quadratic	Linear
3	Linear	Quadratic	Non-linear

Table 5.3: The dependency of the eigenvalues (σ_1 and σ_2), and their sums and products (for association) on the analyte concentration (C).

As shown in Table 5.3, one should first examine the sum, $\sigma_1 + \sigma_2$, which should be

linear in C for all three models. This serves to verify that the underlying mechanism is

indeed a linear biphasic reaction. Then, one should examine the product $\sigma_1 \sigma_2$. If this is

linear in C, then the choice is the two-step conformational change model (Model 1). If the

product is quadratic in C, then one needs to examine the plots of σ_1 and σ_2 vs. C. If the

plots are linear, then the choice is the heterogeneous ligand model (Model 2); otherwise the choice is the bivalent ligand model (Model 3).

5.2.4: Determination of rate constants and their uncertainties

Once the appropriate model is determined and exponents are obtained from fitting procedures as described in Section 5.2.3 in order to determine the rate constants. Based on the exponents obtained from the fitting and the appropriate biphasic binding model, one can use the following procedures to extract the rate constants for the specific binding model.

In case of Model 1, the slope of $\sigma_1 + \sigma_2$ vs. C plot gives k_{a1}, the slope of $\frac{\sigma_1 \sigma_2}{k_{a1}}$ vs. C gives the sum $k_2 + k_{-2}$, $\gamma_1 + \gamma_2 - (k_2 + k_{-2})$ gives k_{d1}, $\frac{\gamma_1 \gamma_2}{k_{d1}}$ gives k_{-2}, and finally, $\gamma_1 + \gamma_2 - (k_{d1} + k_{-2})$ provides k_2. k_a and k_d pairs of the rate constants are very straightforward with these calculations. The two equilibriam association constants can be calculated as $K_{A1} = \frac{k_{a1}}{k_{d1}}$ (intermediate stage) and $K_{A2} = \frac{k_2}{k_{-2}}$ (final stage). The overall association constant is now calculated as $K_A = K_{A1}(1 + K_{A2})$ [25]. Finally, the K_d value is the inverse of K_A i.e. $K_d = \frac{1}{K_A}$.

In case of Model 2, γ_1 and γ_2 produce the two dissociation rate constants (k_{d1} and k_{d2}). Since there is no complicated dependancy of σ_1 and σ_2 on C for this particular biphasic model, the slopes of the linear fit of σ_1 vs. C and σ_2 vs. C directly give k_{a1} and k_{a2}, respectively. Comparing the intercepts from the fitting of σ vs. C plot with the γ values, one can easily identify which k_d is related to which k_a. The K_d's can now be calculated as $K_{d1} = \frac{k_{d1}}{k_{a1}}$ and $K_{d2} = \frac{k_{d2}}{k_{a2}}$.

In case of Model 3, γ_1 and γ_2 produce the two dissociation rate constants (k_{d1} and k_{d2}). The linear coefficient of the quadratic fit of $\sigma_1\sigma_2$ vs. C plot provides $k_{a1}k_{d2}$. Using $\gamma_2 = k_{d2}$, k_{a1} can be calculated. The quadratic coefficient of the quadratic fit of $\sigma_1\sigma_2$ vs. C plot provides $2k_{a1}k_{a2}$. Finally, using the value of k_{a1}, k_{a2} is calculated. It is not clear whether the exponents γ_1 and γ_2 are k_{d1} and k_{d2}, respectively. The values of the dissociation rate constants may be switched. Therefore, k_{d1} and k_{d2} should be carefully identified. If $k_{a1} + k_{a2}$ (using both k_{a1} and k_{a2} determined above) gives a comparable value as the slope of $\sigma_1 + \sigma_2$ vs. C plot, obtained from the fitting, then the k_{d2} used above is correct. Otherwise, γ_1, instead of γ_2, should be used for k_{d2} and γ_2 for k_{d1}. Finally, the K_d's can be calculated as $K_{d1} = \frac{k_{d1}}{k_{a1}}$ and $K_{d2} = \frac{k_{d2}}{k_{a2}}$.

As discussed in Section 5.2.3, although the exponents σ_1 and σ_2 may have strong non-linear dependencies on the analyte concentration (C), their sums and products (Equation 5.5) are at most quadratic in C (Table 5.3). This fact greatly simplifies the procedure for the determination of the rate constants. The uncertainties of the rate constants are mainly due to the two fitting procedures (Sections 5.2.2 and 5.2.3): one is the fitting of SPR profiles to double exponential functions, and the other is the fitting of the exponents (as well as their sums and products) to a linear or a quadratic function of the analyte concentration C. Because both fitting procedures are based on analytical solutions and are performed using exact functions, no systematic errors are introduced from the fitting procedures. The only source of uncertainty is the noise in the SPR profiles and variation in SPR experimental conditions, such as variation in qualities and sensitivities of the sensor chips.

Fitting of SPR profiles to double exponential functions is a non-linear one. Caution must be exercised in choosing the initial parameters. The quality of the fitting can be judged by the R^2 value as well as the standard error of the fitting. Typically, multiple SPR profiles (under the same experimental conditions, of course) are fitted, and average exponents and their standard deviations are obtained. The second fitting procedure (Section 5.2.4) is straightforward. The fitting parameters and their uncertainties can be obtained using standard error analysis techniques [31].

5.3: Results and discussion

5.3.1: Analysis of simulated SPR profiles
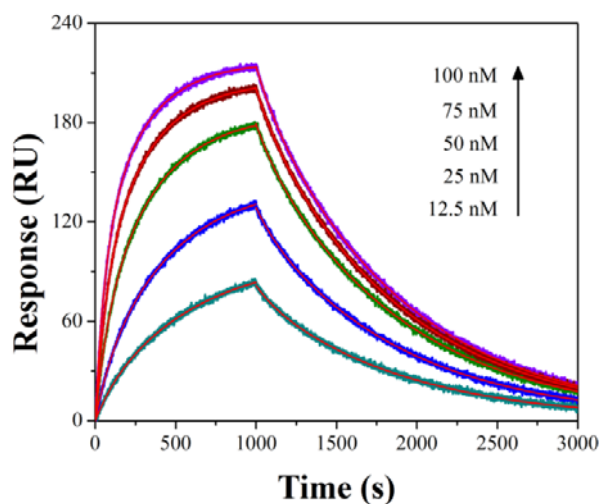
Figure 5.1: Simulated SPR profiles for the two-step conformational change model (Model 1). The zig-zag lines represent the simulated SPR profiles and the continuous lines (red) are the fit to equation 5.7 (association) and equation 5.8 (dissociation).

The Mathematica software was used to simulate SPR sensorgrams, and the Originpro 9.1 to fit the simulated SPR profiles and to perform error analysis. We generated the SPR sensorgrams by directly substituting the rate constants into the analytical solutions (with $B_o = 250$ RU) and adding a random noise with a standard deviation of 1 RU to simulate the experimental noises. Five SPR association profiles with

random noise were generated for each analyte concentration. The analyte concentration was set to zero during the simulation of the dissociation profiles. The dissociation profiles were simulated five times in total. The SPR association profiles, for the two-step conformational change model (Model 1), were simulated at five different analyte concentrations ($C = 12.5$ to 100 nM), using $\alpha = 0.8$ and $\beta = 1.2$. The rate constants were chosen to be the same as in a previous report ($k_{a1} = 1 \times 10^5$ M^{-1}s^{-1}, $k_{d1} = 5 \times 10^{-3}$ s^{-1}, $k_2 = 3 \times 10^{-3}$ s^{-1}, and $k_{-2} = 2 \times 10^{-3}$ s^{-1}) [32]. The simulated SPR profiles, together with the fitted lines of double exponential functions, are shown in Figure 5.1.

As shown in Figure 5.1, simulated SPR profiles were fitted well with double exponential functions. This is to be expected, as explained in Section 5.2. The fitted values of the exponents as well as their standard deviations are listed in Table 5.4.

C	σ_1 ($\times 10^{-3}$ s^{-1})		σ_2 ($\times 10^{-3}$ s^{-1})		γ_1 ($\times 10^{-3}$ s^{-1})		γ_2 ($\times 10^{-4}$ s^{-1})	
	Fitted	Analytical	Fitted	Analytical	Fitted	Analytical	Fitted	Analytical
12.5	9.44±0.95	9.55	1.69±0.05	1.70				
25	10.05±0.38	10.03	2.16±0.03	2.18	8.76±0.24	8.87	11.25±0.03	11.27
50	12.09±0.23	12.11	2.89±0.02	2.89				
75	14.12±0.19	14.14	3.35±0.02	3.36				
100	16.25±0.12	16.33	3.66±0.02	3.68				

Table 5.4: Fitted exponents, σ_1, σ_2 and γ_1, γ_2 for Model 1 (Figure 5.1) using two exponential functions.

Next, the concentration dependencies of the exponents (σ_1 and σ_2), and their sums and products was investigated. As can be seen from Figure 5.2, the sum ($\sigma_1 + \sigma_2$) and the product ($\sigma_1\sigma_2$) are linear in C (Figures 5.3(a) and 5.3(b)), σ_2 (Figure 5.2(d)) is obviously non-linear in C while the non-linearility of σ_1 is weak (Figure 5.2(c)). According to Table 5.3, the nonlinearity of σ_2 is enough to justify the choice of Model 1. Table 5.3 only gives theoretical behavior of the exponents σ_1 and σ_2 (and their sums and products) for different models. In reality, of course, any non-linear function may appear

to be linear within a small range of the independent variable. A quadratic function may have a very small quadratic coefficient, and some non-linear function can have asymptotic linear behaviors. All these can present difficulties in using Table 5.3 to identify the correct biphasic models.
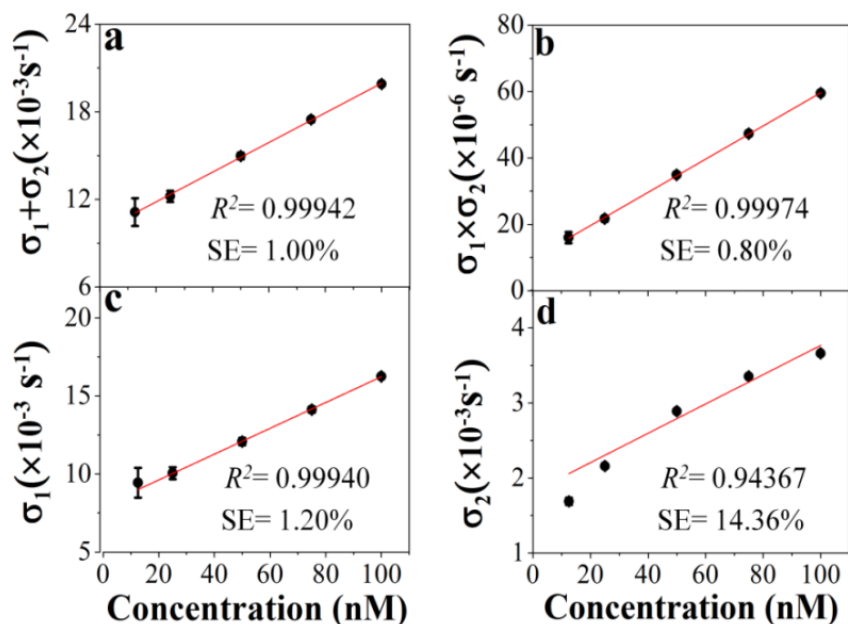
Figure 5.2: The plots of (a) the sum $\sigma_1 + \sigma_2$, (b) the product $\sigma_1\sigma_2$ vs. C, (c) σ_1, and (d) σ_2 vs. the analyte concentration C. The symbols are the average with error bars as the standard deviation and the continuous line represents a linear fit.

In cases where the model cannot be uniquely determined (for example, both the plots $\sigma_1\sigma_2$ vs. C, and σ_1 and σ_2 vs. C are weakly non-linear), one needs to change SPR experimental conditions and repeat the experiments, either change the range of analyte concentrations, or record SPR profiles for appropriate time duration, or do both. Actually, these difficulties are the benefit of the analytical solutions. Because our method identifies the behavior of the exponents of various models, it can help experimentalists to design SPR experiments under appropriate experimental conditions to reveal the true behavior of the exponents.

Another possibility is when the two phases of the biphasic reaction proceed with fairly different time scale. As a result, σ_1 and σ_2 may have different asymptotic behavior and they may not show non-linear behavior within the same range of the analyte concentrations. This is indeed the case for our example reported here as shown in Figure 5.2, where σ_1 is very weakly non-linear. However, σ_2 is clearly non-linear and this is enough evidence to identify the correct model (Model 1). According to Table 5.3, this nonlinearity of σ_2 is enough to justify the choice of Model 1. Also shown in Figure 5.2, the uncertainty of σ_1 is somewhat bigger for the lowest analyte concentration (12.5 nM). This is because we have set the same absolute noise level for simulated SPR sensorgrams at every concentration.

After having decided the appropriate model, we followed the procedures as outlined in the Section 5.2.4 to determine the rate constants. The results are listed in Table 5.5. The obtained rate constants are in good agreement with the corresponding input rate constants (Table 5.5). As can be seen from Figure 5.2, the linear fit in Figure 5.2(a) and Figure 5.2(b) is very good (relative standard error of fitting $\leq$ 1%). Hence the uncertainties in the rate constants are mainly due to the standard deviations of the exponents (Table 5.4).

Parameters	k_{a1} ($\times 10^5$ M^{-1}s^{-1})	k_{d1} ($\times 10^{-3}$ s^{-1})	k_2 ($\times 10^{-3}$ s^{-1})	k_{-2} ($\times 10^{-3}$ s^{-1})
Input	1.00	5.00	3.00	2.00
Output	1.00±0.01	4.88±0.25	2.99±0.37	2.02±0.12

Table 5.5: The input and output values for the parameters k_{a1}, k_{d1}, k_2 and k_{-2} for Model 1.

The uncertainties of the rate constants in Table 5.5 are evaluated using standard error analysis techniques. The uncertainties are in good agreement with a previous study based on numerical integration approach [32], considering that our random noise of 1.0

RU was about twice as large, and a much smaller number of SPR profiles (five) were simulated for each analyte concentration. We believe that using a smaller number of SPR profiles for each analyte concentration is more realistic and feasible for actual SPR experiments.

5.3.2: Effect of $\frac{\alpha}{\beta} = 1$ assumption on the exponents
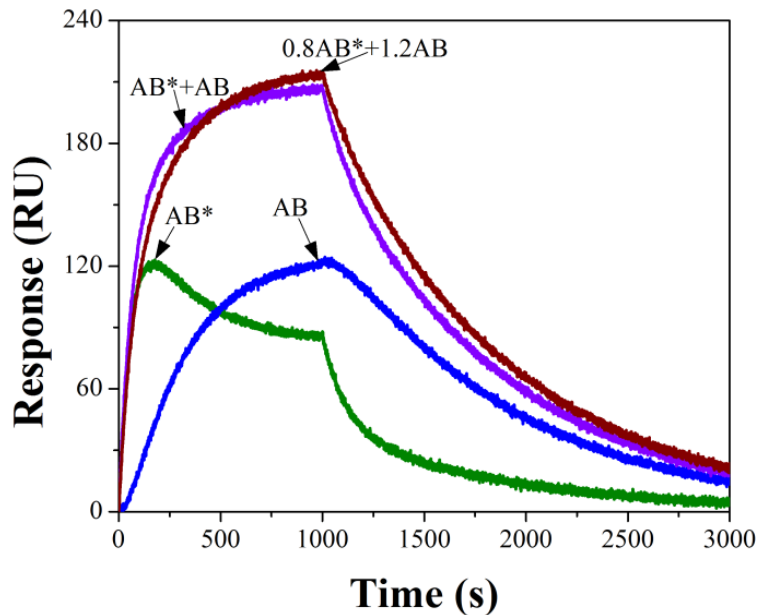
Figure 5.3: Simulated SPR data for the two-step conformational change model at a random noise level of 1 RU. The analyte concentration was 100 nM and this value was set to zero in order to simulate the dissociation profiles.

Although the prevailing practice assumes $\frac{\alpha}{\beta} = 1$ (Equation 5.6), this may not be true in real systems. Figure 5.3 shows the simulated SPR sensorgrams for the two-step conformational change model (Model 1), for analyte concentration of 100 nM, and with the same kinetic parameters as used in the Section 5.3.1. The SPR profiles, association and dissociation, are quite different between the choices of $\alpha = \beta = 1$, and $\alpha = 0.8$ and $\beta = 1.2$.
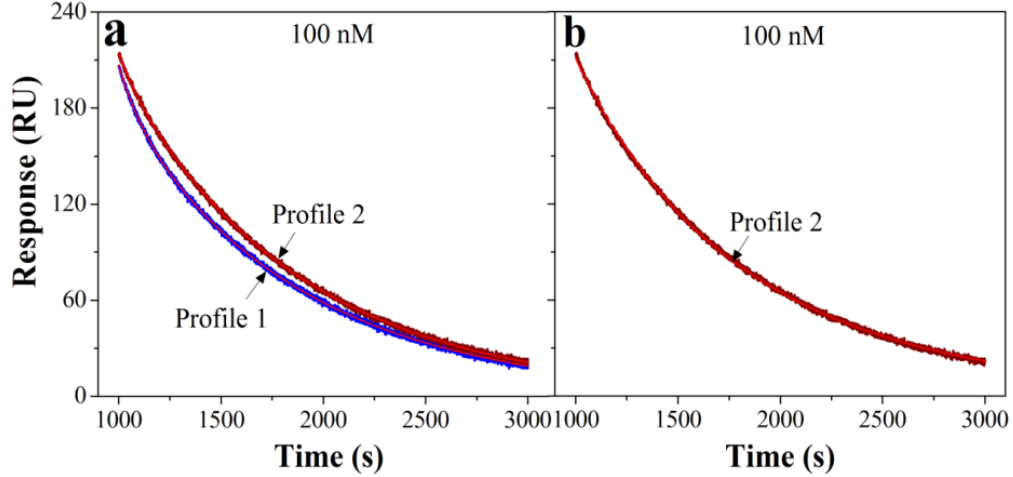
Figure 5.4: (a) Simulated SPR dissociation profiles (from Figure 5.1) assuming $\alpha = \beta = 1$ (Profile 1), and $\alpha = 0.8$ and $\beta = 1.2$ (Profile 2), and (b) SPR dissociation profile (Profile 2) fitted with the two exponential functions while enforcing $\frac{\alpha}{\beta} = 1$. The zig-zag lines represent the simulated SPR dissociation profiles and the continuous lines (red lines) are the fit.

In order to investigate further the effect of the $\frac{\alpha}{\beta} = 1$ assumption, we fitted the SPR dissociation profiles from Figure 5.3. The results are shown in Figure 5.4. In Figure 5.4(a), two SPR dissociation profiles (zig-zag lines) for $\frac{\alpha}{\beta} = 1$ (Profile 1), and $\frac{\alpha}{\beta} = \frac{2}{3}$ (Profile 2), were fitted (continuous lines) with two exponential functions. In Figure 5.4(b), Profile 2 ($\frac{\alpha}{\beta} = \frac{2}{3}$) was fitted again with two exponential functions while enforcing $\frac{\alpha}{\beta} = 1$; i.e., we kept the ratio of the parameters E and F (Equation 5.8) to be the same as what was obtained from the fitting of Profile 1 (Figure 5.4(a)). The corresponding fitted exponents are listed in Table 5.6. The errors in Table 5.6 are the standard error of fitting.

Figure	γ_1 (s^{-1})	γ_2 (s^{-1})	R^2
4a, Profile 1	$(8.73\pm0.12)\times10^{-3}$	$(11.26\pm0.01)\times10^{-4}$	0.9996
4a, Profile 2	$(9.02\pm0.25)\times10^{-3}$	$(11.26\pm0.01)\times10^{-4}$	0.9996
4b, Profile 2	$(2.81\pm0.03)\times10^{-3}$	$(10.70\pm0.01)\times10^{-4}$	0.9995
Analytical	8.87×10^{-3}	11.27×10^{-4}	-

Table 5.6: Fitted parameters for the SPR dissociation profiles as shown in Figure 5.4 using two exponential functions. The analytical calculations of the parameters are also given for comparison.

The fitting of Profile 2 in Figure 5.4(b) was very good with R^2 value of 0.9995, similar to the fitting qualities in Figure 5.4(a). However, the exponent γ_1 is nearly three times the analytical value (Table 5.6). In other words, the R^2 value gave no indication of the serious error in the assumption of $\frac{\alpha}{\beta} = 1$, as opposed to the real value of $\frac{\alpha}{\beta} = \frac{2}{3}$. Our method, on the other hand, recovered the correct exponents for both profiles (Table 5.6). Notably, the assumption of $\frac{\alpha}{\beta} = 1$ introduces a systematic error. The data fittings using simulated SPR profiles with relatively smaller noises were unable to recover the correct values of the exponents.

5.3.3: Reliability of model identification based on the new approach
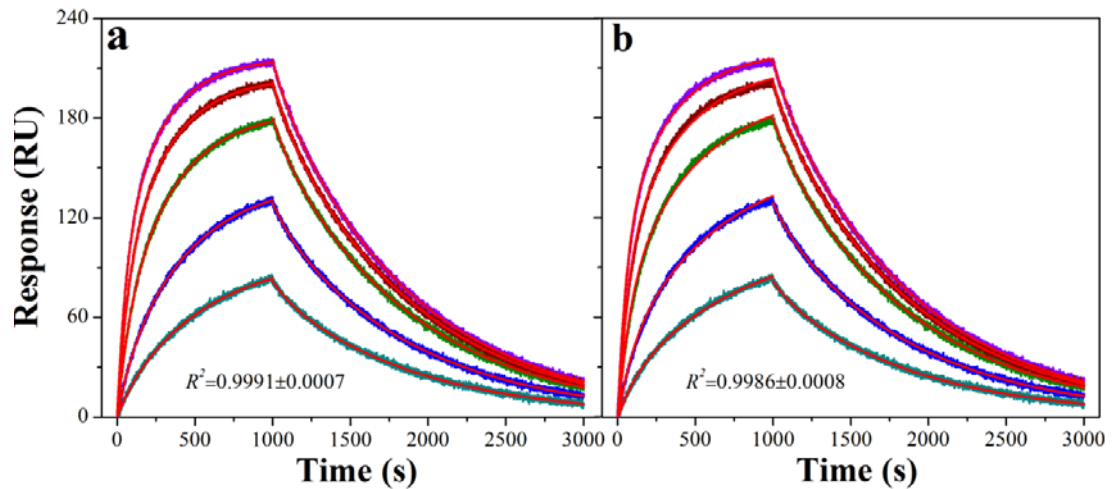
Figure 5.5: Simulated SPR association profiles (zig-zag lines) fitted to with Equation 5.7 (association) and Equation 5.8 (dissociation) with fixed exponents (continuous lines): (a) the exponents were calculated using the rate constants for Model 1, and (b) the exponents were calculated using the rate constants for Model 2.

As shown in Section 5.2, every linear biphasic model results in double exponential SPR profiles. Therefore, a given SPR profile can be fitted equally well to different biphasic models. In order to demonstrate this, we used the simulated SPR profiles (from Figure 5.1) and fitted to Equation 5.7 (association) and Equation 5.8

80

(dissociation) using different biphasic models and different rate constants. The results in Figure 5.5 indicate that a given SPR profile can be fitted equally well to different biphasic models.

In Figure 5.5(a), the SPR profiles are compared to the "correct" model (Model 1) using the rate constants listed in Table 5.5. As expected, the agreement is very good with $R^2 \sim 0.9991$. In Figure 5.5(b), the same SPR profiles are compared to a purposefully picked "wrong" model (Model 2). Surprisingly, a similarly good fitting to SPR profiles was achieved ($R^2 \sim 0.9986$). The rate constants for the "wrong" model were obtained using procedures outlined in Section 5.2.4. The rate constants for the "wrong" model are: $k_{a1} = (0.83 \pm 0.01) \times 10^5$ $M^{-1}s^{-1}$, $k_{d1} = (8.76 \pm 0.24) \times 10^{-3}$ s^{-1}, $k_{a2} = (1.95 \pm 0.28) \times 10^4$ s^{-1}, and $k_{d2} = (11.25 \pm 0.03) \times 10^{-4}$ s^{-1}. The relative uncertainty of k_{a1} for the "wrong" model is somewhat bigger than that of the "correct" model (Table 5.5). This is because the "wrong" model has introduced systematic error in the fitting. In particular, σ_1 and σ_2 are non-linear, but the "wrong" model requires them to be linear (Table 5.3).

Therefore, in order to identify the underlying biphasic reaction, one must investigate the behavior of the exponents as a function of the analyte concentration C (Table 5.3). Neither the slightly bigger uncertainty of the rate constants nor the minimal decrease of R^2 value enables one to confidently reject the "wrong" model. We fully expect that for SPR profiles of a high quality (such as relatively smaller noises, wide range as well as large numbers of the analyte concentration values, etc.), R^2 value for the "wrong" model could be significantly worse than that of the "correct" model. Additionally, prior knowledge and experience with the system under study can help to

identify the "correct" model and reject the "wrong" one. Even in such cases, the approach explained here can still be of great value in confirming the model identification using the existing approach.

5.4: Conclusions

I have presented a new approach for the analysis of SPR profiles. The method is based on analytical solutions of the linear biphasic rate equations, which is fundamentally different from the existing data fitting approach based on numerical solutions. This not only provided a firm theoretical foundation for our fitting procedures, but also lended theoretical support for some of the common practices in SPR measurements, such as performing SPR experiments at several different analyte concentrations, or fitting SPR profiles using double exponential functions.

In summary, the new SPR data analysis procedure, as explained in this report, has the following advantages: 1) avoids the ambiguity about which component (phase) of the biphasic mechanism is more sensitive to SPR, 2) obtains clear signature to determine the underlying biphasic reaction models, 3) does not require prior knowledge of a particular reaction model to determine the rate constants, and 4) uncertainty on the parameters can be transparently and directly assessed.

5.5: References

1. P.B. Tiwari, X. Wang, J. He, Y. Darici, Rev. Sci. Instrum. 2014, 86, 035001.

2. W.D. Wilson, Science 2002, 295, 2103.

3. D.G. Myszka, Curr. Opin. Biotechnol. 1997, 8, 50.

4. H. Nakajima, N. Kiyokawa, Y.U. Katagiri, T. Taguchi, T. Suzuki, T. Sekino, K. Mimori, T. Ebata, M. Saito, H. Nakao, T. Takeda, J. Fujimoto, J. Biol. Chem. 2001, 276, 42915.

5. B. Nguyen, F.A. Tanious, W.D. Wilson, Methods 2007, 42, 150.

6. S.C. Schuster, R.V. Swanson, L.A. Alex, R.B. Bourret, M.I. Simon, Nature 1993, 365, 343.

7. N.-F. Chiu, T.-Y. Huang, Sens. Actuators, B 2014, 197, 35.

8. B. Sikarwar, P.K. Sharma, A. Srivastava, G.S. Agarwal, M. Boopathi, B. Singh, Y.K. Jaiswal, Biosens. Bioelectron. 2014, 60, 201.

9. P.Y. Tsoi, M. Yang, Biosens. Bioelectron. 2004, 19, 1209.

10. J. Majka, C. Speck, In: Analytics of Protein–DNA Interactions, H. Seitz (Ed.), Springer Berlin Heidelberg, 2007, 13.

11. P.B. Tiwari, T. Annamalai, B. Cheng, G. Narula, X. Wang, Y.-C. Tse-Dinh, J. He, Y. Darici, Biochem. Biophys. Res. Commun. 2014, 445, 445.

12. E.M. Phizicky, S. Fields, Microbiol. Rev. 1995, 59, 94.

13. T. Berggård, S. Linse, P. James, Proteomics 2007, 7, 2833.

14. W. Wang, Y. Yang, S. Wang, V.J. Nagaraj, Q. Liu, J. Wu, N. Tao, Nat. Chem. 2012, 4, 846.

15. R.K. Somvanshi, A. Kumar, S. Kant, D. Gupta, S.B. Singh, U. Das, A. Srinivasan, T.P. Singh, S. Dey, Biochem. Biophys. Res. Commun. 2007, 361, 37.

16. N.M. Mulchan, M. Rodriguez, K. O'Shea, Y. Darici, Sensor. Actuators, B 2003, 88, 132.

17. P. Critchley, J. Kazlauskaite, R. Eason, T.J.T. Pinheiro, Biochem. Biophys. Res. Commun. 2004, 313, 559.

18. P.B. Tiwari, L. Astudillo, J. Miksovska, X. Wang, W. Li, Y. Darici, J. He, Nanoscale 2014, 6, 10255.

19. P.A. Van der Merwe, In: Protein–Ligand Interactions: Hydrodynamics and Calorimetry, S. Harding, B.Z. Chowdhry (Eds.), Oxford University Press, Oxford, UK, 2001, 137.

20. C. Hahnefeld, S. Drewianka, F. Herberg, In: Molecular Diagnosis of Infectious Diseases, J. Decler, U. Reischl (Eds.), Humana Press, New Jersey, 2004, 299.

21. S. Filion-Côté, P.J.R. Roche, A.M. Foudeh, M. Tabrizian, A.G. Kirk, Rev. Sci. Instrum. 2014, 85, 093107.

22. H.Q. Zhang, S. Boussaad, N.J. Tao, Rev. Sci. Instrum. 2003, 74, 150.

23. N.J. Tao, S. Boussaad, W.L. Huang, R.A. Arechabaleta, J. D'Agnese, Rev. Sci. Instrum. 1999, 70, 4656.

24. S. Lund-Katz, D. Nguyen, P. Dhanasekaran, M. Kono, M. Nickel, H. Saito, M.C. Phillips, J. Lipid Res. 2010, 51, 606.

25. D. Riesner, A. Pingoud, D. Boehme, F. Peters, G. Maass, Eur. J. Biochem. 1976, 68, 71.

26. J. Bernet, J. Mullick, Y. Panse, P.B. Parab, A. Sahu, J. Virol. 2004, 78, 9446.

27. W.L. Martin, P.J. Bjorkman, Biochemistry 1999, 38, 12639.

28. R.L. Rich, D.G. Myszka, J. Mol. Recognit. 2006, 19, 478.

29. F. Gesellchen, B. Zimmermann, F. Herberg, In: Protein-Ligand Interactions, G. Ulrich Nienhaus (Ed.), Humana Press, New Jersey, 2005, 17.

30. D. Wawrzak, M. Métioui, E. Willems, M. Hendrickx, E.d. Genst, L. Leyns, Biochem. and Biophys. Res. Commun. 2007, 357, 1119.

31. Originlab Website, http://www.originlab.com/pdfs/16_CurveFitting.pdf [September 2014], 2014.

32. T.A. Morton, D.G. Myszka, I.M. Chaiken, Anal. Biochem. 1995, 227, 176.

CHAPTER 6: QUANTITATIVE STUDY OF PROTEIN-PROTEIN

INTERACTION by QUARTZ NANOPIPETTES

In addition to SPR as discussed in Chapters 3, 4, and 5, this chapter presents a new label free nanopore based analytical method to quantitatively study protein-protein interaction. Unlike SPR, this method utilizes chemically modified nanopipettes (conical nanopores) with attoliter sensing volumes, to detect protein-protein interaction in a nano-confinement environment. With the proper modification of negatively charged human neuroglobin (hNgb) onto the inner surface of nanopipettes, I was able to detect concentration dependent current change when the hNgb modified nanopipette tip was exposed to positively charged cytochrome c (Cyt c) with a series of concentrations in the bath solution. The equilibrium dissociation constant (K_d) for the Cyt c-hNgb complex formations was derived and the value matched very well with the result from surface plasmon resonance (SPR) measurement. These results demonstrate that nanopipettes can potentially be used as a label-free analytical method to quantitatively characterize protein-protein interactions. The entire content in this chapter has been adapted from my research results published in a peer reviewed paper [1].

6.1: Introduction

Artificial nanopores, either biological or solid state, have become a new class of label-free electronic sensor since the pioneering work was reported in 1996 [2]. The current nanopore research focuses primarily on nucleic acids analysis, motivated by the promising progress in nanopore based single molecule DNA sequencing technique [3,4]. With the rapid progress of nanopore based technology, various types of nanopore devices have also been utilized to study other analytes, such as proteins [5-10], various

nanoparticles [11-13], and virus or virus-like particles [14]. In recent years, nanopore devices have been increasingly investigated for single protein detection and analysis. The size, charge, shape [9], unfolding [15], binding [16], surface adsorption [17], and aggregation [18] of proteins or protein complexes have been investigated at the single molecule level using nanopore devices. Metal ion-protein [19] and nucleic acid-protein [20] interactions have been quantitatively studied near the physiological conditions. Most recently, nanopore devices also show promising potential to be used to study kinetic protein-protein interactions quantitatively [21].

Protein-protein interactions play critical roles in the cellular processes. Quantitative study of protein-protein interactions is important for the fundamental understanding of their roles in cellular functions and for applications in disease diagnostics, ligand screening, and biomarker discovery. Therefore, it is necessary to carry out further investigations to apply nanopore devices on this important topic. Quartz or glass nanopipette made from micro-capillary tubes [22] can be viewed as a conical-shaped solid state nanopore. Nanopipettes with 10s of nanometer in inner diameter can be easily, cheaply and reproducibly fabricated, which is the most attractive feature of nanopipettes. Nanopipettes can detect and analyze analytes using two methods. The first one is the widely used resistive-pulse sensing method (or the Coulter counting method) for nanopore devices. The molecules pass through a nanopore, partially block the ionic pathways, and thereby cause detectable and stochastic changes in ionic current. Using this method, DNA [23-26] and proteins [7] have been detected and analyzed at the single molecule level. The second method is based on surface charge sensing. Due to its conical shape, the ionic current through the nanopipette is very sensitive to surface charge

variation near the nanopipette tip. The specific binding of a small number (tens or hundreds) of charged analytes to chemically modified pipette surface near the pore mouth often induces measurable change in the ionic current. In addition, the rectification ratio of the strongly rectified ionic current-voltage (I-V) curve is another useful signal that can be utilized [19,27]. Using this method, the bindings between metal ions and prion proteins [19,28,29] have been studied.

Herein, the idea of using nanopipettes was explored to quantitatively study protein-protein interactions, based on surface charge sensing. I used the cytochrome c (Cyt c) and human neuroglobin (hNgb) binding pair as the model system. These proteins and their intermolecular interactions are very important for a variety of biological activities, including preventive action during hypoxic conditions and apoptosis [30,31]. The receptor His-tagged hNgb proteins were immobilized onto the quartz nanopipette inner surface through anti-His antibodies. The negatively charged hNgb can specifically capture positively charged Cyt c in bath solution at neutral pH and induce measurable ionic current change through the nanopipette. The binding pairs can also be separated by treating them with 1 M NaCl solution, and the baseline ionic current can be recovered. By monitoring and analyzing the normalized ionic current change as a function of Cyt c concentration in the bath solution, an equilibrium dissociation constant (K_d) value of 20 ± 4 µM was obtained and was in good agreement with surface plasmon resonance (SPR) measurement, a well-established surface-based affinity senor. In the control experiments, the normalized ionic current change through the hNgb-modified nanopipette was monitored when the same concentration of positively charged Lysozyme (Lsz) proteins were added in the bath solution. Smaller current changes, with weak analyte

concentration dependence, were observed. This is consistent with the fact that the interaction between Lsz and hNgb is non-specific and weak. Analytical calculations and Poisson-Nernst-Planck (PNP) numerical simulations (numerical simulations are explained in Chapter 7) were carried out to understand the mechanism of the surface charge sensing method of nanopipettes for affinity analysis. My results suggest that glass/quartz nanopipettes have the potential to quantitatively study various protein-protein interactions. The protein immobilization method is general and can be applied to other His-tagged proteins. In these experiments, the effective sensing volume of nanopipette is several attoliters and the involved protein molecule number can be as few as 10s. Therefore, nanopipettes can also mimic the protein-protein interactions in a concentrated and crowded intracellular environment.

6.2: Methods

6.2.1: Reagents and solutions

(3-Aminopropyl) triethoxysilane (APTES) was purchased from Thermo Scientific (Rockford, IL); mouse anti-His antibody was purchased from Invitrogen (Camarillo, CA); Glutaraldehyde was purchased from SPI-CHEM (West Chester, PA), and 2-Aminoethanethiol hydrochloride from Acros Organics (Thermo Fisher Scientific, New Jersey, USA). Lysozyme from chicken egg white was purchased from Sigma Aldrich (St. Louis, MO). Ferric cytochrome c from equine heart (Cyt c) and ferric His-tagged human Ngb (hNgb) were received from Dr. Miksovska's lab at FIU. All other chemicals were purchased from Sigma Aldrich and used without further purification. All solutions were prepared using deionized (DI) water ($\sim$18MΩ) from a water purification system (Ultra Purelab system, ELGA/Siemens). If not mentioned otherwise, I always used buffered

KCl solution (25 mM KCl and 2.5 mM PB) at pH = 7.0 for ionic current measurements. The prepared electrolyte solution was filtered through a 0.2 µm filter and degassed by sonication. The conductivity of such an electrolyte solution was 0.367 Sm^{-1} at 23 ^{o}C, which was determined by a conductivity meter (Oakton, CON 510).

6.2.2: Quartz nanopipette fabrication and characterization

The fabrication and characterization of nanopipettes are explained in Section 2.2. The SEM result reveals that the inner diameter of nanopipettes is about 37 nm (Figure 2.2b). Although the inner diameter can be determined by SEM, it is not practical to check the inner diameter of every nanopipette by SEM. I, therefore, obtained the inner diameter of the nanopipettes based on the pore ionic conductance G_p using Equation 2.3. The estimated the average half cone angle of the outer surface is 1.9^{o}. Therefore, the estimation for the half cone angle, θ=1.6^{o}, is reasonable.
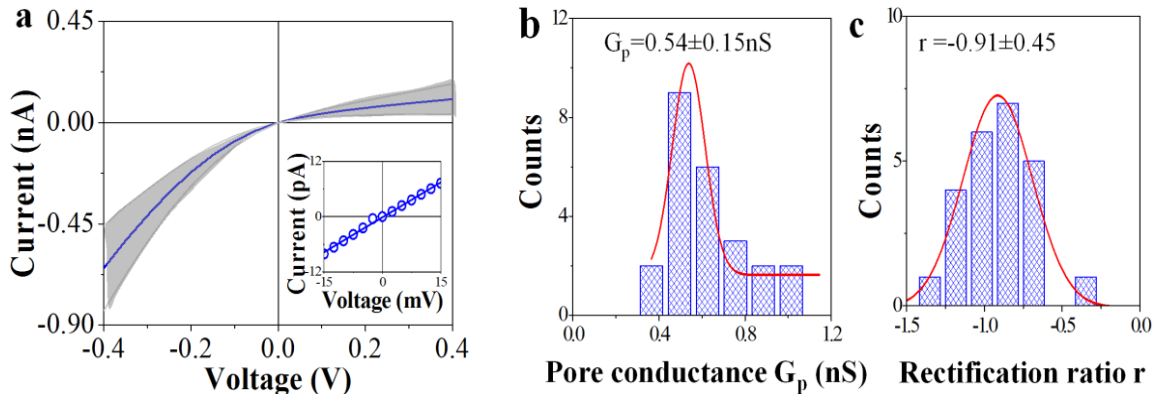
Figure 6.1: (a) The measured I-V curves for 24 non-modified nanopipettes in 25mM KCl. The mean I-V is showed as the solid line, and the standard deviation is displayed by the grey area. Inset: An experimental I-V (open blue circles) curve with a linear fit (solid line) in the voltage range from -15 mV to +15 mV. (b) The pore conductance (G_p) histogram of 24 non-modified nanopipettes. The solid line is a Gaussian fit and the mean value of G_p is 0.54 nS. The conductance was determined from the slope of the I-V curve in the inset of (a). (c) The rectification ratio r (at ±0.4V) histogram of 24 non-modified nanopipettes and the mean value is -0.91.

In the bigger bias range, as shown in Figure 6.1a, the I-V curves are nonlinear. However, referring to the inset of Figure 6.1a, the I-V curves for the bare nanopipettes are always nearly linear and symmetric within the voltage range from -15 mV to +15 mV. The symmetry and linearity of the I-V curves suggested that the surface charge effect can be ignored. A G_p histogram for 24 nanopipettes is displayed in Figure 6.1b, and a nanopipette conductance of 0.54 ± 0.15 nS is obtained. Due to the conical shape geometry and large surface charge density, the measured I-V curves of nanopipette always show rectification behavior in the bigger bias range. To quantitatively compare the rectification, I used the definition of rectification ratio r as $r = \log \left| \frac{I_+}{I_-} \right|$ [19]. The rectification ratio r is zero when the I-V is symmetric. A histogram of the rectification ratio of 24 nanopipettes at ±0.4V is shown in Figure 8.1c and r = -0.91±0.45.

6.2.3: Surface functionalization

The quartz nanopipette surface was chemically modified according to the procedures as explained in Section 2.2. I have modified 74 nanopipettes; the successful rate of the first APTES modification step was about 35% (26 out of 74). The failure ones showed unstable, weak or negative rectification ratio of I-V curves. I expect this modification step to be more successful if the environmental humidity can be lowered (lab room humidity was 52-56% at 23°C). If the first ATPES modification step is successful, the successful rate of the following modification steps is about 73% (19 out of 26). I discarded the nanopipettes that did not show the corresponding changes of rectification in I-V curves. Out of the 19 hNgb-modified pipettes, 6 pipettes did not show reliable responses in Cyt c or Lsz measurements.

6.3: Results and discussion

6.3.1: Quartz nanopipette characterization

The details of quartz nanopipette fabrication are given in Section 2.2.3 and in the Methods section. The surface charge can be ignored at this small voltage range (inset of Figure 6.1a, simulation results in Chapter 7) and a simple analytical equation (Equation 2.3) can be used to derive the inner diameter. When using an average half-cone angle $\theta = 1.6_o$ and $G_p = 0.54 \pm 0.15$ nS, the derived inner diameter is 34 ± 11 nm and is very close to the SEM result. Therefore, an average inner diameter of 34 nm and an average half-cone angle of 1.6^o were used in the simulations (Chapter 7). The value of θ is consistent with the SEM observation. A similar half-cone angle has also been reported by another group [32].

The rectification phenomenon has been thoroughly studied experimentally and theoretically and is attributed to the surface charge and conical shaped nanopore geometry [33-35]. Assuming a uniform distribution of surface charge density at the quartz surface, the surface charge density can be estimated using numerical simulations by comparing with the measured rectification ratio at ± 0.4V. The surface charge density of quartz nanopipettes were determined by matching experimental and simulated (Chapter 7) I-V The determined surface charge density of -46 mCm^{-2} is in the range of reported surface charge densities of quartz and silica surface [36].

6.3.2: Human Neuroglobin immobilization and characterization

Human Ngb is a hexa-coordinated heme protein predominantly expressed in nerve tissues [37]. This protein has a molecular weight of 17 kDa [30] with a hydrodynamic diameter of 3.8 nm [38], and its isoelectric point (pI) is 5.4 [39], suggesting that hNgb is

a negatively charged protein at neutral pH. The total charge of hNgb was determined to be -4e using ProtParam [40]. It is critical to immobilize hNgb properly to preserve protein function and achieve adequate surface coverage. The procedures of anti-His antibody assisted hNgb immobilization is described in Chapter 2 (Section 2.2.3).
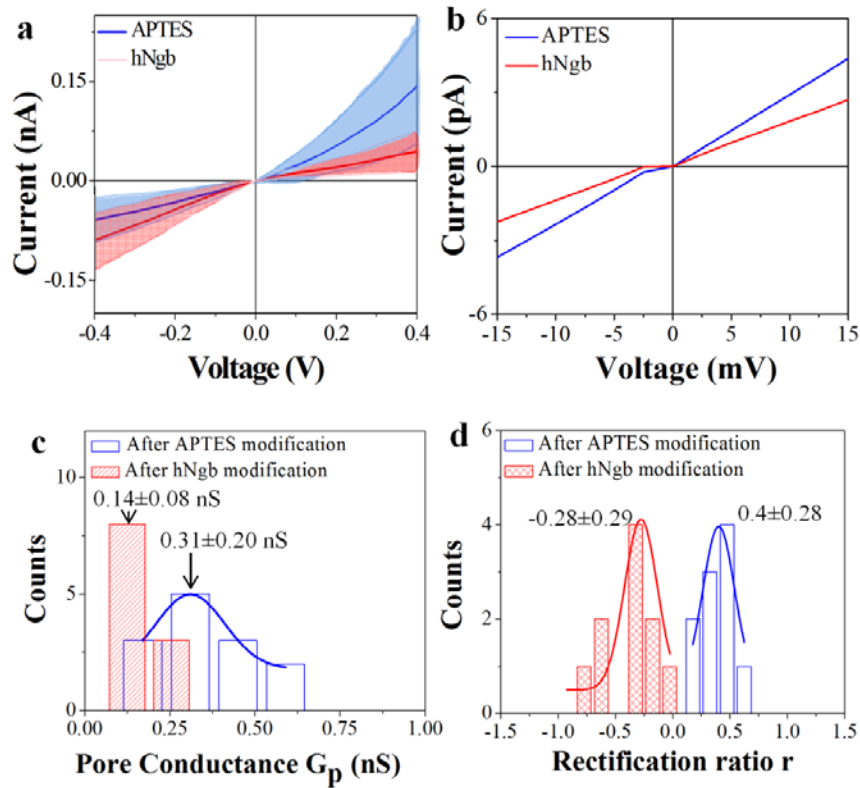
Figure 6.2: (a) The mean I-V of 11 APTES (blue) and hNgb-modified pipettes (red) is shown as the solid line and the standard deviation is displayed by the shadow area. The voltage sweep rate is 50 mV/s. (b) Typical I-V curves after the APTES (blue) and hNgb (red) modifications and in the low voltage range (-15 mV to +15 mV). (c) The G_p histogram of 11 nanopipettes after the APTES (blue empty columns) and hNgb modification (red partially filled columns). The conductance values (mean±s.d.) are 0.31±0.20 nS and 0.14±0.08 nS, respectively. (d) The rectification ratio r (at ±0.4V) histogram of 10 nanopipettes after APTES (blue empty columns) and hNgb (red partially filled columns) modifications. All measurements were performed in 25mM KCl and 2.5 mM PB buffer (pH=7.0).

Before using the anti-His antibody method, I first tested the amide bond method. The nanopipette was sequentially modified with poly-L-lysine (PLL) and polyacrylic acid (PAA) via electrostatic adsorption. Then the Cyt c proteins were immobilized to PAA through the amide bonds by using NHS-EDC coupling chemistry. Based on the

rectification ratio r of the modified nanopipettes, 1 out of 4 nanopipettes was modified. However, the measured ionic current was still not stable in my experimental conditions. I also tested the aldehyde-amino chemistry. In this method, the Cyt c proteins were covalently immobilized to the APTES modified nanopipettes through glutaraldehyde. Only 1 out of 6 nanopipettes showed satisfied Cyt c immobilization. Therefore, both methods did not work well as the anti-His antibody method. This may be attributed to the better controlled orientation of immobilized proteins and reduced modifications to the protein structure when using the anti-His antibody method. I monitored the surface modification by the change of I-V curves.

Figure 6.2a shows the typical I-V curves of the nanopipettes measured at neutral pH after the APTES modification and after the hNgb modification. As shown in Figures 6.2b and 6.2c, the pore conductance G_p in the small bias range reduces about 1.7 times after the APTES modification and about 4 times after the hNgb modification. Using Equation 2.3, the pore diameter was calculated to reduce from 34 nm to 18 nm after the APTES modification and to 11 nm after the hNgb modification. Using these diameters, I obtained the similar current reduction in numerical simulations (Chapter 7). Considering the molecular size, it can be speculated that APTES most likely formed a multilayer at the quartz inner surface. The pore size reduction after hNgb modification is mainly attributed to the adsorption of anti-His antibodies. The surface coverage of hNgb is low (see the last paragraph of Section 6.3.3); therefore, the effect of hNgb modification to the pore size is ignored. The overall shapes of I-V curves change with the surface modifications. At -0.4V, the ionic current is suppressed after the APTES modification but enhanced after the hNgb immobilization. The surface charge at neutral pH becomes

positive after the APTES modification due to the amine groups of APTES and becomes negative after the immobilization of negatively charged hNgb. As shown in Figure 6.2d, I obtained histograms of the rectification ratio r (at ±0.4V) after the APTES and hNgb modifications. The mean value of r is 0.4 after the APTES modification and -0.28 after the hNgb modification. The sign of r is changed from positive to negative, indicating that the surface charge polarity is changed from positive to negative.

The noise analysis of the modified nanopipettes supported the immobilization of hNgb (Section 2.2.3.2). As shown in Figure 6.3, the normalized noise always increases after hNgb modification. The increase of normalized noise can be attributed to the dynamic fluctuation of the modified proteins, which have been observed in lipid bilayer [41] and Nups proteins [42] modified nanopores. The noise analysis provides additional evidence of the surface modification of the quartz inner surface.
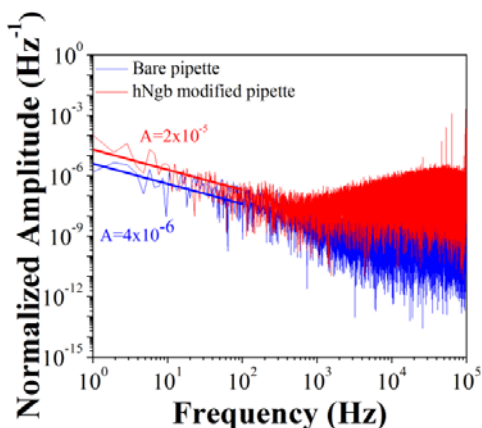
Figure 6.3: Normalized noise power spectrum for bare pipette (blue) and hNgb modified pipette (red).

The anti-His antibody assisted hNgb immobilization method was also confirmed by SPR (Chapter 3). SPR allows real-time and label-free studies of surface chemical modifications and protein-protein interactions. The gold surface cleaning and chemical modification procedures are explained in Section 2.1.2.2. The real-time chemical

modification of gold surface with cysteamine was confirmed at a flow rate of 0.05 mL/min. As shown in Figure 6.4a, the baseline changes after the glutaraldehyde (GA, step 2 of Figure 2.3) and anti-His antibody (step 3 of Figure 2.3) modifications indicate the successful chip surface modification. After the antibody modification, the functionalized chip surface was treated with 1 M ethanolamine (pH 8.0) to quench excess aldehyde groups. Figure 6.4b shows the SPR result of the immobilization of His-tagged hNgb onto the antibody surface (step 5 of Figure 2.3). The hNgb modified surface is quite stable and did not change much even after the flowing of 1 M NaCl solution.
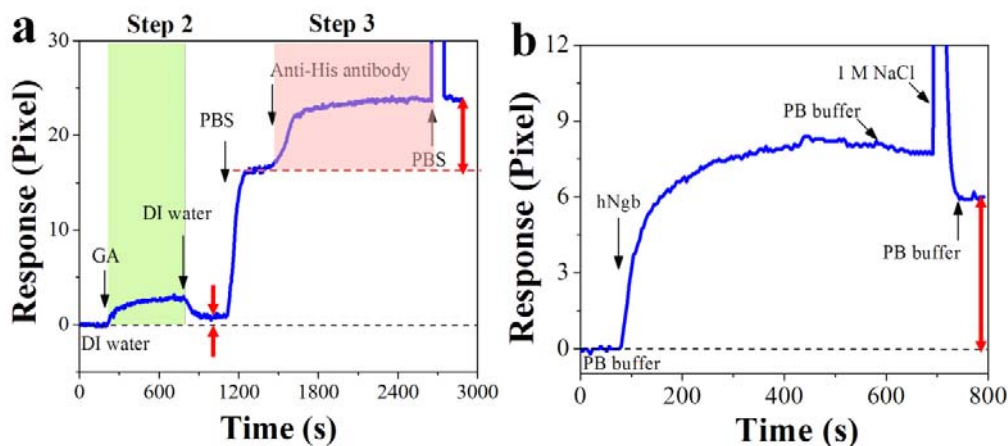
Figure 6.4: SPR results. (a) Real-time SPR response of the Glutaraldehyde and anti-His antibody modifications. (b) Real-time SPR response of hNgb modification to the anti-His antibody modified surface.

I also studied the stability of the immobilized hNgb at the quartz surface. Typical results are shown in Figure 6.5a. I compared the ionic current (at V = -0.4V) of the modified nanopipette after rinsing with buffered 25 mM KCl solution (trace 1) and after rinsing with 1 M NaCl (trace 2). To avoid pipette-to-pipette difference, I used a normalized ionic current I_n (I/I_o). To get I_n, the ionic current (I) is normalized by the average current I_o before any treatments. The magnitude of I_n only increased slightly after rinsing with 1 M NaCl solution, suggesting a very strong binding between hNgb and

antibody. The small variation can be attributed to the removal of a few non-specifically adsorbed hNgb molecules.
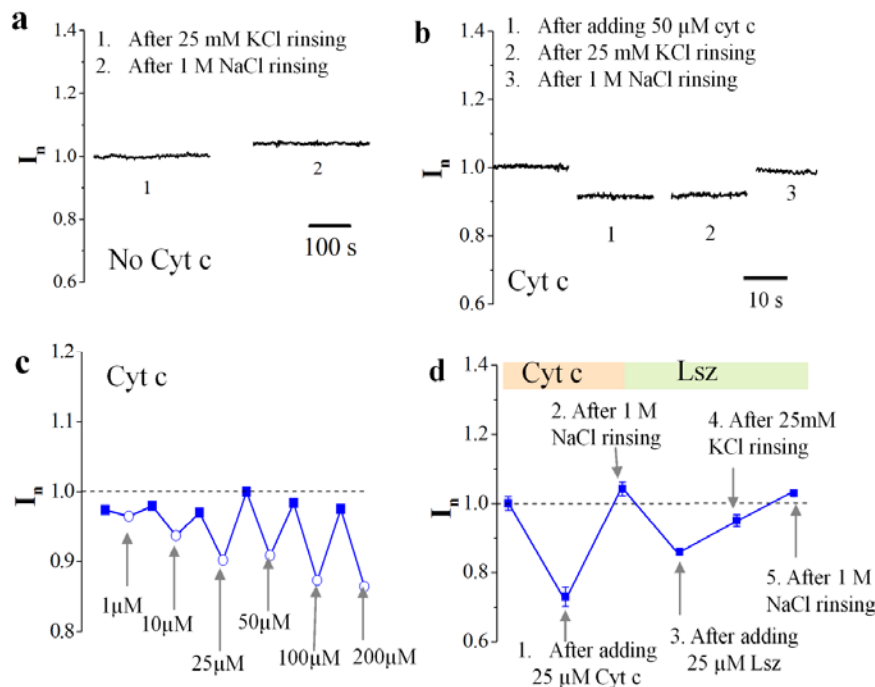
Figure 6.5: (a) Normalized current I_n time traces for the hNgb-modified nanopipette after 25 mM KCl rinsing (1) and after 1M NaCl rinsing (2). (b) I_n-t traces for a hNgb modified nanopipette after sequentially adding 50μM Cyt c (1), 25 mM KCl rinsing (2) and 1M NaCl rising (3). (c) The regeneration of a nanopipette. The solid squares represent I_n after 1M NaCl treatment and the open circles represent I_n after adding Cyt c with a series of concentrations. (d) The change of In for a hNgb modified nanopipette after sequentially adding 25 μM Cyt c (1), 1M NaCl rising (2), 25 μM Lsz (3), 25 mM KCl rinsing (4), and 1M NaCl rising (5). The data were the mean value of 10 seconds data and the error bar was from the standard deviation. All the results were measured at V = -0.4V.

The result in Figure 6.5a was confirmed by SPR measurements (Figure 6.4b), which showed that 1 M NaCl could not remove His-tagged hNgb molecules that bonded to anti-His antibodies. Based on my experience, the hNgb modified nanopipettes are stable for about 2 days if stored at 4°C.

6.3.3: Binding affinity

Cyt c is another heme protein that is expressed in mitochondria of all aerobic organisms [43]. The Cyt c is a globular protein with a molecular weight of 12.4 kDa and

96

a hydrodynamic diameter of 2.5-3.4 nm [44]. Its pI is 10.2 [45], therefore, it is positively charged (with approximately +9e) at neutral pH. Because Cyt c and hNgb proteins have opposite charges at neutral pH, their binding is initialized by the electrostatic interaction. Based on the computational results of molecular docking, Cyt c binds to Ngb specifically at the exposed heme site through dipole-dipole interactions [46].

In order to use nanopipettes to study the interaction between hNgb and Cyt c, I measured the response of ionic current through hNgb-modified nanopipette after adding Cyt c in the bath solution. As shown in Figure 6.5b, I measured the ionic current at a fixed bias V = -0.4V after adding 50 µM Cyt c in the bath solution. The measurement was made after waiting for several minutes until the current was stabilized. An obvious decrease in the magnitude of I_n was observed (1 of Figure 6.5b). The decrease of I_n is attributed to the reduction of negative surface charge density because of the binding of positively charged Cyt c molecules to negatively charged hNgb molecules at the quartz surface. Next, I rinsed the pipette tip with 25 mM KCl solution and measured the ionic current again with no Cyt c in the bath; no obvious change of I_n was observed (2 of Figure 6.5b). This suggested that the Cyt c-hNgb complex was stable during 25 mM KCl solution rinsing. We then rinsed the pipette tip with 1 M NaCl and 25 mM KCl solution, sequentially. The measured ionic current (3 of Figure 6.5b) almost returned to its initial current level. This result suggested that 1 M NaCl solution can effectively weaken the interactions between Cyt c and hNgb, and remove adsorbed Cyt c proteins. Therefore, 1 M NaCl can be used to regenerate the hNgb modified nanopipette surface after Cyt c binding. With this simple regeneration method, I investigated the current response of the same hNgb modified nanopipette to a series of Cyt c concentrations. One typical result is

shown in Figure 6.5c. The change of I_n magnitude is correspondingly larger when the Cyt c protein bath concentration is higher. For comparison, I studied the interactions between hNgb and lysozyme (Lsz) proteins. Similar to Cyt c, Lsz is also a globular protein with a molecular weight of 14.3 kDa [47] and a hydrodynamic diameter of 3.8 nm [48]. Lysozyme protein has net a positive charge (+8e) at pH=7.0 [49]. One example of the Lsz experiment is shown in Figure 6.5d. After exposing hNgb-modified nanopipettes to 25μM Lsz, the magnitude of I_n is reduced as well, due to the adsorption of positively charged Lsz. The reduction is normally smaller than the case of Cyt c with the same concentration, which can be attributed to a reduced number of adsorbed Lsz molecules at steady state. In addition, the reduced current is often partially or fully recovered after 25 mM KCl solution rising (4 of Figure 6.5d). This is very different from the Cyt c data in Figure 6.5b.

These observations, including the breaking of Cyt c-hNgb complex with 1M NaCl but not with 25 mM KCl, were also confirmed by SPR measurements. Figure 6.6a shows the typical SPR results when different concentrations of Cyt c were flowed over the hNgb-modified surface (Figure 6.4b). After the ~820 s of Cyt c injection, 25 mM KCl solution was flowed over the chip surface, which could not break Cyt c-hNgb pairs. However, the flow of 1 M NaCl solution could successfully remove Cyt c from the surface, and hNgb surface was regenerated. Control SPR experiments were also carried out to study the interactions between Lysozyme (Lsz) and hNgb. As shown in the sensorgrams of Figure 6.6b, the Lsz-hNgb complex is highly dissociable. After treated with 25 mM KCl, there is a large decrease of the response signal, and the response signals lost protein concentration dependence (as indicated by red arrow). In contrast, the

Cyt c-hNgb complex is stable during 25mM KCl flowing. Therefore, the interaction between hNgb and Lsz is not specific and different from the more specific interaction between Cyt c and hNgb.
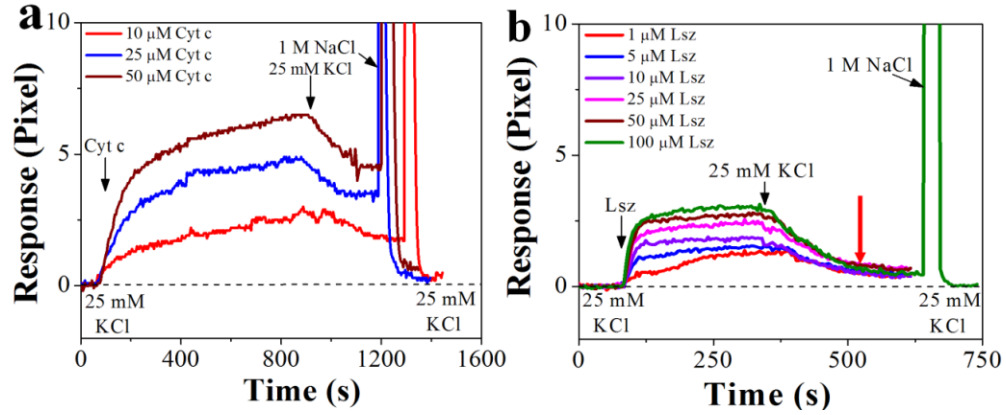
Figure 6.6: SPR results. (a) SPR response vs. time at different Cyt c concentrations (red color, 10µM; blue color, 25µM; and brown color, 50 µM) showing Cyt c-hNgb complex formation, dissociation, and surface regeneration. The immobilized Cyt c proteins cannot be removed by 25 mM KCl but can be removed by 1 M NaCl. b) SPR sensorgrams for Lsz binding to hNgb.

To quantitatively study the interactions between the proteins, I monitored the dynamic change of a normalized ionic current change $\Delta I_n = \frac{-(I-I_o)}{I_o}$ immediately after manually injecting 250 µL concentrated Cyt c solution in the 750 µL bath solution. Aided by the perturbations during the solution injection, the color of the whole bath solution uniformly became pale red in one second. I, therefore, concluded that Cyt c concentration in bath solution can reach a designed value in at most several seconds. I also estimated how long it will take for the solution in the nanopipette tip region to achieve bath Cyt c concentration. As suggested by the numerical simulation results explained in the following chapter (Chapter 7), it can just be considered the surface charge variation in the 2µm long pipette tip region. Because of the small diameter and half cone angle, the volume of the 2 µm long pipette tip is only about 6.7 attoliters. Therefore, there are only

about ~100 Cyt c molecules inside the effective volume at concentration 25 μM. The number of Cyt c molecules that can arrive at the pore mouth per second from the bath is largely controlled by diffusion and can be estimated by flux=$2\pi DCR_c$, where D is the diffusion constant of Cyt c (=6x10-7cm2/s, from Stokes' law and Einstein-Smoluchowski relation), C is Cyt c bath concentration, and R_c is the capture radius, which is normally larger than the actual pore size. Compared with nanopores drilled on thin films (i.e., silicon nitride membrane), it is not trivial to define the pore length of the nanopipette. Therefore the actual pore radius R=5.5 nm was used for the capture radius R_c, which will underestimate the protein flux. When the Cyt c bath concentration is 25 μM, the flux is about 3×10^4 proteins per second. After the proteins arrive at the pore mouth, they can be driven by electrophoresis to move 1 μm distance inside the pipette tip in less than 1 millisecond due to the enhanced electric field (about 10^5-10^6 V/m, simulation results, Figure 7.6a in the following chapter) at the pipette tip. Therefore, the Cyt c concentration inside and near the nanopipette tip should reach the bath solution concentration in less than a few milliseconds, and this mass transport time can be neglected in the following discussions. The current time traces for various Cyt c bath concentrations are shown in Figure 6.7a.

The big spikes at the beginning of each trace are due to the disturbance by manual addition of proteins that takes about 10 seconds. This noise marked the start point of the traces. I aligned all the traces according to the onset position of the spikes. The gradually rising ΔI_n can be attributed to the binding kinetics between Cyt c and hNgb. After several minutes (i.e., after 4 minutes in Figure 7.8a), the normalized current change reached a steady state value of ΔI_{neq}, (indicated by the green shadow area). Interestingly, stepwise

current changes often appeared in the traces with low Cyt c concentrations (i.e., traces 2 and 3 in Figure 6.7a).
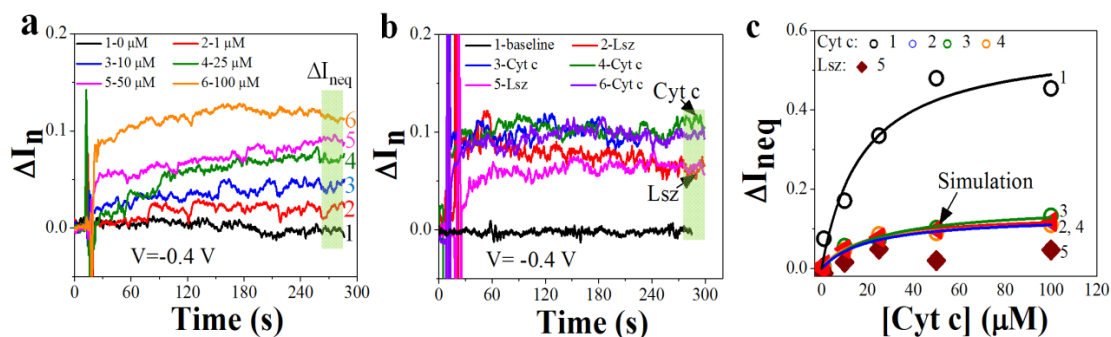
Figure 6.7: (a) ΔI_n-t traces for a hNgb modified nanopipette (pipette 2) after adding Cyt c in the bath solution with various concentrations (0-100 µM). (b) ΔI_n-t traces for a hNgb modified nanopipette after sequentially adding 25 µM Cyt c or 25 µM Lsz in the bath solution (step 2 and step 5 are Lsz; step 3,4, and 6 are Cyt c). The displayed data in Figures 6.7a and 6.7b have the time interval of 0.1s between two points. (c) Curves 1-4, normalized current change at equilibrium ΔI_{neq} as a function of Cyt c concentration. Curve 5 (brown diamond dots) is taken from Lsz and is shown here for comparison. The red triangle dots are simulated results as will be presented in the following chapter (Chapter 7). The solid lines are fitting curves using Equation 6.1.

At 1µM, there are only about four free Cyt c molecules at a steady state in the tip with attoliter sensing volume. These stepwise changes may reveal protein-protein interactions at the single molecule level. More experiments will be carried out in the future to obtain further insight about this phenomenon. As a control, I also recorded ΔI_n after adding 25 µM Lsz in the bath solution and the results (pink and red curves) are shown in Figure 6.7b. The same pipette was used to measure ΔI_n response when sequentially adding Lsz and Cyt c in the bath solution. Between the measurements, the 1M NaCl rinse was used to regenerate the pipette surface. In the repeated experiments, smaller ΔI_{neq} was always observed for Lsz after reaching steady state (green shadow area). Therefore, ΔI_{neq} can reflect the interaction strength between proteins. Compared to Cyt c, the decrease of ΔI_{neq} for Lsz is obvious but not significant. This can be attributed to the following reasons: 1) the relative weak interaction between Cyt c and hNgb; 2) the

small number of proteins contributed to ΔIneq; and 3) the nonspecific adsorption of Lsz to the surface.

Using the data shown in Figure 6.7a, I plotted the relationship between ΔI_{neq} and the Cyt c concentration. The results of 4 pipettes are shown in Figure 6.7c. These plots can be fitted by:

$$\Delta I_{neq} = \frac{\Delta I_{Maxn}[Cyt\ c]}{[Cyt\ c]+K_d}$$ (6.1)

where, [Cyt c] is the concentration of Cyt c in the bath solution and K_d is the equilibrium dissociation constant. ΔI_{Maxn} is roughly the saturation value of ΔI_{neq} at a higher Cyt c concentration (i.e., at 100 μM) and can also be obtained from the fitting. By fitting the experimental results ΔI_{neq}-[Cyt c] using Equation 6.1 (solid lines in Figure 6.7c), I obtained ΔI_{Maxn} and K_d for Cyt c-hNgb interactions. Although ΔI_{neq} and ΔI_{Maxn} varied significantly, K_d values are quite similar. The average K_d value is 20 ± 4 μM. In a control experiment, I also studied ΔI_{neq} as a function of the Lsz concentration. As shown in Figure 6.7c (pipette 5), the Lsz concentration dependence of ΔI_{neq} is weak with obvious fluctuation. I could not fit the data using Equation 6.1 with R^2 better than 0.5.

The SPR experiments were also performed between the proteins pairs in the same buffered 25 mM KCl solution. After the quasi-equilibrium response for Cyt c-hNgb interaction is reached (Section 3.3.6), as shown in inset of Figure 6.8, 25 mM KCl solution was flowed over the chip surface. For simplicity, the K_d for the Cyt c-hNgb interactions was determined using equilibrium analysis method. Figure 6.8 shows the SPR response vs. Cyt c concentrations over hNgb-immobilized surface (Figure 6.4b). Equation 3.5 was used to fit the experimental data and a K_d value of ~16 μM was

obtained. A similar K_d value for Cyt c binding to dithiothreitol (DTT) reduced hNgb in Tris buffer has also been reported [46]. The average K_d value ($\sim$20 μM) obtained from nanopipette experiments are very similar to the K_d value ($\sim$16 μM) obtained from SPR experiments.
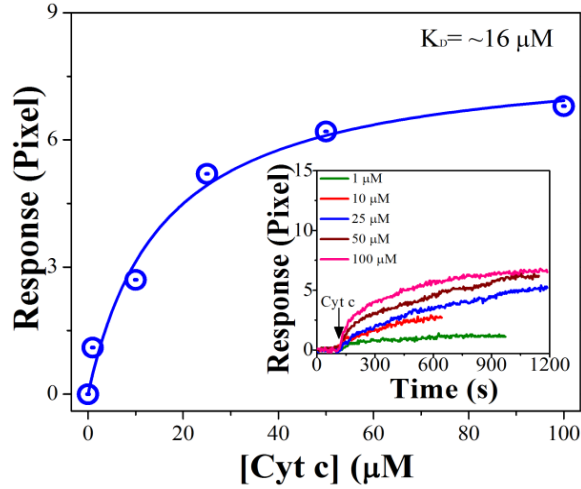
Figure 6.8: SPR response vs. Cyt c concentration plot. The experimental data (open circles) were fitted (continuous line) using Equation 5.4. Inset: concentration dependent SPR sensorgrams.

I also estimated the effect of the applied voltage on the measured K_d. The electric force slightly weakens the binding strength and an equation $K_d(V) = K_d(V = 0) \exp(\frac{F(V,x)x_\beta}{k_B T})$ can be used to make a simple estimation. In this relationship, x_β is the binding length of the protein pairs, the electric force $F(V,x)=E(V,x)Q$. As a crude estimation, 1nm for x_β and +9e for the net charge Q of Cyt c were used. I used the value Electric field (E) resulted from numerical simulation (Chapter 7). To simplify the calculation, constant value 4×10^5 Vm^{-1} was used here for the electric field. With these approximations, I got $K_d(V) = K_d(V = 0) \times 1.15$. Therefore, K_d (V=0) = 17.4 μM and this corrected value is closer to the SPR result.

I have obtained K_d of hNgb and Cyt c pairs from seven nanopipettes. Four of them gave similar K_d values near 20 μM as shown in Figure 6.7c. The other three nanopipettes gave values 35-60 μM. Considering the substantial fluctuations in the nanopipette radius and surface charge density, the reproducibility of K_d is very good. This is because K_d is determined by the ratio $\Delta I_{neq}/\Delta I_{Maxn}$ at a series of the Cyt c concentrations, and the ratio should be independent of pore radius R, half-cone angle θ, and the surface charge. The PNP numerical simulation results (Chapter 7), confirmed that ΔI_{neq} and ΔI_{Maxn} change correspondingly with the variation of R and θ. And the higher sensitivity (larger ΔI_{neq}) can be achieved when the nanopipette has smaller R and θ. Using similar experimental conditions in numerical simulations (Chapter 7), the experimental results of ΔI_{neq}-[Cyt c] plots in Figure 6.7c was also reproduced.

Based on simulation results (will be explained in Chapter 7), a linear relationship between ΔI_{neq} and $\Delta\sigma$ was obtained as shown in Equation 7.2:

$$\Delta I_{neq} = \alpha\Delta\sigma \qquad (7.2)$$

where, α is a function of R, θ and V and is obtained from the slope of the ΔI_{neq}-$\Delta\sigma$ plot. In the experiments, $\Delta\sigma$ is induced by the adsorption of positively charged Cyt c, which carries +9e charges at neutral pH. Based on a simple estimation (assuming the net charge of Cyt c will not change when forming Cyt c-hNgb complexes), $\Delta\sigma$ is given by Equation 7.3:

$$\Delta\sigma = \frac{\theta_{Cytc} \times N_{hNgb} \times 9e}{A} \qquad (7.3)$$

where, N_{hNgb} is the total number of immobilized hNgb proteins in the effective quartz surface area $A = 18 \times 10^{-14}$ m^2 (2 μm long pipette section), and θ_{Cytc} is the surface

coverage of Cyt c. From the Langmuir adsorption model, $\theta_{Cytc} = \frac{[Cyt\ c]}{[Cyt\ c]+K_d}$. Combining

Equations 7.2, 7.3 and Langmuir adsorption model, it is obtained:

$$\Delta I_{neq} = \frac{\alpha \times N_{hNgb} \times 9e}{A} \frac{[Cyt\ c]}{[Cyt\ c]+K_d} \qquad (7.4)$$

Comparing Equations 7.1 and 7.4, it is obvious that $\Delta I_{max} = \frac{\alpha \times N_{hNgb} \times 9e}{A}$. Therefore, ΔI_{max}

is proportional to the immobilized hNgb molecules. As mentioned earlier, ΔI_{max} can be

derived from the experimental results in Figure 6.7c. I, therefore, can estimate the total

effective number of immobilized hNgb molecules. I obtained 262 molecules for pipettes

2 and 4, 322 for pipette 3 and 1168 for pipette 1. Obviously, the sensitivity of pipette 1 is

better than other pipettes due to the presence of more receptors. For pipette 2, there are

about 12 Cyt c proteins binding to hNgb at a steady state in the 2μm long pipette tip

section of pipette 2 when the bath Cyt c concentration is 1μM and K_d is 20 μM. This

estimation confirms that the stepwise change in Figure 6.8a is induced by a few

molecules and suggests that the nanopipette can sense the surface charge change at the

single molecule level. Assuming hNgb molecules are uniformly distributed and based on

the footprint size of individual protein, the surface coverage of hNgb protein near the

nanopipette tip is estimated to be below 10%. This surface coverage is low.

Consequently, the diameter change induced by the hNgb modification and Cyt c

adsorption can be ignored. If the surface modification to increase the surface density of

receptor hNgb can be improved, it should also be able to enhance the sensitivity of the

nanopipettes and detect analyte (Cyt c) induced current change at a much lower Cyt c

bath concentration. The above estimations ignored the fluctuation of the protein net

charge and assumed a uniform distribution of receptor hNgb. The deviation of these

assumptions will certainly affect the estimated results. However, the main conclusions from these estimations should still hold.

6.4: Conclusions

In summary, I have demonstrated that quartz nanopipettes with attoliter effective volumes can be used as a reliable and label-free analytical method to quantitatively and reversibly study protein-protein interactions based on the surface charge sensing. Although the variations of geometry and surface modification of nanopipettes affect the normalized current change, these changes do not affect the measured binding affinity significantly. Therefore, reproducible binding affinity for protein pairs can be obtained. I also demonstrated that the surface charge sensing method of nanopipette can detect the current change induced by the adsorption of a few proteins. It has the potential to reach single protein sensitivity. Numerical calculations and analytical models were used to help understanding the surface charge sensing mechanism of nanopipettes.

6.5: References

1. P.B. Tiwari, L. Astudillo, J. Miksovska, X. Wang, W. Li, Y. Darici, J. He, Nanoscale 2014, 6, 10255.

2. J. Kasianowicz, E. Brandin, D. Branton, D. Deamer, Proc. Natl. Acad. Sci. U.S.A. 1996, 93, 13770.

3. D. Branton, D.W. Deamer, A. Marziali, H. Bayley, S.A. Benner, T. Butler, M. Di Ventra, S. Garaj, A. Hibbs, X.H. Huang, S.B. Jovanovich, P.S. Krstic, S. Lindsay, X.S.S. Ling, C.H. Mastrangelo, A. Meller, J.S. Oliver, Y.V. Pershin, J.M. Ramsey, R. Riehn, G.V. Soni, V. Tabard-Cossa, M. Wanunu, M. Wiggin, J.A. Schloss, Nat. Biotechnol. 2008, 26, 1146.

4. B.M. Venkatesan, R. Bashir, Nat. Nanotechnol. 2011, 6, 615.

5. L.T. Sexton, L.P. Horne, S.A. Sherrill, G.W. Bishop, L.A. Baker, C.R. Martin, J. Am. Chem. Soc. 2007, 129, 13144.

6. S. Howorka, Z.S. Siwy, Nat. Biotechnol. 2012, 30, 506.

7. W. Li, N.A.W. Bell, S. Hernández-Ainsa, V.V. Thacker, A.M. Thackray, R. Bujdoso, U.F. Keyser, ACS Nano 2013, 7, 4129.

8. Y.P. Shan, P.B. Tiwari, P. Krishnakumar, I. Vlassiouk, W.Z. Li, X.W. Wang, Y. Darici, S.M. Lindsay, H.D. Wang, S. Smirnov, J. He, Nanotechnology 2013, 24, 495102.

9. D. Fologea, B. Ledden, D.S. McNabb, J. Li, Appl. Phys. Lett. 2007, 91, 053901.

10. C. Plesa, S.W. Kowalczyk, R. Zinsmeester, A.Y. Grosberg, Y. Rabin, C. Dekker, Nano Lett. 2013, 13, 658.

11. Y. Wang, K. Kececi, M.V. Mirkin, V. Mani, N. Sardesai, J.F. Rusling, Chemical Science 2013, 4, 655.

12. Y.S. Ang, L.-Y.L. Yung, ACS Nano 2012, 6, 8815.

13. W.-J. Lan, H.S. White, ACS Nano 2012, 6, 1757.

14. K. Zhou, L. Li, Z. Tan, A. Zlotnick, S.C. Jacobson, J. Am. Chem. Soc. 2011, 133, 1618.

15. D.S. Talaga, J. Li, J. Am. Chem. Soc. 2009, 131, 9287.

16. A. Han, M. Creus, G. Schürmann, V. Linder, T.R. Ward, N.F. de Rooij, U. Staufer, Anal. Chem. 2008, 80, 4651.

17. D.J. Niedzwiecki, J. Grazul, L. Movileanu, J. Am. Chem. Soc. 2010, 132, 10816.

18. H.-Y. Wang, Y.-L. Ying, Y. Li, H.-B. Kraatz, Y.-T. Long, Anal. Chem. 2011, 83, 1746.

19. B. Vilozny, P. Actis, R.A. Seger, Q. Vallmajo-Martin, N. Pourmand, Anal. Chem. 2011, 83, 6121.

20. D.J. Niedzwiecki, R. Iyer, P.N. Borer, L. Movileanu, ACS Nano 2013, 7, 3341.

21. R. Wei, V. Gatterdam, R. Wieneke, R. Tampe, U. Rant, Nat Nano 2012, 7, 257.

22. P. Actis, A.C. Mak, N. Pourmand, Bioanal. rev. 2010, 1, 177.

23. L.J. Steinbock, O. Otto, C. Chimerel, J. Gornall, U.F. Keyser, Nano Lett. 2010, 10, 2493.

24. X. Gong, A.V. Patil, A.P. Ivanov, Q. Kong, T. Gibb, F. Dogan, A.J. deMello, J.B. Edel, Anal. Chem. 2013, 86, 835.

25. T.R. Gibb, A.P. Ivanov, J.B. Edel, T. Albrecht, Anal. Chem. 2014, 86, 1864.

26. L.J. Steinbock, R.D. Bulushev, S. Krishnan, C. Raillon, A. Radenovic, ACS Nano 2013, 7, 11255.

27. B. Vilozny, A.L. Wollenberg, P. Actis, D. Hwang, B. Singaram, N. Pourmand, Nanoscale 2013, 5, 9214.

28. P. Actis, A. McDonald, D. Beeler, B. Vilozny, G. Millhauser, N. Pourmand, RSC Adv. 2012, 2, 11638.

29. N. Sa, Y. Fu, L.A. Baker, Anal. Chem. 2010, 82, 9963.

30. T. Brittain, J. Skommer, K. Henty, N. Birch, S. Raychaudhuri, IUBMB Life 2010, 62, 878.

31. Y. Sun, K. Jin, X.O. Mao, Y. Zhu, D.A. Greenberg, Proc. Natl. Acad. Sci. U.S.A. 2001, 98, 15306.

32. M. Caldwell, S.J.L. Del Linz, T.G. Smart, G.W.J. Moss, Anal. Chem. 2012, 84, 8980.

33. H.S. White, A. Bund, Langmuir 2008, 24, 2212.

34. C. Wei, A.J. Bard, S.W. Feldberg, Anal. Chem. 1997, 69, 4627.

35. S. Umehara, N. Pourmand, C.D. Webb, R.W. Davis, K. Yasuda, M. Karhanek, Nano Lett. 2006, 6, 2486.

36. D. Stein, M. Kruithof, C. Dekker, Phys. Rev. Lett. 2004, 93, 035901.

37. T. Burmester, B. Weich, S. Reinhardt, T. Hankeln, Nature 2000, 407, 520.

38. C. Lechauve, H. Rezaei, C. Celier, L. Kiger, M. Corral-Debrinski, S. Noinville, C. Chauvierre, D. Hamdane, C. Pato, M.C. Marden, J. Mol. Biol. 2009, 388, 968.

39. D. Schaming, C. Renault, R.T. Tucker, S. Lau-Truong, J. Aubard, M.J. Brett, V. Balland, B. Limoges, Langmuir 2012, 28, 14065.

40. G. E., H. C., G. A., D. S., W. M.R., A. R.D., B. A., In: The Proteomics Protocols Handbook J.M. Walker (Ed.), Humana Press, New Jersey, 2005, 571.

41. E.C. Yusko, J.M. Johnson, S. Majd, P. Prangkio, R.C. Rollings, J. Li, J. Yang, M. Mayer, Nat. Nanotechnol. 2011, 6, 253.

42. S.W. Kowalczyk, L. Kapinos, T.R. Blosser, T. Magalhaes, P. van Nies, Y.H. LimRoderick, C. Dekker, Nat. Nanotechnol. 2011, 6, 433.

43. R.E. Dickerson, T. Takano, D. Eisenberg, O.B. Kallai, L. Samson, A. Cooper, E. Margoliash, J. Biol. Chem. 1971, 246, 1511.

44. N. Khare, C.M. Eggleston, D.M. Lovelace, S.W. Boese, J Colloid Interface Sci. 2006, 303, 404.

45. T. Brittain, J. Skommer, S. Raychaudhuri, N. Birch, Int. J. Mol. Sci. 2010, 11, 2306.

46. S.H. Bønding, K. Henty, A.J. Dingley, T. Brittain, Int. J. Biol. Macromol. 2008, 43, 295.

47. M. Xu, V.A. Shashilov, V.V. Ermolenkov, L. Fredriksen, D. Zagorevski, I.K. Lednev, Protein Sci. 2007, 16, 815.

48. A.S. Parmar, M. Muschol, Biophys. J. 2009, 97, 590.

49. J.J. Grigsby, H.W. Blanch, J.M. Prausnitz, Biophys. Chem. 2001, 91, 231.

CHAPTER 7: FINITE ELEMENT BASED NUMERICAL SIMULATIONS

In Chapter 6, I introduced a new label free experimental technique in order to quantitatively study protein-protein interactions using quartz nanopipettes. This chapter deals with finite element based numerical simulations in order to support and to understand the nanopipette experimental results as presented in Chapter 6. The majority of the contents in this chapter have been adapted from my research results published in a peer reviewed paper [1].

7.1: Introduction

The artificial nanopores with surface charge show electrical characteristics that are very similar to biological pores [2,3]. The flux ions through the nanopipette pore orifice are responsible for the charge transport. Due to the interaction between these mobile charges with the fixed charges on the conical nanopore wall, an interesting phenomenon is observed, which is known as Ion current rectification (ICR) [2,4,5]. ICR is the deviation of current-voltage measurements from the ohmic behavior. In other words the current at one voltage polarity is larger compared to reduced current at the same voltage but opposite polarity [5]. When the diameter of the pore orifice is comparable to the Debye screening length, the charged conical nanopores result ICR [6].

The Nernst-Plank equation as shown in Equitation 7.1 explains the physical properties of transport of ionic species whereas the relationship of ion concentrations with electric potential is given by Poisson's equation as given by Equation 7.2 [5]:

$$\mathbf{J_i} = -D_i \nabla C_i - \frac{z_i R}{RT} D_i C_i \Delta \Phi + C_i \mathbf{u} \tag{7.1}$$

$$\nabla^2 \Phi = -\frac{F}{\epsilon} \sum_i z_i C_i \tag{7.2}$$

where, $\mathbf{J_i}$ is the ionic flux, D_i is the diffusion constant, C_i is the concentration, and Z_i is the charge of ionic species i. Φ is the electric potential, u is the fluid velocity, F is the Faraday constant, T is the temperature, and ϵ is the dielectric constant of the medium.

Herein, finite element based numerical simulations have been performed in order to support the nanopipette experimental results and to understand the fundamental charge sensing mechanism as presented in Chapter 6. Finite element based numerical simulations can be used to solve the problems that cannot be solved using analytical solutions [7].

7.2: Methods

7.2.1: Computation domain and mesh distribution

The schemes of the computation domain and mesh distribution are shown in Figures 7.1a and 7.1b, respectively. The whole computation domain was discretized into free triangular elements. Rigorous mesh refinement was performed with the maximum and minimum mesh sizes were 800 nm and 0.08 nm, respectively.
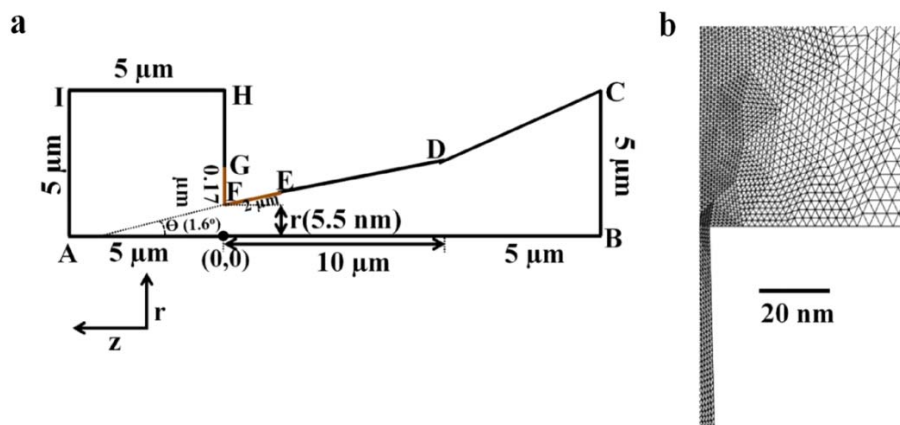
Figure 7.1: (a) Sketch of the computation domain for the nanopipette. The brown colored EF-FG section has surface charge. The drawing is not to scale. (b) Mesh distribution near the pore mouth.

Parameter	Value
Relative permittivity (ε_r)	80
Temperature (T)	298 K
Diffusion coefficient (K^+)	1.957×10^{-9} ($m^2 s^{-1}$)
Diffusion coefficient (Cl^-)	2.032×10^{-9} ($m^2 s^{-1}$)
Charge number (z_{K+})	1
Charge number (z_{Cl-})	-1
Maximum element (mesh) size	0.8 µm
Maximum element (mesh) size	0.08 nm
Maximum element growth rate	1.4
Resolution of curvature	0.3
Resolution of narrow regions	1
Number of refinements	3

Table 7.1: Parameters used in numerical simulations using COMSOL multiphysics.

Table 7.1 represents the parameters used to supply and appropriate boundary condition as mentioned in Table 8.2, for EF =2 µm, during simulations. The surface charge density of -4.5 mCm^{-2}, applied potential of -0.4 V, and 5.5 nm pore radius was used in the simulations.

Surface	Poisson's equation	Nernst-Plank equation
AB	Axial symmetry	Axial symmetry
BC	Constant electric potential	Constant concentration
CD	Zero charge	No flux (insulation)
DE	Zero charge	No flux (insulation)
EF	Surface charge density	No flux (insulation)
FG	Surface charge density	No flux (insulation)
GH	Zero charge	No flux (insulation)
HI	Zero charge	No flux (insulation)
IA	Ground	Constant concentration

Table 7.2: Selection of boundary values for the sketch as shown in Figure 7.1a.

7.2.3: Simulation

I carried out numerical simulations using Poisson-Nernst-Planck (PNP) equations based on the finite element method using the software package COMSOL Multiphysics 4.3b with chemical reaction engineering and AC/DC modules. Similar to previous reports

[5,6,8-10], the fluid dynamics was ignored and Navier-Stocks equations were not used in the simulation, therefore the term "$C_i\mathbf{u}$" in Equation 7.1 was ignored in the simulation. The simulation was verified by comparing the results with published results [6] under the same conditions. The ionic current was calculated by integration of the ionic flux density along the electrode cross-section area using Equation 7.3:

$$I = -F \int_S [\mathbf{J}(K^+) - \mathbf{J}(Cl^-)] \cdot \mathbf{n} \, dS \qquad (7.3)$$

I carried out numerical simulations using Poisson-Nernst-Planck (PNP) equations based on the finite element method. I only considered the surface charge distributed in the 2μm long section of the pipette tip. As shown in Figure 7.2, this simplification is reasonable and the calculated ionic current is accurate enough (less than 1% difference).
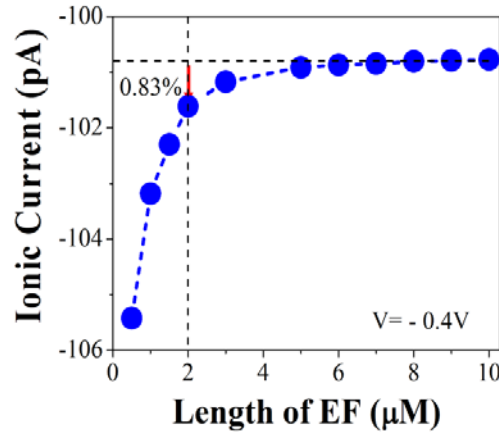
Figure 7.2: The ionic current at -0.4 V as a function of EF length (Figure 7.1a). The surface charge density σ of EF section is fixed at -4.5 mCm^{-2}. The simulated current magnitude for 2μm EF length is only about 0.83% higher than the one for 10 μm EF length. The half cone angle θ was always 1.6°.

7.3: Results and discussion

7.3.1: Effect of surface charge at low voltage

As confirmed by the numerical simulations (Figure 7.3) and previous reports [10,11], the surface charge can be ignored at this small voltage range (i.e., $V = k_B T/e$, where k_B is the Boltzmann constant, T is the temperature, and e is the elementary electron

charge) and a simple analytical equation (Equation 2.3) can be used to derive the inner diameter.
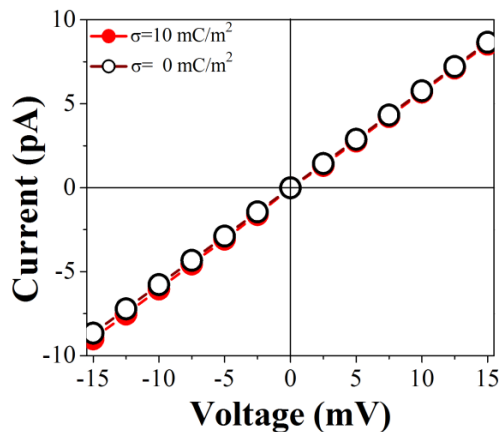
Figure 7.3: Simulated I-V curves (within -15 mV- +15 mV bias range) for the pipette with radius 17 nm in the presence and absence of surface charge. The half cone angle θ was always 1.6°.

7.3.2: Determination of surface charge density
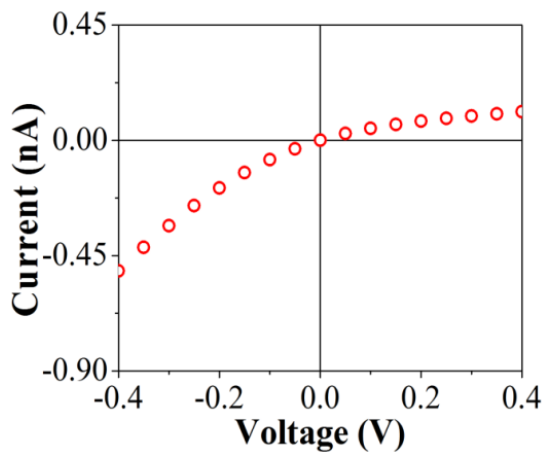
Figure 7.4: Simulated I-V curves for non-modified nanopipettes in 25mM KCl.

Assuming a uniform distribution of surface charge density at the quartz surface, the surface charge density can be estimated using numerical simulations by comparing with the measured rectification ratio at ±0.4V. As shown in Figure 7.4, the shape and

magnitude of the simulated I-V are close to the experimental results (Figure 6.1a) using a surface charge density of -46 mCm^{-2}.
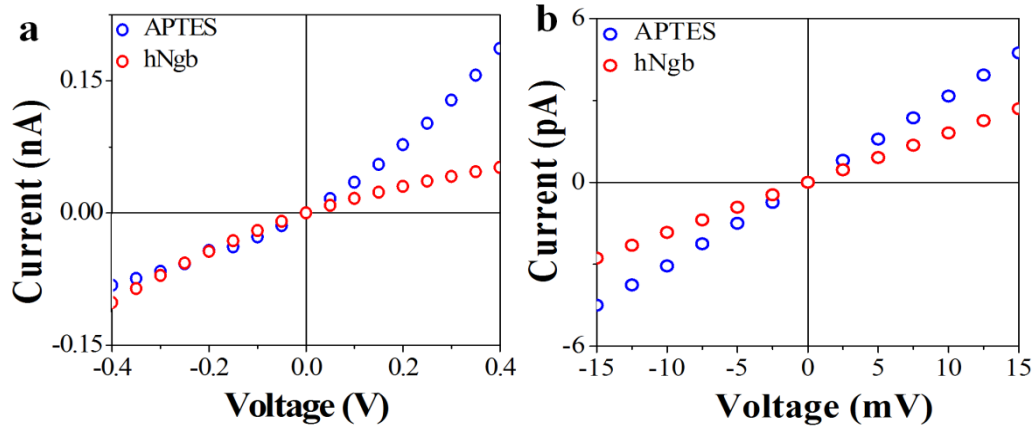
Figure 7.5: (a) The simulated I-V curves for APTES (blue circles) and hNgb modified pipettes (red circles). (b) The simulated I-V curves for after the APTES (blue) and hNgb (red) modifications and in the low voltage range (-15 mV to +15 mV). The simulation parameters are specified in the Methods section.

I calculated the I-V curves at various surface charge densities (σ) and polarities. As shown in Figure 7.5a, the nanopipettes with surface charge density of +10 mCm^{-2} and -4.5 mCm^{-2} can better match the experimental results (Figure 6.2a) of ATPES- and hNgb-modified nanopipettes, respectively. The simulated I-V curves at low bias range (-15 mV to +15 mV, Figure 7.5b) were also very similar to experimental results (Figure 6.2b). The above calculations were based on the uniform surface charge coverage assumption. I also used numerical simulations to understand the effect of non-uniform surface charge distribution to r when the average σ is the same.

Surface charge density for Surface 1, σ_1 (mCm^{-2})	Surface charge density for Surface 2, σ_2	Average surface charge density, $\sigma = (\sigma_1 + \sigma_2)/2$ (mCm^{-2})	Rectification ratio r
-6.5	-2.5	-4.5	-0.38
-2.5	-6.5	-4.5	-0.17
-4.5	-4.5	-4.5	-0.29

Table 7.3: Comparison of rectification ratio r.

As shown in Table 7.3, I compared the rectification ratio r for three different charge distributions. The 2 μm long charged section FE (Figure 7.1a) was divided into two equal halves. The first half starting from point F was named surface 1 and the second half was named surface 2. The magnitude of r was found to be larger if more charges locate near the pore and is smaller if more charges locate away from the pore. The variation of charge distribution can be one source of the experimental error for r.

7.3.3: Simulation for electric field distribution
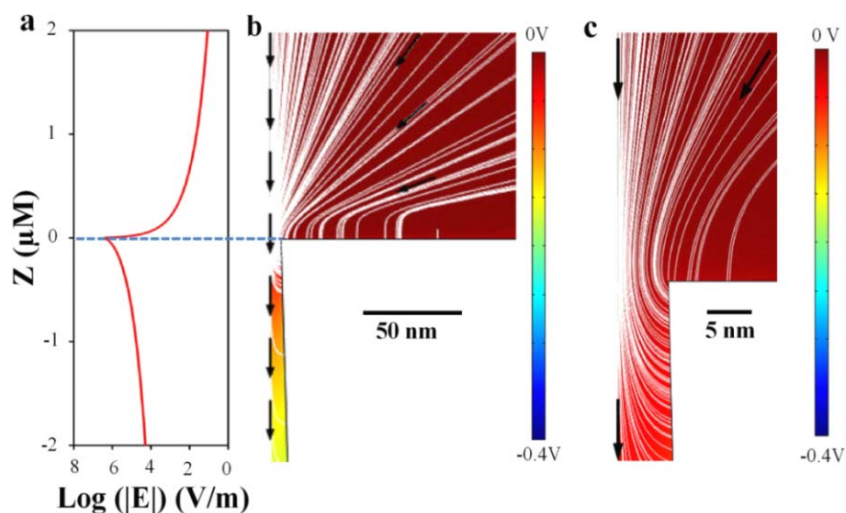
Figure 7.6: (a) Simulated electric field (E) distribution (in logarithmic scale) as a function of position along the pore axis z. (b) Color coded potential (V) distribution and electric field lines (white) within the same region of Figure 7.6a. The white lines visualize the electric field distribution and the arrows indicate the direction of the electric field. (c) The zoom in image of V and E distributions near the pore mouth. Applied bias was -0.4V in all the simulations.

In order to understand the electric field distribution near the pore, I performed numerical simulations. The electric field distribution along the pore axis was used in Chapter 6 in order to investigate the effect of applied voltage in the derived K_d value for Cyt c binding to hNgb. Figure 7.6a depicts the distribution of the simulated electric field (E), in logarithmic scale, as a function of position along the pore axis z. Figures 7.6b and

7.6c reveal the electric field E(x) distribution near the nanopipette tip when the applied bias is -0.4V. Figure 7.6c is the zoom in image of Figure 7.6b near the pore.

7.3.4: Pipette geometry and binding constant
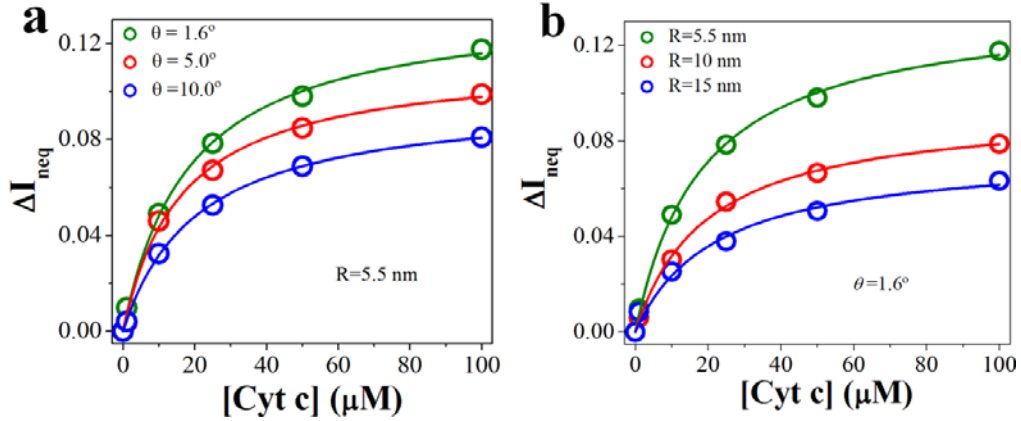
Figure 7.7: (a) Simulated ΔI_{neq}-[Cyt c] plots at different half cone angles. The pipette radius R was always 5.5 nm. (b) Simulated ΔI_{neq}-[Cyt c] plots at different pore radius. The initial surface charge density was -4.5 mCm^{-2}. All the simulated data (open dots) can be fitted (solid lines) using Equation 6.1 with K_d=20 μM.

As shown in the PNP numerical simulation results (Figures 7.7a and 7.7b), ΔI_{neq} and ΔI_{Maxn} change correspondingly with the variation of R and θ. Smaller R and θ induce larger ΔI_{neq} and ΔI_{Maxn}. However, $\Delta I_{neq}/\Delta I_{Maxn}$ remains same value and leads to the same K_d. These simulation results also suggest that the higher sensitivity (larger ΔI_{neq}) can be achieved when the nanopipette has smaller R and θ. As mentioned in Chapter 6 (Figure 6.7c), the numerical simulation reproduced the experimental results of ΔI_{neq}-[Cyt c] plots.

7.3.5: Charge sensing mechanism

To understand the charge sensing mechanism analytically, the nanopipette tip was first treated as a cylindrical nanochannel. Considering the very small half-cone angle, it is a reasonable first order approximation. The surface charge effect of a high aspect ratio nanochannel has been thoroughly investigated analytically and numerically [10,12,13]. For the analytical model, the ionic conductance through a long nanochannel has a linear

term proportional to the surface charge. Therefore, the relative current change should be proportional to the surface charge change $\Delta\sigma$. I also use PNP equations to numerically calculate ΔI_{neq} as a function of $\Delta\sigma$ for a nanopipette with the same R (5.5nm), θ (1.6^o), and σ (-4.5 mCm^{-2}) as in the experiments.

As shown in Figure 7.8, a linear relationship between ΔI_{neq} and $\Delta\sigma$ was obtained. Based on this relation and other analytical equations, the number of immobilized hNgb proteins and bound Cyt c proteins were estimated. These estimated results and related discussion have already presented in Chapter 6.
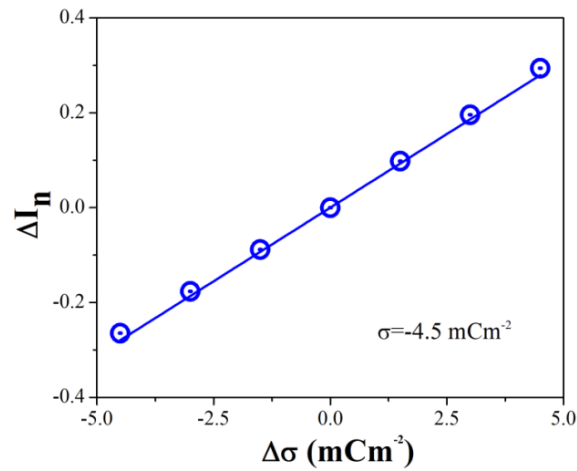
Figure 7.8: The simulated result (blue open circles) of ΔI_n as a function of $\Delta\sigma$. The continuous line is the linear fit.

7.4: Conclusions

Based on the numerical simulation results, the ionic current through the conical-shaped nanopipette was found to be very sensitive to the surface charge variation near the pore mouth. The numerical simulation results were useful not only to validate experimental nanopipette results but also very helpful in the understanding of fundamental charge sensing mechanism.

7.5: References

1. P.B. Tiwari, L. Astudillo, J. Miksovska, X. Wang, W. Li, Y. Darici, J. He, Nanoscale 2014, 6, 10255.

2. Z. Siwy, E. Heins, C.C. Harrell, P. Kohli, C.R. Martin, J. Am. Chem. Soc. 2004, 126, 10850.

3. C. Ho, R. Qiao, J.B. Heng, A. Chatterjee, R.J. Timp, N.R. Aluru, G. Timp, Proc. Nat. Acad. Sci. U. S. A. 2005, 102, 10445.

4. Z.S. Siwy, Adv. Funct. Mater. 2006, 16, 735.

5. H.S. White, A. Bund, Langmuir 2008, 24, 2212.

6. C. Kubeil, A. Bund, J. Phys. Chem. C 2011, 115, 7866.

7. Y. Tian, X. Liu, X. Li, In: Computational Intelligence and Intelligent Systems, Z. Cai, H. Tong, Z. Kang, Y. Liu (Eds.), Springer Berlin Heidelberg, 2010, 146.

8. J. Liu, M. Kvetny, J. Feng, D. Wang, B. Wu, W. Brown, G. Wang, Langmuir 2011, 28, 1588.

9. I. Vlassiouk, S. Smirnov, Z. Siwy, Nano Lett. 2008, 8, 1978.

10. I. Vlassiouk, S. Smirnov, Z. Siwy, ACS Nano 2008, 2, 1589.

11. Y. Wang, K. Kececi, M.V. Mirkin, V. Mani, N. Sardesai, J.F. Rusling, Chem. Sci. 2013, 4, 655.

12. D. Stein, M. Kruithof, C. Dekker, Phys. Rev. Lett. 2004, 93, 035901.

13. R.M.M. Smeets, U.F. Keyser, D. Krapf, M.-Y. Wu, N.H. Dekker, C. Dekker, Nano Lett. 2005, 6, 89.

CHAPTER 8: MASS TRANSPORT THROUGH VERTICALLY ALIGNED LARGE DIAMETER MWCNTs EMBEEDED IN PARYLENE

This chapter presents a nanopore technique to investigate the translocation of small ions through CNT based nanoporous membrane device. The majority of the contents of this chapter have been adapted from my research results published in a peer reviewed paper [1].

8.1: Introduction

In recent years, there has been enormous interest in utilizing carbon nanotubes as nanochannels or nanopores [2-9]. From a biological point of view, the CNT is an ideal model to help understand the transporter proteins on the cell membrane that work in aqueous environments with hydrophobic inner walls and nanometer channel sizes. CNTs have several advantages as nanopores or nanochannels. (1) They require no special nanofabrication to achieve a pore size of molecular size (ranging from less than 1 nm to more than 10 nm). They have an atomically smooth surface and perfect uniformity over long distances, resulting in frictionless motion of fluid and particles. (2) For high quality CNTs, the chemistry and structures of the interior surface are well defined, which simplifies theoretical simulations. (3) The excellent electrical properties of CNTs provide new routes to electrical detection, trapping and manipulation of charged biomolecules and nanoparticles. (4) Well defined sites are available for chemical functionalization at the ends of the tubes. Such modifications will be extremely useful for ion and molecule selection, gating or separation.

Recent research on CNT based nanofluidic devices has yielded exciting applications in efficient gas filtration, chemical and biological separation, water

desalination and programmable transdermal drug delivery [10-12]. I have used parylene deposited vertically aligned MWCNT forest membranes (about 7 nm in tube inner diameter and 42 μm in tube length). Parylene film is chemically inert, electrically resistive and pinhole free and has low permeability to moisture and gases. Parylene is also known for its capability to conformably cover all surfaces regardless of the configuration of the surface, including configurations with high aspect ratio [13,14]. MWCNT forests embedded in parylene have been used in several applications, including electrochemical sensors [14-16], but not as a membrane for mass transport.

Herein, I used this new type of CNT membrane to help improve the understanding of several aspects such as the transport of particles through CNTs under electric field. In this dissertation research, the translocation of small molecules and nanoparticles is studied, especially driven by an electric field. The flux of charged molecules through CNT nanopores is contributed by several factors as implied by Equation 8.1 [17-19]:

$$J_{pore} = -D\frac{dC}{dx} + \frac{\epsilon r^2 \Delta p}{8\mu\tau L} - \frac{zFDC}{RT}\frac{dU}{dx} + \vartheta_{eo}C \tag{8.1}$$

where, J_{pore} is the flux, D is the diffusion coefficient, C is solute bulk concentration, $\frac{dC}{dx}$ is the concentration gradient, ϵ is the relative porosity of the porous membrane, r is pore radius, p is applied pressure, μ is the dynamic viscosity, τ is the tortuosity, L is pore length, z is the number of unit charge of the solute, R is the molar gas constant, T is the absolute temperature, $\frac{dU}{dx}$ is the electric field gradient, and ϑ_{eo} is electro-osmotic velocity. The presence of fixed surface charge on the solid pore wall establishes a layer of opposite charges (counterions), in solution, in order to maintain electro-neutrality. This system, comprised of charges and the layer of counterions, is known as electrical double layer

(EDL). The two electrokinetic phenomena, electrophoresis and electro-osmosis, are the major means of transport of the charged molecules under the effect of applied electric field. The thickness of EDL and the mobile counterions affect the electrokinetics [20]. Electrophoresis is the drifting of charged species relative to their background aqueous medium [21] whereas electro-osmosis is the movement of the liquid medium, containing charged species, as a whole over the charged surface [20]. Depending upon charge and molecular structure of the charged species, they interact differently with nanopore walls. These interactions enhances the selectivity of CNT pores to the charged species [1].

Molecule-carbon surface interactions were found to play important roles in the transport of these particles. Under an electric field in the range of 4.4 $\times10^4$ Vm^{-1}, electrophoresis instead of electro-osmosis was found to be the main mechanism for ion transport. Small charged molecules and 5 nm gold nanoparticles can be driven through the membranes by an electric field. Due to the weak electric driving force, the interactions between charged molecules and the hydrophobic CNT inner surface play important roles in the transport, leading to enhanced selectivity for the small molecules.

8.2: Experimental methods

8.2.1: MWCNT forest growth and characterization and Parylene coated MWCNT forest membrane fabrication

Figure 8 depicts the characterization and schematic of the MWCNT forest membrane (Section 2.3.5) that was used in this dissertation for the investigation of the translocation of small charged molecules. Figure 8.1a represents SEM and Figure 8.1b represents low resolution TEM image of MWCNTs. The inset in top left corner in Figure 8.1b represents the high resolution image of one MWCNT and top right corner represents

the histogram of inner diameters of these MWCNTs. Parylene was deposited to coat the MWCNTs forest. Figure 8.1c represents the SEM image of the cross-section of the parylene coated MWCNT membrane. After parylene coating the substrate was treated with two step sequential RIE in order to remove excess parylene and SiN membrane from backside of the substrate.
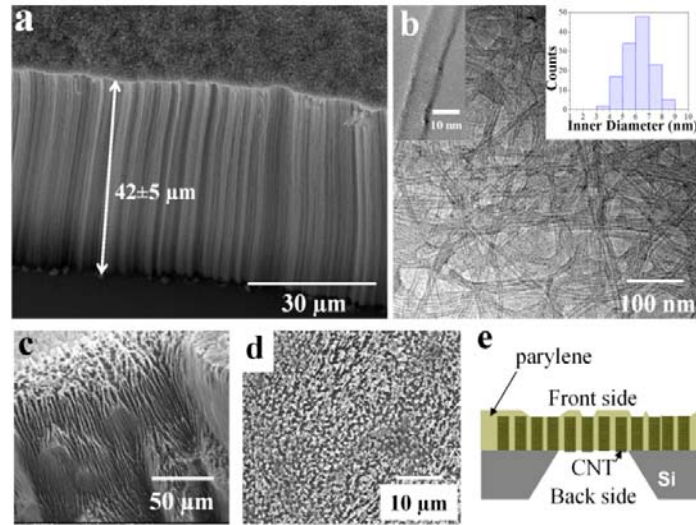
Figure 8.1: (a) SEM image of a cross-section of the as-grown vertically aligned MWCNT forest. The average height of the CNT forest is about 42 μm. (b) Low-resolution TEM image of a large number of MWCNTs. The inset in the top left corner is a high resolution TEM image of one MWCNT. The inset in the top right corner shows the histogram of inner diameters of these MWCNTs. (c) A SEM image shows the cross-section of the parylene coated MWCNT membrane. (d) A SEM image shows the membrane surface after oxygen plasma treatment. (e) A schematic diagram of the parylene encapsulated MWCNT forest membrane on a silicon support with a square window with size 35–100 μm.

I performed PAN etching of those samples as outlined in Section 2.3.2.2. The samples after PAN etching was then cleaned with copious amount of DI water and dried gently with Ar gas. Then oxygen plasma (2-4 min, 7.2 W, 550-600 mTorr) was then used to remove the excess parylene, and to expose and open the CNT ends. The surface of the membrane after oxygen plasma is shown in Figure 8.1d. The as-fabricated parylene surface is hydrophobic. However, the parylene surface becomes hydrophilic after oxygen

plasma treatment. The hydrophilic parylene surface is stable and facilitates the transport of particles. A schematic diagram of the final device is shown in Figure 8.1e. The "back side" and "front side" of the device are labeled in Figure 8.1e and the same definition is used to identify the two sides of the final device throughout this dissertation. Si/SiN substrates without MWCNTs growth (only with SiN window was opened at the backside, Figure 8.1e), was etched using KOH (Section 2.3.2.1) to fabricate the free standing SiN membranes). These SiN membranes were used in control experiments.

8.2.2: Porosity measurements

It is crucial to determine the space occupied by MWCNT pores compared to the total membrane space, which is called porosity. I measured the porosity of a CNT membrane (after 3 min oxygen plasma treatment) using a KCl diffusion method [22]. A pore area of 7.2×10^{-11} m^2 and porosity of 0.89% was obtained for one of the CNT membranes. Based on the average CNT diameter (7 nm), the obtained CNT area density was 0.23×10^{11} cm^{-2}. This is in line with estimates by other groups [8,23] but subject to considerable uncertainty, for example, the pore diameter estimated from the membrane conductance is about a factor three too large (an error that may also reflect enhanced ion mobility in the interior of the CNTs).

8.2.3: Materials, chemical reagents and solution preparation

5 and 10 nm gold nanoparticles (Au NPs) were purchased from Ted Pella. These gold nanoparticles are capped with negative citrate ligand and the size is very accurate, with only 10% size variation. No aggregation was observed when these particles were dissolved in pure water or aqueous solution with low salt concentration (<15 mM KCl solution) [24]. Other chemical reagents were purchased from Sigma Aldrich and used

without further purification. All solutions were prepared using deionized (DI) water (~18 MΩ) from a water purification system (Ultra Purelab system, ELGA/Siemens). The prepared salt solution was filtered through a 0.2 μm filter and degassed by sonication. For comparison, we also used anodic aluminum oxide (AAO) nanoporous membranes (Anodisc, Whatman) with pores of nominal diameter 20 nm and thickness of 60 μm. The AAO membrane was placed on the same silicon chip with a small opening in the center formed by breaking SiN membrane. The porosity of the AAO membrane is 25–50% of the total exposed surface area.

8.2.4: Measurement
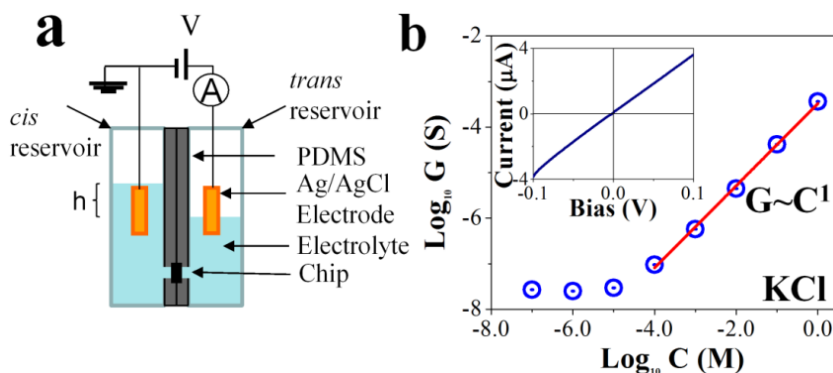
Figure 8.2: (a) Diagram of the ionic current measurement setup, h is the solution height difference between two reservoirs. (b) The ionic conductance versus KCl concentration on a log–log scale. The solid line is a linear fit to the experimental data. The inset shows the I-V curve of the membrane in 100 mM KCl solution.

The experimental setup is shown in Figure 8.2a. The fabricated CNT forest membrane was sandwiched between two flat PDMS slabs (Section 2.3.4) with punched holes (~1 mm diameter) as fluid pathways. The sandwich structure was further clamped between two polystyrene optical cuvettes with 1 mm diameter fluid holes. The measurement setup was placed in a home-built Faraday cage to reduce noise. Bias was applied through Ag/AgCl electrodes (prepared by dipping clean 0.25 mm diameter Ag

wire into bleach to a distance of 3-4 cm for 30 min) across the membrane at a fixed

distance (~1.2 cm). The applied bias was mostly below 2 V and never above 3 V to avoid

water electrolysis, electrode polarization, and electric potential damage to molecules.

The measurement was carried out at room temperature (22°C). No temperature

change in solution was observed when applying 3 V for 2 h across the CNT membrane.

The *cis* side was always grounded and the applied bias was defined as positive when the

potential at the *trans* side was more positive. The analytes were always added on the *cis*

side. The ionic current data were collected with a Keithley 2636 A sourcemeter (Keithley

Instruments). A pressure gradient was introduced by adjusting the height difference

between the water surface level in cis and *trans* reservoirs. No obvious change in the

height difference was observed for a 10 hours experiment. The measured ionic current of

the same device was normally stable for weeks if the membrane was rinsed properly and

stored in water all the time. As control experiments, I performed I-V measurements

without the presence MWCNT membrane in the ionic pathway. I also measured the ionic

conductance for the 1mm diameter PDMS channel at various concentration of KCl

solution, as shown in Figure 8.3a. The measured conductance values (solid blue triangles)

matched very well with the calculated conductance values (open blue triangles) using the

conductivities (σ) of KCl solutions and the geometry parameters of the PDMS channel

($G = \frac{\sigma A}{L}$, A and L are the cross-section area and length of the channel respectively). I also

put the measured the ionic conductance through the MWCNT membrane (same as Figure

8.2b) here for comparison. The current through the PDMS channel is about one order

higher than the current we measured through CNT membrane when the KCl

concentration is above 0.1mM and hence the electrical resistance of the fluidic pathway

(without the membrane) is at least one order smaller than the resistance of the CNT membrane.
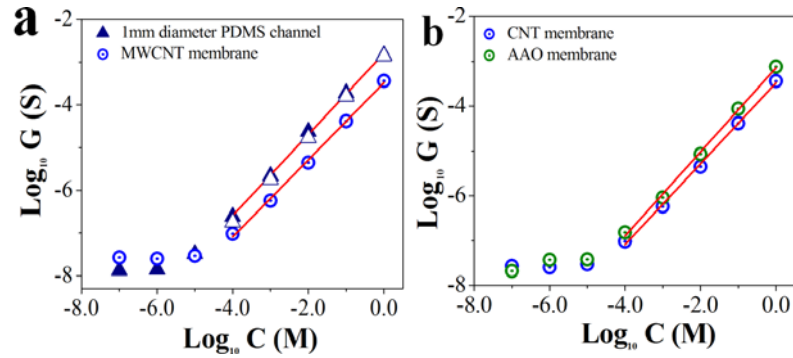
Figure 8.3: (a) The log-log plot of ionic conductance as a function of KCl concentration for both CNT membrane (blue open circles) and 1mm diameter PDMS channel (solid blue triangles). The experimental data (blue open circles and solid blue triangles) were fitted by linear functions and are plotted as solid lines (red). The open blue triangles are calculated conductance using $G = \frac{\sigma A}{L}$. (b) Log-log plot of ionic conductance as a function of KCl concentration for both CNT membrane (blue open triangles) and AAO membrane (open green circles). The experimental data were fitted by linear functions (solid red lines).

I also used Anodic aluminum oxide (AAO) nanoporous membranes (Anodisc, Whatman) with pores of nominal diameter 20 and thickness of 60μm. I first measured the ionic conductance through these AAO membranes as a function of KCl concentration. As shown in Figure 8.3b, the ionic conductance through AAO membranes is bigger (less than 10 times) comparing with MWCNT forest membranes. Considering the much bigger pore area of the AAO (25-50% porosity) membrane than CNT membrane (normally below 1%), an enhanced ionic flow through MWCNT membrane under an electric field is expected.

8.3: Results and discussion

I carried out several control experiments to prove that, within the applied bias and pressure range, the transport was through the inside of the CNT and not through the cracks and voids in the parylene film. I measured the ionic current through the membrane by using the setup as shown in Figure 8.2a. When the CNT membrane was not treated by

127

oxygen plasma, there was no measurable ionic current but the ionic current was detectable after 1 min oxygen plasma treatment. The oxygen plasma was generated at 10.2 W RF power in a quartz vacuum chamber with pressure of 550 mTorr. The result for one device is shown in Figure 8.4a.

I also studied the translocation of gold nanoparticles (Au NP) with well-defined size under pressure and electric field. The 5 nm Au NP is smaller than the average CNT inner diameter and the 10 nm Au NP was larger than the average CNT inner diameter. I measured more than 10 membranes and about 80% of the membranes only allow 5 nm Au NPs to pass with only electric field applied (Figure 8.5b). However, the ratio was reduced to about 40% when a pressure (294 Pa, about 3 cm height difference) was applied. I discarded the 60% membranes that also allowed the passage of 10 nm NPs. This fact also suggests that these parylene encapsulated CNT membranes are not suitable for high pressure applications. Therefore, I mainly studied the transport driven by electrical field. If a pressure gradient was needed, the pressure was always below 294 Pa, a level at which no leaks were detected in the parylene membranes.
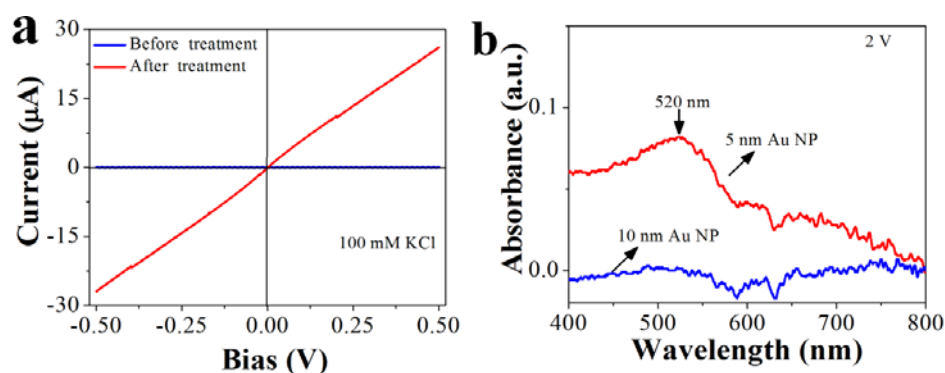

Figure 8.4: (a) I-V curves as before and after oxygen plasma treatment of one device. (b) UV–vis spectra of 5 nm (red) and 10 nm (blue) Au nanoparticles at the *trans* reservoir after applying a 2 V bias for 6 h. No pressure is applied. The concentration of Au NPs at the *cis* reservoir is 60 µM in 1 mM KCl solution.

To understand the ion transport mechanisms in these large diameter MWCNTs, I measured the ionic conductance in KCl solution as a function of KCl concentration. I first measured the ionic current through the CNT forest membrane at different bias. The current-voltage curves were symmetric in the applied bias range (<2 V), and a typical curve taken in 100 mM KCl solution is shown in the inset of Figure 8.2b. The ionic conductance can be derived from the slope of the I-V curve. I then plotted the ionic conductance data as a function of KCl concentration in a logarithmic scale. As shown in Figure 8.2b, the ionic conductance was proportional to the KCl concentration when it is above 0.1 mM. A deviation was observed when the concentration was below 0.1 mM. The deviation at low salt concentration was previously explained by surface charge on the nanochannel/nanopore [25]. However, the conductance departs from a linear relationship at much higher salt concentration (>10 mM) for silica nanochannels with surface charge density ~60 mCm^{-2} at pH 7. Even for an octadecyltrichlorosilane (OTS) modified silica channel with significantly reduced surface charge density, the deviation appears at around 1 mM KCl concentration [25]. Therefore, I concluded that the surface charge density at the inner surface of MWCNTs was extremely low. The following are possible reasons why the surface charge density is low at the inner surface of the MWCNTs. (1) Because of the inert nature of CNT inner surface; there are very few charged groups at the CNT inner surface. Charged groups (i.e. carboxyl groups) distribute mostly at the CNT ends. (2) The CNT inner surface may also acquire charges due to polarization when contacting charged solution or being affected by nearby environmental charges. However, the net charge density of the solution inside the large diameter MWCNT is low. In addition, the conducting outer layers of MWCNTs can

effectively screen the environmental charges. The proportionality at KCl concentration 0.1 mM-1 M suggests that the transport mechanism under electric field is electrophoresis. This is very different from the transport mechanism in individual SWCNTs with inner diameter below 2 nm [26,27]. A unique power law relationship with exponent smaller than 1 is always observed in these single SWCNT fluidic devices. The origin of such behavior is attributed to the strong electro-osmotic flow inside smaller diameter SWCNTs. In summary, the electro-osmotic flow is much weaker in these MWCNTs of 7 nm average diameter compared with small diameter SWCNTs. Due to the low surface charge; ion enrichment and ion depletion are not expected in my system [28,29]. Electrophoresis will be the dominant transport mechanism. This conclusion is also consistent with previous experiments and theoretical calculations [22,30]. It is worth noting that increased electro-osmotic flow has been observed by grafting small charged molecules at the inner surface of MWCNTs [31]. However, such modification will also increase the roughness of the CNT inner surface and a decrease in slip length is expected.
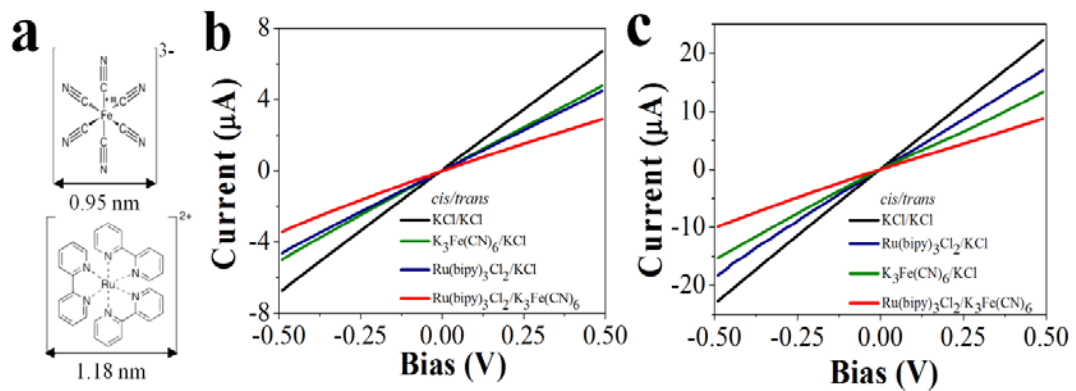
Figure 8.5: (a) Schemes of the molecular structure of the $Fe(CN)_6^{3-}$ anion and $Ru(bipy)_3^{2+}$ cation and their hydrated diameters. (b) The measured I-V curves when the *cis* and *trans* reservoirs were filled with KCl/KCl (black curve), $K_3Fe(CN)_6$/KCl (green curve), $Ru(bipy)_3Cl_2$/KCl (blue curve), and $Ru(bipy)_3Cl_2$/ $K_3Fe(CN)_6$ (red curve), respectively. The concentration of KCl solution was 75 mM and the concentration of $Fe(CN)_6^{3-}$ anion and $Ru(bipy)_3^{2+}$ cation were 12.5 and 25 mM, respectively. (c) The measured I-V curves for the same ionic pathway without the presence of MWCNT membrane.

I then studied the transport of small molecules through these membranes. The Fe(CN)$_6^{3-}$anions (hydrated diameter ~0:95 nm) [10] and Ru(bipy)$_3^{2+}$cations (hydrated diameter ~1:18 nm) [10] were used in this study. The molecular structures of both ions are shown in Figure 8.5a. I first measured *I–V* curves and the results are shown in Figure 8.6b. The solutions in the *cis/trans* reservoirs are KCl/KCl , K$_3$Fe(CN)$_6$/KCl , Ru(bipy)$_3$Cl$_2$/KCl and Ru(bipy)$_3$Cl$_2$/ K$_3$Fe(CN)$_6$. The concentration of KCl solution was always 75 mM, and that of K$_3$Fe(CN)$_6$ and Ru(bipy)$_3$Cl$_2$ solutions were always 12.5 and 25 mM, respectively, which kept the solution ionic strength at both reservoirs the same ($I_C = {}^1\!/_2 \sum C_i Z_i^2$). As shown in Figure 8.5b, at the same bias (i.e. 0.25 V), the ionic current magnitude is in the following sequence: [KCl/KCl] > [K$_3$Fe(CN)$_6$/KCl] > [Ru(bipy)$_3$Cl$_2$/KCl] > [Ru(bipy)$_3$Cl$_2$/ K$_3$Fe(CN)$_6$]. The same sequence was observed for all the MWCNT membranes we measured. In order to verify the CNT effect, we also performed I-V measurements without the presence of MWCNT membrane in the ionic pathway. The measured ionic current magnitude at the same bias (i.e. 0.25 V) is in the following sequence: [KCl/KCl] > [Ru(bipy)$_3$Cl$_2$/KCl] > [K$_3$Fe(CN)$_6$/KCl] > [Ru(bipy)$_3$Cl$_2$/ K$_3$Fe(CN)$_6$] as shown in Figure 8.5c.

Here the ionic current is contributed by the transport of all the ion species in the solution. In order to study the transport of individual ion, I also directly measured the concentration of translocated ions at the *trans* reservoir after applying a bias between two reservoirs for 90 min. In this experiment, the *cis* reservoir was filled with 25 mM K$_3$Fe(CN)$_6$ or Ru(bipy)$_3$Cl$_2$ in 100 mM KCl (pH 7) solution. The *trans* reservoir was filled with 100 mM KCl solution. The concentration of Fe(CN)$_6^{3-}$ ions was determined by

the by the absorption peak in UV-vis measurements or by the pronounced redox peak at 0.18 V versus Ag/AgCl in square wave voltammetry. The concentration of $Ru(bipy)_3^{2+}$ ions was determined by the two adsorption peaks at 285 and 450 nm in UV–vis spectra. As shown in Figure 8.6a, the anion $Fe(CN)_6^{3-}$ can only be driven across the membrane by positive bias and the cation $Ru(bipy)_3^{2+}$ can only be driven across the membrane by negative bias. In addition, the concentration of transported ion increased with the applied bias. At zero bias, the concentration of transported ions was not detectable, confirming that diffusive transport was inefficient for these membranes. These results are consistent with the electric field induced electrophoretic transport. Of the two ions, the anion $Fe(CN)_6^{3-}$ is apparently much easier to transport through the MWCNTs and the concentration is about 25 times higher at the *trans* reservoir when the bias magnitude of 1.5 V is applied for 90 min between the two reservoirs. This observation is consistent with the I-V curves in Figure 8.5b. What is the reason for the large difference in transport between anion $Fe(CN)_6^{3-}$ and the cation $Ru(bipy)_3^{2+}$?
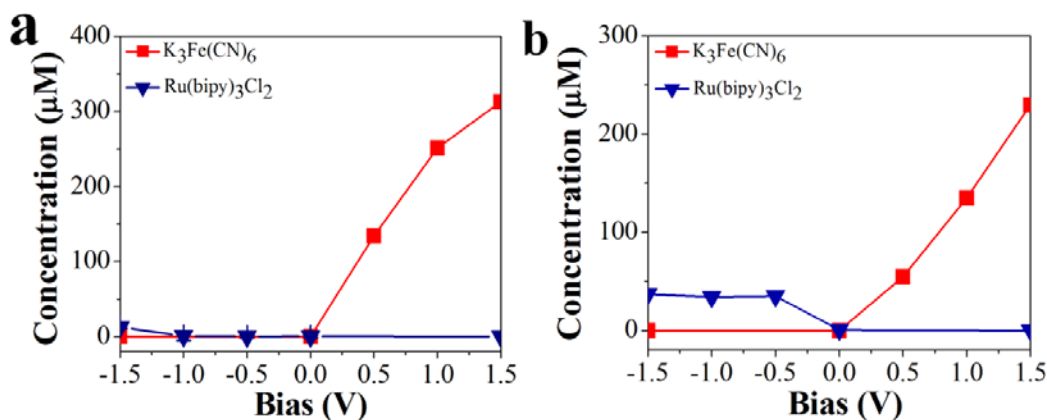
Figure 8.6: (a) The concentration of $Fe(CN)_6^{3-}$ anion (red square) and $Ru(bipy)_3^{2+}$ cation (blue triangle) at the *trans* reservoir as a function of the applied bias. The time was always 90 min. The solid lines are guides for the eye. (b) The concentration of anion $Fe(CN)_6^{3-}$ (red square) and cation $Ru(bipy)_3^{2+}$ (blue triangle) at the *trans* reservoir as a function of the applied bias, when MWCNTs membrane was replaced by AAO. The time was always 90 minutes. The solid lines are guides for the eye.

Interestingly, much higher rejection of cation $Ru(bipy)_3^{2+}$ than anion $Fe(CN)_6^{3-}$ is opposite to the observation in small diameter DWCNTs [10], in which the anion is rejected by the negatively charged carboxyl groups at the CNT ends. Because of the much larger diameter of MWCNTs in these membranes, the charges carried by the ions and at the CNT ends are likely fully screened by the electric double layer (EDL) at 100 mM KCl concentration. Therefore, the electrostatic interactions between ions and CNT ends are not important. In addition, the hydrated diameter of the $Fe(CN)_6^{3-}$ anion is only slightly smaller than that of the $Ru(bipy)_3^{2+}$ cation. So size induced steric hindrance will not contribute significantly to such obvious ion selectivity. One reason may be the different bulk electrophoretic mobility between $Fe(CN)_6^{3-}$ (~10.4 × 10^{-8} m^2 $s^{-1}V^{-1}$) and $Ru(bipy)_3^{2+}$ (~4.0 × 10^{-8} m^2 $s^{-1}V^{-1}$). However, the mobility of $Fe(CN)_6^{3-}$ is only about 2.5 times higher than the mobility of $Ru(bipy)_3^{2+}$, which cannot account for the 25-fold concentration difference at the *trans* reservoir. The main reason may be the stronger molecular interaction between the cation $Ru(bipy)_3^{2+}$ and the curved CNT inner surface. The origin of the interaction may be van der Waals forces and pi–pi stacking between the rings of the $Ru(bipy)_3^{2+}$ cation and the CNT inner surface.

For control experiments, I also used AAO nanoporous membranes with pores of nominal diameter 20 and thickness of 60μm. The ionic conductance through these AAO membranes as a function of KCl concentration is shown in Figure 8.3b. Figure 8.6b represents the transport of two small molecules $K_3Fe(CN)_6$ and $Ru(bipy)_3Cl_2$ through AAO membrane. Between the two ions, the anion $Fe(CN)_6^{3-}$ was easier to be transported through the MWCNTs and the concentration was about 6 times higher at the *trans* reservoir when the bias magnitude of 1.5V was applied for 90 minutes between the two

reservoirs. This permittivity difference may due to the surface interaction. This control experiment supports the view that the ion selectivity in the CNT membrane is mainly due to surface interactions.

8.4: Conclusions

In contrast to small diameter DWCNTs and SWCNTs, the electro-osmosis in the large diameter MWCNTs is weak. Therefore, an electric field can only provide a weak force to drive ions and small molecules. The transport is also significantly affected by the interactions with the hydrophobic CNT inner surface, leading to enhanced selectivity for small molecules.

8.5: References

1. P. Krishnakumar, P.B. Tiwari, S. Staples, T. Luo, Y. Darici, J. He, S.M. Lindsay, Nanotechnology 2012, 23, 455101.

2. G. Hummer, J.C. Rasaiah, J.P. Noworyta, Nature 2001, 414, 188.

3. D. Mattia, Y. Gogotsi, Microfluid Nanofluidics 2008, 5, 289.

4. R.B. Schoch, J. Han, P. Renaud, Rev. Mod. Phys. 2008, 80, 839.

5. A. Noy, H.G. Park, F. Fornasiero, J.K. Holt, C.P. Grigoropoulos, O. Bakajin, Nano Today 2007, 2, 22.

6. M. Whitby, N. Quirke, Nat. Nanotechnol. 2007, 2, 87.

7. C.Y. Lee, W. Choi, J.-H. Han, M.S. Strano, Science 2010, 329, 1320.

8. B.J. Hinds, N. Chopra, T. Rantell, R. Andrews, V. Gavalas, L.G. Bachas, Science 2004, 303, 62.

9. J.K. Holt, H.G. Park, Y.M. Wang, M. Stadermann, A.B. Artyukhin, C.P. Grigoropoulos, A. Noy, O. Bakajin, Science 2006, 312, 1034.

10. F. Fornasiero, H.G. Park, J.K. Holt, M. Stadermann, C.P. Grigoropoulos, A. Noy, O. Bakajin, Proc. Nat. Acad. Sci. 2008, 105, 17250.

11. B. Corry, J. Phys. Chem. B 2007, 112, 1427.

12. J. Wu, K.S. Paudel, C. Strasinger, D. Hammell, A.L. Stinchcomb, B.J. Hinds, Proc. Nat. Acad. Sci. 2010, 107, 11698.

13. M.A. Derylo, K.C. Morton, L.A. Baker, Langmuir 2011, 27, 13925.

14. M. Scott, Y. Juhwan, C. Alan, T. Yu-Chong, Nanotechnology 2006, 17, S23.

15. D. Cai, L. Ren, H. Zhao, C. Xu, L. Zhang, Y. Yu, H. Wang, Y. Lan, M.F. Roberts, J.H. Chuang, M.J. Naughton, Z. Ren, T.C. Chiles, Nat. Nanotechnol. 2010, 5, 597.

16. Z. Wang, Y. Ou, T.-M. Lu, N. Koratkar, J. Phys. Chem. B 2007, 111, 4296.

17. X. Sun, X. Su, J. Wu, B.J. Hinds, Langmuir 2011, 27, 3150.

18. V. Srinivasan, W.I. Higuchi, Int. J. Pharm. 1990, 60, 133.

19. M. Mulder, Basic principles of membrane technology, Kluwer Academic Publishers, Dordrecht, the Netherlands, 1994.

20. R.B. Schoch, J. Han, P. Renaud, Rev. Mod. Phys. 2008, 80, 839.

21. M.H. Oddy, J.G. Santiago, J. Colloid Interface Sci. 2004, 269, 192.

22. M. Majumder, N. Chopra, B.J. Hinds, ACS Nano 2011, 5, 3867.

23. G. Zhong, J.H. Warner, M. Fouquet, A.W. Robertson, B. Chen, J. Robertson, ACS Nano 2012, 6, 2893.

24. C. Gao, S. Ding, Q. Tan, L.-Q. Gu, Anal. Chem. 2008, 81, 80.

25. D. Stein, M. Kruithof, C. Dekker, Phys Rev. Lett. 2004, 93, 035901.

26. P. Pang, J. He, J.H. Park, P.S. Krstić, S. Lindsay, ACS Nano 2011, 5, 7277.

27. H. Liu, J. He, J. Tang, H. Liu, P. Pang, D. Cao, P. Krstic, S. Joseph, S. Lindsay, C. Nuckolls, Science 2010, 327, 64.

28. K. Zhou, M.L. Kovarik, S.C. Jacobson, J. Am. Chem. Soc. 2008, 130, 8614.

29. Q. Pu, J. Yun, H. Temkin, S. Liu, Nano lett. 2004, 4, 1099.

30. J.A. Thomas, A.J.H. McGaughey, Nano lett. 2008, 8, 2788.

31. J. Wu, K. Gerstandt, M. Majumder, X. Zhan, B.J. Hinds, Nanoscale 2011, 3, 3321.

CHAPTER 9: SUMMARY AND FUTURE RESEARCH

9.1: Summary of results

In summary, this dissertation presents the optimization of a customized SPR instrument for quantitative study of protein-protein and protein-DNA molecular interactions. Using the customized SPR, a K_d value of ~13 μM was obtained for Cyt c-hNgb molecular interactions. This K_d value is in a general agreement with a published result. Based on the SPR results, it was reasonable to confirm that there is no substantial influence of CD-loop flexibility, due to the disulfide bond in between Cys 46 and Cys 55 amino acid residues, on the affinity of hNgb with Cyt c. The use of the customized SPR system was extended to investigate protein-DNA interactions. K_d values of ~8 nM and ~15 nM in the presence and absence of Mg^{2+} for EctopoI-pBAD/Thio interaction were determined, respectively. A larger dissociation rate constant (k_d) was obtained for interaction between Mg^{2+} bound EctopoI and pBAD/Thio supercoiled plasmid DNA. These SPR results suggested that the enzyme turnover would be enhanced in the presence of Mg^{2+}.

To date, there is no clear procedure to analyze biphasic SPR data. A theoretical approach based on the analytical solution of linear biphasic rate equations has been introduced. Based on this approach one can confidently chose the correct underlying biphasic interaction mechanism and determine the kinetic parameters with high confidence levels.

This dissertation introduces a new label free analytical method to quantitatively study the protein-protein interaction, based on a charge sensing mechanism. Using chemically modified quartz nanopipettes, the derived K_d value (~20 μM) for the Cyt c-

hNgb complex formations matched very well with SPR measurements. Finite element based numerical simulations also reproduced the nanopipette experimental results. All together, these results suggest that nanopipettes have a potential to quantitatively study protein-protein interactions in attoliter sensing volumes.

In addition, the translocation of charged molecules through CNT nanopores under the effect of an electric field has also been investigated. The observed molecule-based selective nature of hydrophobic and nanometer sized CNT pore walls are helpful to understand the selective nature of intracellular transport.

9.2: Future research

This dissertation also aimed to develop new SPR sensors by incorporating CNTs on the gold surface. This research was started with a hope to achieve better sensitivity of the SPR sensor. In order to prepare CNT film on the gold surface, one milligram of commercially available Hipco purified CNTs was put in 1% V/V aqueous solution of Triton X-100 and sonicated for 1 hour. The mixture was centrifuged at a speed of 18800X and at 4°C for 40 minutes. The appropriate amount of the centrifuged mixture (usually 2.5-4 ml) was vacuum filtrated so that the CNTs could make a layer on the filter paper (Nitrocellulose membrane filter, Millipore Corporation) with pore size 0.1 μm. Then the membrane filter (still inside the filtration system) was washed with a copious amount of DI water. The gold coated glass chip was cleaned in piranha solution (conc. H2SO4: H2O2::3:1) for 5 minutes and dried with Argon gas. The Nitrocellulose membrane filter with CNTs was faced upside down so that CNTs would have contact with the gold surface. The chip and membrane filter assembly was sandwiched in between general laboratory filter paper (Fisherbrand) and was pressed overnight with a

flat load of 44 lbs., with even surface, overnight. On the following day the load was removed and the membrane filter was peeled off from the gold surface. The gold chip with CNT layer was annealed in an argon environment at 270°C for 20 hours. I used the furnace in Dr. Wenzhi Li's lab at FIU for annealing. The Veeco MultiMode AFM microscope operated in tapping mode in air was used to confirm the presence of CNT thin film on gold. The oscillation amplitude, scan rate, and scan size were varied for different scans in order to obtain the best results. Aluminum coated silicon (N-type) AFM tips (ACTA-SS-10, NanoScience instruments, k ~ 25-75 N/m) was used in all AFM scanning. All the experiments were conducted at room temperature. AFM experiments were further processed by the Gwyddion Image Analysis Software.
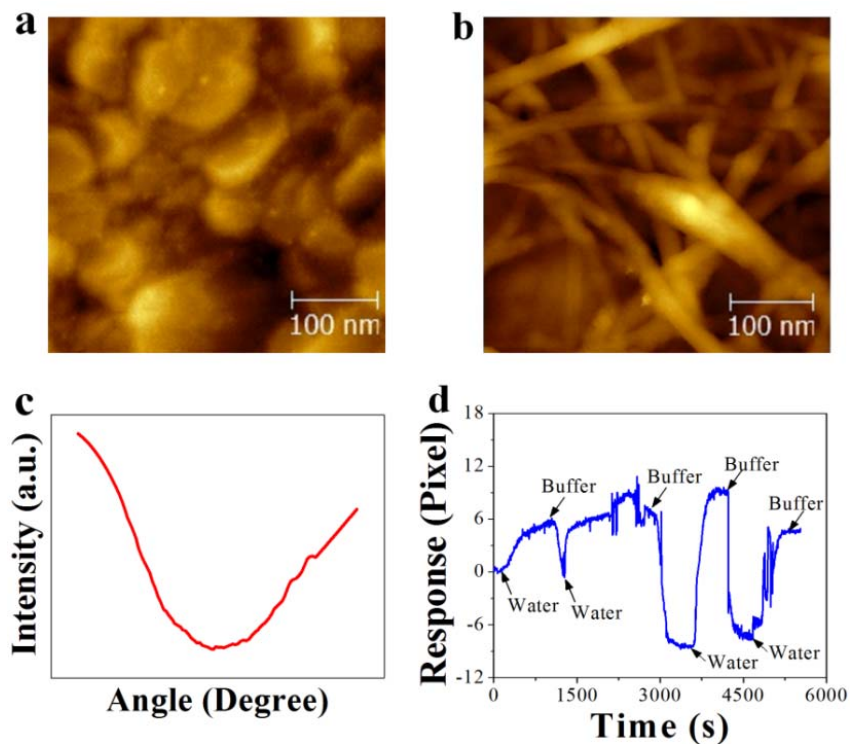

Figure 9.1: AFM images of (a) hydrogen flamed and (b) CNT transferred gold coated glass chip. (c) SPR curve with the CNT membrane transferred gold ship. (d) SPR sensorgram for the sensor chip as mentioned in Figure 9.1b.

Figure 9.1a shows the AFM image of the hydrogen flamed cleaned gold chip and Figure 9.1b shows the gold chips with CNTs. As shown in Figure 9.1c, the SPR dip, for CNT transferred chip, was found to be much broader as compared to cleaned gold without CNTs (Figure 5.1b). This might be due to much thicker CNTs on the gold surface, and it was very difficult to maintain the uniform thickness of CNT layer in the modified chip. On top of this the SPR response was found to be very unstable. The layer of CNTs transferred onto the gold chip using the protocol described here might not reside well on the gold chip. Therefore, it will be interesting to see the SPR results with atomic thick graphene layer (layers) grafted on the gold chip with special procedures.

The extension of theoretical simulations for analysis biphasic SPR data to the non-linear rate equations and the data analysis procedures coded in a computer program would make a complete toolset in order to understand and analyze the biphasic SPR data. This will help experimentalists to identify the correct biphasic SPR interactions and to extract the rate constants with high confidence level.

Based on my expertise on nanofabrication, I have started fabricating a nanohole SPR instrument. As shown in Figures 9.2a and 9.2b (optical microscopy images), the free standing SiN film (325 nm) was fabricated using the nanofabrication techniques, including photolithography and the dry/wet chemical etching procedures. The inset of Figure 9.2a depicts the optical image for purposefully broken SiN membrane for comparison. After SiN membrane fabrication ~150 nm of gold layer was deposited over SiN membrane, using an e-beam evaporator.

The Veeco Multimode AFM microscope operated in tapping mode in air was used to characterize the thickness of the as-deposited gold layer. Figure 9.2c represents the

AFM step-height profile for the determination of the gold film thickness. Figure 9.2d is the SEM image of the gold layer deposited on the SiN window (inside dotted white square) as shown in Figure 9.2a. In future, arrays of manholes can be drilled on the gold coated SiN window (Figure 9.2d). This chip can be used to fabricate the nanohole SPR instrument for the detection of biomolecular interactions. The sensitivity of such an instrument is better and considerably low sample volume is enough for experiments as compared to traditional SPR instruments.
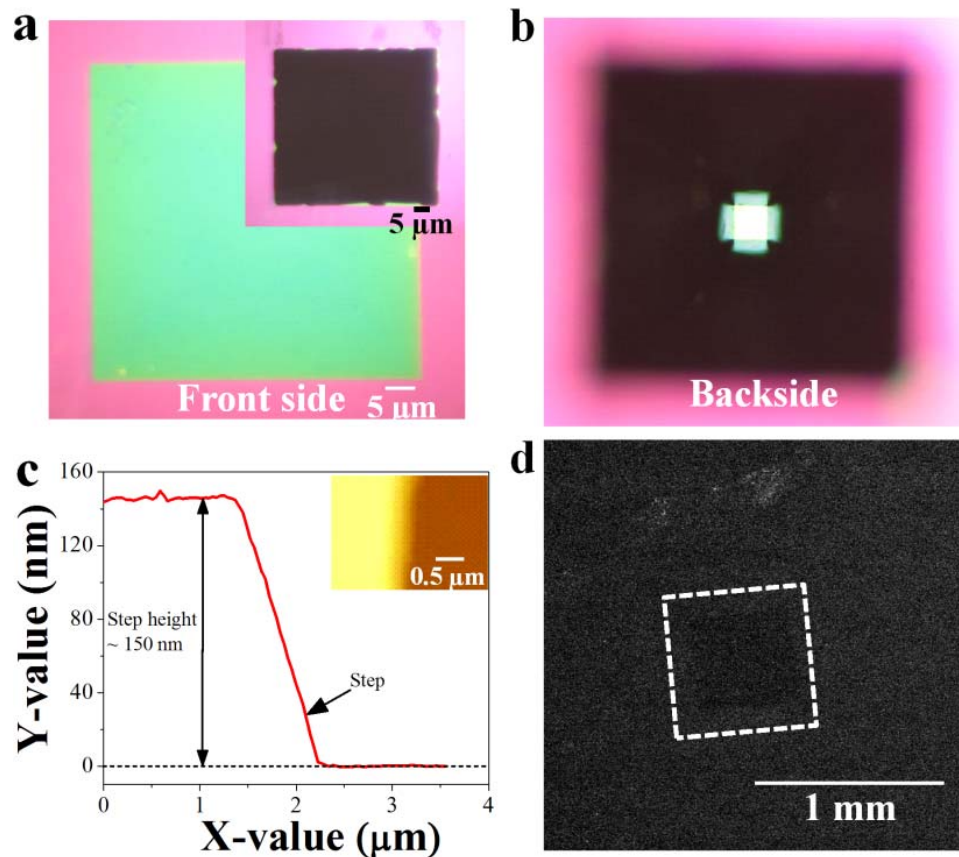
Figure 9.2: (a) Optical image of as-fabricated 325 nm free standing SiN membrane from the membrane side (front side). Inset: Optical image for broken SiN membrane. (b) Optical image of SiN membrane from the opposite of the membrane side (back side). (c) Step height profile for the AFM image of the ~150 nm gold layer over SiN membrane. Inset: AFM image showing the edge of gold layer over SiN surface. The edge was patterned using photolithography. (d) SEM image of ~150 nm gold layer deposited SiN membrane window (inside dotted white square).

Several improvements can still be made to enhance of yield of nanopipette experiments. With better surface modification strategies to improve surface charge uniformity, to increase receptor density, and to prevent nonspecific binding, I expect that the yield and sensitivity of the functionalized nanopipette will be greatly improved. The sensitivity of the nanopipette will be further improved if the analyte can be effectively delivered to and enriched in the nanopipette tip.
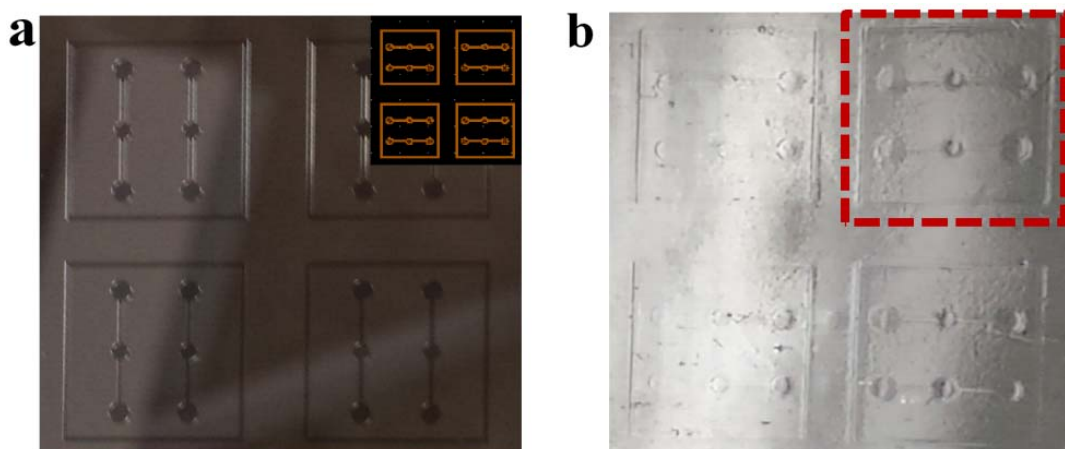

Figure 9.3: Image for the portion of (a) as-fabricated PDMS mold. Inset: portion of mask design using the Layouteditor mask drawing software. (b) pattered PDMS layer with micro-channels (inside red dotted square).

I have started fabrication of PDMS microfluidic channels using nanofabrication techniques. A 325 nm silicon oxide (SiO_2) coated (one side) 500 μm thick silicon (Si) wafer (3 inches in diameter) was used to spin coat the SU-8 3025 photoresist. A two-step programmed spin coating was followed to spin coat the photoresist: Speed 1= 500 rpm, Ramp 1= 100 rpm/s, Time 1= 10 s (Program 1), and Speed 2= 1400 rpm, Ramp 2= 300 rpm/s, Time 2= 30 s (Program 2). The wafer was treated with HDMS primer prior to spin coating. The expected thickness of the photoresist was to be 50 μm. The wafer was then baked at 95°C for 12 minutes. After allowing the wafer to cool down, it was loaded in the

mask aligner to be exposed under UV-light. The laser based mask maker (uPG101, Heidelberg Instrument) was used to write patterns on the blank glass mask substrate (5300 Å of AZ1518 photoresist coated over 5×5 inch chromium deposited glass). Mask patterns were designed using the Layout editor or the AutoCAD software.

The wafer was then developed using SU-8 developer for 8 minutes followed by Isopropyl alcohol (IPA) rinsing, drying with nitrogen gas, and finally hard baking at 160°C for 5 minutes. This final mold was used as to imprint the patterns on the PDMS layer for the fabrication of microfluidic channels. This mold was treated with (Tridecafluoro-1, 1, 2, 2-Tetrahydrooctyl) Trichlorosilane in vacuum prior to using to fabricate micro channels. This treatment allowed the PDMS later to be peeled off easily from the mold. Figure 9.3a depicts a cell phone image of the portion of as-fabricated PDMS mold. The inset of Figure 9.3a is the portion of the mask patterns designed using Layouteditor. Figure 9.3b represents a cell phone image for the portion of patterned PDMS layer (patterns are inside red dotted square). In future, it will be interesting to insert the nanopipettes sandwiched in between the two PDMS layers, with micro-channels. Such a fabrication would be useful to investigate the dynamics of virus like particles passing through the nanopores.

VITA

PURUSHOTTAM BABU TIWARI

2009 – 2015   Graduate Assistant (Ph.D. student)
                     Department of Physics, Florida International University
                     Miami, FL 33199, USA.

2007   B. Ed. in Mathematics, Tribhuvan University, Kathmandu, Nepal

2005   M. Sc. in physics, Tribhuvan University, Kathmandu, Nepal

2003   B. Sc. in physics, Tribhuvan University, Kathmandu, Nepal

PUBLICATIONS AND PRESENTATIONS

P B Tiwari *et al. "Analyzing surface plasmon resonance data: choosing a correct biphasic model for interpretation",* Review of Scientific Instruments, 2015, 86 (3), 035001.

P B Tiwari *et al. "Quantitative Study of Protein-Protein Interaction by Quartz Nanopipettes"*, Nanoscale, 2014, 6 (17), 10255-10263

P B Tiwari *et al. "A surface plasmon resonance study of the intermolecular interaction between* Escherichia coli *topoisomerase I (EctopoI) and pBAD/Thio supercoiled plasmid DNA",* Biochemical and Biophysical Research Communications, 445 (2), 445-450, 2014

Y P Shan, P B Tiwari *et al. "Surface modification of graphene nanopores for protein translocation"* Nanotechnology, 2013, 24 (49), 495102

P Krishnakumar, P B Tiwari *et al. "Mass transport through vertically aligned large diameter Multi Walled Carbon Nanotubes (MWCNTs) embedded in parylene"* Nanotechnology, 2012, 23 (45), 455101

P B Tiwari *et al. "Analyzing biphasic surface plasmon resonance data"* presented in American Physical Society meeting, San Antonio, TX (March 2-6, 2015)

P B Tiwari *et al. "Molecular interaction between Escherichia coli topoisomerase I and pBAD/Thio supercoiled plasmid DNA"* presented in Biophysical Society meeting, Baltimore, MD (February 7-11, 2015)

P B Tiwari *et al. "Electrochemical impedance spectroscopy for graphene surface modification and protein translocation through the chemically modified graphene*

nanopore" presented in American Physical Society March meeting, Denver, CO (March 3-7, 2014)

P B Tiwari *et al.* "*Quartz nanopipettes for the study of protein-protein interaction*" presented in Biophysical Society meeting, San Francisco, CA (February 15-19, 2014)

P B Tiwari *et al.* "*Conical nanopore: A platform for sensing protein-protein molecular interaction*" presented in Nanoflorida conference, Gainesville, FL (September 29-30, 2013)

P B Tiwari *et al.* "*Electric field controlled small molecule transport through vertically aligned large diameter multiwalled carbon nanotube forest membrane*" presented in American Physical Society March meeting, Baltimore, MD (March 18-22, 2013)

P B Tiwari "*Study of Ca^{2+} and Mg^{2+} binding to DREAM protein using SPR*" presented in Joint annual meeting of NHBP and NHSP, Austin, TX (September 21-24, 2011)